



# MASTERARBEIT / MASTER'S THESIS

Titel der Masterarbeit / Title of the Master's Thesis

„Direct radiometric dating of a Neoproterozoic iron formation – Rhenium-Os and highly siderophile element systematics of the Urucum Iron Formation, Brazil“

verfasst von / submitted by

Tobias Prost BSc

angestrebter akademischer Grad / in partial fulfilment of the requirements for the degree of  
Master of Science (MSc)

Wien, 2023 / Vienna 2023

Studienkennzahl lt. Studienblatt /  
degree programme code as it appears on  
the student record sheet:

UA 066 815

Studienrichtung lt. Studienblatt /  
degree programme as it appears on  
the student record sheet:

Masterstudium Erdwissenschaften

Betreut von / Supervisor:

Univ.-Prof. Dr. Christian Köberl

Mitbetreut von / Co-Supervisor:

Dipl.-Min. Dr. Toni Schulz



## Table of contents

I. Acknowledgements .....	III
II. List of Figures and Tables .....	IV
1 Introduction.....	1
1.1 Objective of this thesis .....	1
1.2 State of the Art .....	1
1.2.1 Iron Formations .....	1
1.2.1.1 Mineralogy and Petrology .....	6
1.2.1.2 Ages and distribution of iron formations .....	10
1.2.1.3 Neoproterozoic Iron Formations .....	16
1.2.1.4 Iron formations as proxies for ancient seawater composition .....	19
1.3 Highly siderophile elements and the Re-Os Isotopic system .....	28
1.3.1 Highly siderophile elements .....	28
1.3.1.1 Highly siderophile elements in seawater .....	29
1.3.2 The Re-Os isotopic system.....	30
1.3.2.1 The marine osmium isotope record .....	32
2 Geological setting of the Urucum Iron Formation .....	37
2.1 The South American Platform .....	37
2.2 The Santa Cruz Deposit .....	41
2.2.1 Geological Overview.....	41
2.2.2 Age and Stratigraphy .....	42
2.2.3 Deposition and Tectonics .....	46
2.3 Previous research on the Urucum iron formation .....	48
2.3.1 Geochemistry of the Urucum iron formation .....	50
2.3.2 Isotope Geochemistry of the Urucum iron formation .....	51
3 Samples and Methods .....	52
3.1 Samples .....	52
3.2 Methods .....	53
4 Results .....	56
4.1 Highly siderophile elements .....	56
4.2 Re-Os Isotopes.....	60
5 Discussion .....	62
5.1 Impact of alteration on the Re-Os distribution in the Urucum samples.....	63
5.2 Meteoritic component in the Urucum iron formation.....	68
5.3 The significance of the Re-Os isotope stratigraphy in the Urucum iron formation .....	70
6 Conclusions.....	75

7	References.....	76
8	Appendix.....	8-1
	Abstract .....	8-11

## I. Acknowledgements

I would like to thank both my supervisors, Dr. Christian Köberl and Dr. Toni Schulz, for their tireless and continuous support and help during the development of this thesis. They were both always helpful and willing to give me advice and support. Without the enthusiasm and analytical knowledge of Dr. Schulz, this thesis would have lost in quality.

I would also like to thank Dr. Sebastian Viehmann, who not only provided the vital sample material for this thesis, but also eagerly shared his knowledge and insights with me during data interpretation. He, like my supervisors, was always trying to get the best out of me and this thesis. Without him, this work would not have been possible.

I would also like to extend my thanks to the scientist of the ICP-MS facilities at the Steinmann Institute, University of Bonn, who carried out the measurements of the Ir, Pt, Pd, and Ru concentrations.

Furthermore, I would like to thank Bernardo T. Freitas for sharing his expertise and knowledge of the Urucum area with me.

Lastly, I would like to express my thanks to my parents, whose continuous support made it possible for me to receive an education in the first place. I would like to thank my girlfriend for her belief and support during the writing process. She kept my motivations high, and I could count on her support whenever I needed it. Finally, I'd like to thank all my friends, colleagues, and acquaintances who, consciously or unconsciously, helped me during the creation of this thesis, be it with suggestions, emotional support, entertainment, or just lending an ear.

## II. List of Figures and Tables

<b>Figure 1.1:</b> Representative images of typical iron formations. (A-C) from Konhauser et al. (2017). (D) Photo courtesy of Sebastian Viehmann. (E) from Bekker et al. (2014).....	2
<b>Figure 1.2:</b> Simplified models for deposition of Archean and Paleoproterozoic IF with focus on iron oxidation mechanisms. Iron oxidation via oxygenic photosynthesis (A), metabolic oxidation (B), and abiogenic iron oxidation via UV photooxidation (C). From Bekker et al. (2014). ....	5
<b>Figure 1.3:</b> Mineralogy of iron formations represented by the Dales Gorge Member, Brockman Iron Formation (Australia). From Bekker et al. (2014).....	7
<b>Figure 1.4:</b> Depositional types of Iron Formations. From Gaucher et al. (2016). ....	9
<b>Figure 1.5:</b> Major sediment-hosted iron formations globally (A), and their amount of iron in billion metric tons plotted against time (B). Adapted and modified from Bekker et al. (2014). ....	12
<b>Figure 1.6:</b> Summary of carbon (black) and sulphur (red and grey) isotope data (a) and the evolution of atmosphere throughout Earth’s history (b). From Lyons et al. (2014). ....	13
<b>Figure 1.7:</b> Example of a Neoproterozoic Iron Formation of the Rapitan IF at Cranswick River, Mackenzie Mountains, Northwestern Territories, Canada. From Bekker et al. (2014). Photographs are courtesy of E. Turner. ....	17
<b>Figure 1.8:</b> Shale-normalized REY pattern of selected Archean (the 2.7 Ga Temagami and Manjeri IF), Paleoproterozoic (the ~ 2.4 Ga Brockman and the 1.88 Ga Gunflint IF) and Neoproterozoic (the ~ 590 Ma Urucum IF) iron formations, and modern-day seawater. REY patterns of the Temagami, Manjeri, Gunflint, and Brockman IF were taken from Planavsky et al (2010). REY pattern of the Urucum IF was taken from Viehmann et al. (2016). REY pattern of modern seawater from Douville et al. (2002). ....	22
<b>Figure 1.9:</b> Baseline distribution of HSE (with the exception of Re and Au) in different core, mantle, and crust reservoirs of the Earth, Moon, and Mars(a), and range of Ir concentrations in terrestrial and extraterrestrial materials (b). (a) from Day et al. (2013), (b) from Koeberl (2014).....	28
<b>Figure 1.10:</b> An example Re-Os isochron plot with four shale samples. From Stein and Hannah (2014). ....	31
<b>Figure 1.11:</b> Re and Os concentrations and Re/Os ratios of sources and sinks of Re and Os in seawater. From Stein and Hannah (2014).....	33
<b>Figure 1.12:</b> (A) “Best” published $^{187}\text{Os}/^{188}\text{Os}$ data for paleoseawater of the past 80 million years. The Sr isotopic evolution curve for the same time frame is displayed in pale blue. Adapted and modified from Peucker-Ehrenbrink and Ravizza (2020). (B) Marine $^{187}\text{Os}/^{188}\text{Os}$ record for the Cretaceous, Jurassic, and Late Triassic. From Peucker-Ehrenbrink and Ravizza (2012) .....	34
<b>Figure 1.13:</b> Initial $^{187}\text{Os}/^{188}\text{Os}$ data and Re-Os isochron ages of published ORM (see Peucker-Ehrenbrink and Ravizza 2020, for data sources). Additionally, initial $^{187}\text{Os}/^{188}\text{Os}$ data of (1) the ~2.7 Ga old Temagami BIF (Schulz et al. 2021), and (2) the 2.2 to 1.8 Ga old Biwabik BIF (Ripley et al. 2008) were added to the graph as red dots. Adapted and modified from Peucker-Ehrenbrink and Ravizza (2020). ....	36
<b>Figure 2.1:</b> Geotectonic provinces of South America and the major provinces of the Amazonian Craton. Modified after Engler (2011) and Cordani et al. (2000). ....	38
<b>Figure 2.2:</b> (a) Geological map of the Brasiliano Paraguay fold belt and the Chiquitos-Tucuvaca aulacogen. Adapted and modified from Angerer et al. (2016) and references therein. (b) Detailed geological map of the Urucum district with locations of the drillcores. Adapted and modified from Viehmann et al. (2016). ....	42
<b>Figure 2.3:</b> Stratigraphic scheme of the Jacadigo and Corumbá groups after the lithostratigraphy of de Almeida (1945). The displayed age at the base of the Jacadigo group is after Piacentini et al (2013). From Viehmann et al. (2016). ....	44

<b>Figure 3.1:</b> (a) Locations of the Urucum sample drill cores. Picture courtesy of Sebastian Viehmann. (b) Simplified column of the sample drill cores with marked samples used in this thesis. Modified after Viehmann et al. (2016) and Huang et al. (2021).....	53
<b>Figure 3.2:</b> Graph depicting sample preparation and all steps of analytical methods applied in this study. Note that this is only an outline and many steps (e.g., the repeated evaporation during steps) are not depicted.....	55
<b>Figure 4.1:</b> Stratigraphic distribution of measured HSEs of the Urucum samples of drill core FDUR0051 (a) and FDRK0062 (b). Isochronic samples (discussed below) are plotted as triangles. ....	58
<b>Figure 4.2:</b> Interelement correlations between Re and Os (a), Ru and Re (b), Ru and Pd(c), and Pt and Ir (d), the Re/Os (e), and the Os/Ir ratio (f) of the Urucum samples. Isochronic samples (discussed below) are displayed as circles.....	59
<b>Figure 4.3:</b> Stratigraphic distribution of Re-Os isotopic ratios of the Urucum samples of drill core FDUR0051 (a) and FDRK0062 (b). Isochronic samples (discussed below) are displayed as inverted triangles.....	62
<b>Figure 5.1:</b> Diagrams of the FeO <sub>t</sub> and MnO content against the <sup>187</sup> Os/ <sup>188</sup> Os ratios (A and B, respectively) for the analyzed Urucum IF-Mn-F samples. FeO <sub>t</sub> and MnO data was provided by Viehmann et al. 2016 (see Appendix 8-3 and 8-4). ....	64
<b>Figure 5.2:</b> Al <sub>2</sub> O <sub>3</sub> concentrations of the Urucum samples against measured Re concentration (a) and Os concentration (b). Al <sub>2</sub> O <sub>3</sub> concentrations are taken from Viehmann et al. (2016) (see Appendix 8-3 and 8-4). ....	65
<b>Figure 5.3:</b> Diagrams of the Sr concentrations of the analyzed Urucum samples against measured Re concentration (a), Os concentration (b), and the <sup>187</sup> Os/ <sup>188</sup> Os ratio (c). Sr concentrations are taken from Viehmann et al. 2016 (see Appendix 8-3 and 8-4). ....	67
<b>Figure 5.4:</b> Comparison of Cl-normalized highly siderophile interelement ratios for measured samples, nonmarine, and marine Samples. Ratios of the UCC by Peucker-Ehrenbrink and Jahn (2001), the ratios modern seawater were derived from the studies reported in chapter (1.3.1.1.). Ratios of modern anoxic sediments by Ravizza (1991), of komatiites by Puchtel et al. (2014), and of the Temagami BIF by Schulz et al (2021). ....	69
<b>Figure 5.5:</b> <sup>187</sup> Os/ <sup>188</sup> Os versus <sup>187</sup> Re/ <sup>188</sup> Os diagram of all analyzed samples from both Urucum drillcores (A), of the samples with a calculated, non-negative <sup>187</sup> Os/ <sup>188</sup> Os initial ratio (B), and of the samples reflecting the deep oceanwater component (C). The regression line defined by the samples yield both an age and an initial <sup>187</sup> Os/ <sup>188</sup> Os ratio. The MSWD (Mean Square Weighted Deviation) defines the goodness of a fit. Isochrons were calculated with the program isoplot.....	71
<b>Figure 5.6:</b> Initial <sup>187</sup> Os/ <sup>188</sup> Os data and Re-Os isochron ages as seen in chapter (1.3.2.1), with the best-fit isochron age of the Urucum BIF added in blue. Note that the unradiogenic initial <sup>187</sup> Os/ <sup>188</sup> Os ratio of the Urucum BIF falls into the proposed interval of radiogenic <sup>187</sup> Os/ <sup>188</sup> Os ratios at the end of the Neoproterozoic.....	74
<b>Table 1:</b> Highly siderophile elements data for iron-rich (IF), manganese-rich (Mn-F), and chert samples of Urucum. Sample ID follow the notation of Viehmann et al. (2016). ....	57
<b>Table 2:</b> Highly siderophile elements data for iron-rich (IF), manganese-rich (Mn-F), and chert samples of Urucum. Sample ID follow the notation of Viehmann et al. (2016). ....	61
<b>Appendix 8-1:</b> Recipes for the 1 <sup>st</sup> and 2 <sup>nd</sup> stage anion exchange column separation. From Chu et al. (2014). ....	8-1
<b>Appendix 8-2:</b> Estimates of HSE abundance in various HSE reservoirs and BIFs.....	8-2

<b>Appendix 8-3:</b> Major and trace element concentrations of pure and impure IF samples used in this study. The characterisation of samples into pure and impure is based on REY-analysis of Viehmann et al. (2016). From Viehmann et al. (2016). .....	8-3
<b>Appendix 8-4:</b> Major and trace element concentrations of Mn1-horizon, Mn2-horizon, and chert samples used in this study. From Viehmann et al. (2016). .....	8-4
<b>Appendix 8-5:</b> Hand samples of Urucum samples UR51_10, UR51_14, UR51_15, UR51_16, and UR51_20. Selected samples are marked as red. ....	8-5
<b>Appendix 8-6:</b> Hand samples of Urucum samples UR51_26, UR51_30, and UR51_35. Selected samples are marked as red. ....	8-6
<b>Appendix 8-7:</b> Hand samples of Urucum samples UR51_40, UR51_45, UR51_47, and UR51_51. Selected samples are marked as red.....	8-7
<b>Appendix 8-8:</b> Hand samples of Urucum samples UR51_53, UR51_55, UR51_56, and UR51_51. Selected samples are marked as red.....	8-8
<b>Appendix 8-9:</b> Hand samples of Urucum samples UR62_11, UR62_15, UR62_17, and UR62_25. Selected samples are marked as red.....	8-9
<b>Appendix 8-10:</b> Hand samples of Urucum samples UR62_30, and UR62_31. Selected samples are marked as red.....	8-10

# 1 Introduction

## 1.1 Objective of this thesis

Neoproterozoic iron formations mark a sudden reappearance of banded iron formations after a one-billion-year hiatus in the marine sedimentary record (e.g., Bekker et al. 2014). Their formation might be linked to a regional return of anoxic basins and wide-spread Neoproterozoic glaciations (e.g., Cox et al. 2013; Gaucher et al. 2015). As iron formations are thought to retain their primal (deposition) geochemistry (e.g., Mänd et al. 2022), they are ideal geochemical archives and have long been used to unravel the history and evolution of Earth's hydro- and atmosphere. The Re-Os isotopic system is a popular tool for directly dating the deposition of Proterozoic, early Paleozoic and Mesozoic sedimentary rocks (e.g., Cohen et al. 2017; Peucker-Ehrenbrink and Ravizza 2020). As Re and Os show different compatibility during mantle melting, their interelemental Re/Os ratio can be highly diverse and can cover up to three magnitudes between mantle-derived rocks and crustal rocks. Aside from chronometry, Os isotopes can, therefore, be used to investigate changes in silicate weathering, as well as the chemical evolution of seawater (e.g., Peucker-Ehrenbrink and Ravizza 2020). However, the usage of the Re-Os isotopic system on iron formations has been explored only recently (e.g., Schulz et al. 2021).

The approach of this master thesis encompasses the first application of the highly siderophile element and  $^{187}\text{Re}/^{187}\text{Os}$  isotope tools to the Neoproterozoic Urucum iron and manganese formation (Brazil). Using these geochemical tools, this study seeks to (i) identify primary seawater HSE and Re-Os isotope signatures of the Urucum basin, (ii) to discriminate between possible source contributions to the water column from which the Urucum BIF precipitated (i.e., continental, hydrothermal, cosmic) and to (iii) obtain the first direct Re-Os isochron age of a Neoproterozoic iron formation. Such data provide the background to significantly contribute to our ever-increasing knowledge about the causes of Neoproterozoic climate changes.

## 1.2 State of the Art

### 1.2.1 Iron Formations

Iron formations (IFs) are marine chemical sedimentary rocks that directly precipitated from seawater throughout the Precambrian, particular in the Archean, Paleoproterozoic, and Neoproterozoic eras (e.g., Mänd et al. 2022, and references therein). They are rich in iron (15-

40 wt% Fe) and silica (40-60 wt% SiO<sub>2</sub>) and hold considerable scientific and economic interest and have been extensively studied for more than a century.

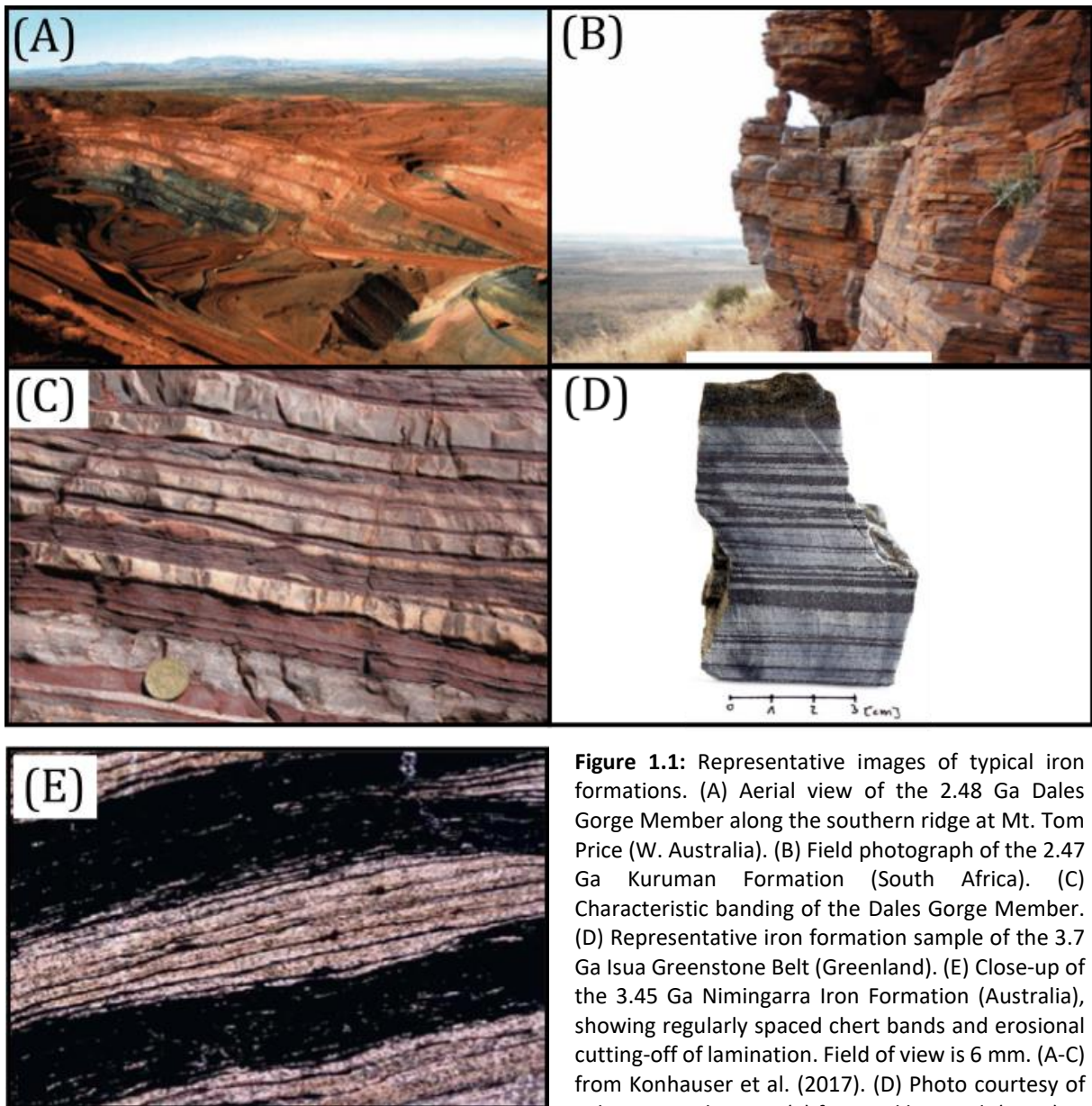


**Figure 1.1:** Representative images of typical iron formations. (A) Aerial view of the 2.48 Ga Dales Gorge Member along the southern ridge at Mt. Tom Price (W. Australia). (B) Field photograph of the 2.47 Ga Kuruman Formation (South Africa). (C) Characteristic banding of the Dales Gorge Member. (D) Representative iron formation sample of the 3.7 Ga Isua Greenstone Belt (Greenland). (E) Close-up of the 3.45 Ga Nimingarra Iron Formation (Australia), showing regularly spaced chert bands and erosional cutting-off of lamination. Field of view is 6 mm. (A-C) from Konhauser et al. (2017). (D) Photo courtesy of Sebastian Viehmann. (E) from Bekker et al. (2014).

Most IFs are texturally composed of distinctive, repetitive layers of fine-grained iron-rich bands and microcrystalline quartz (chert), giving them the term “Banded Iron Formations” (BIFs) (Fig. 1.1A-E). These layers vary in thickness (meter-scale to millimeter-scale) and can laterally be quite extensive (e.g., Konhauser et al. 2017). On the other hand, some IFs lack banding and are instead characterized by granules composed of chert, iron oxide, iron carbonates, and/or iron silicates cemented in early diagenetic chert, carbonate, or hematite, giving them the name “Granular Iron Formations” (GIFs). These GIFs are interpreted to have been deposited in shallow water, proximal setting (near coast, e.g., Konhauser et al. 2017), derived from sedimentary rework of earlier IF (e.g., Beukes and Gutzmer 2008).

Determining the source of iron has long been seen as a sort of “holy grail” in these fields. Early studies suggested a continental source, where  $\text{Fe}^{2+}$  became mobile during weathering in the absence of atmospheric  $\text{O}_2$  (e.g., James 1954; Lepp and Goldich 1964). However, several rivers the size of the modern Amazon, all transporting vast amounts of iron (orders of magnitude higher than known today), would be required to achieve the necessary concentrations of Fe for IFs to precipitate (Trendall and Blockley 1970). Therefore the focus shifted to other possible sources. The discovery of modern hydrothermal vent systems on the seafloor (black and white smokers) in the 1990s led to the emphasis of hydrothermal processes as possible source of iron for the genesis of IFs (e.g., Isley 1995). With the discovery of microfossils in Paleoproterozoic IFs (e.g., Barghoorn and Tyler 1965; Cloud 1965), the importance of microorganisms for the deposition of IFs also received greater attention (e.g., Konauser et al. 2011a).

Accumulation of the large masses of iron present in IFs requires the transportation of iron in the form of  $\text{Fe}^{2+}$ , as  $\text{Fe}^{3+}$  is insoluble when even tiny amounts of dissolved oxygen are present at neutral pH. The presence of iron formations, therefore, suggests an anoxic state of the Precambrian atmosphere and hydrosphere (e.g., Cloud 1973; Bekker et al. 2010), although later studies found the Precambrian systems to be more nuanced and complex with respect to the oxygenation of Earth’s atmosphere and oceans (e.g., Farquhar et al. 2014, and references therein). Several authors proposed the presence of regional “oxygen oases”, places where the local  $\text{O}_2$  production rate exceeded the rate  $\text{O}_2$  loss in an otherwise anoxic ocean (e.g., Olson et al. 2013, and references therein). While the Earth eventually transitioned to a state where its atmosphere was oxygenated, the initial oxygenation of Earth’s atmosphere is still a matter of debate. The general consent, however, is that the oxygenation of the shallow oceans precedes that of the atmosphere by several million years (e.g., Lyons et al. 2014; Konhauser et al. 2017, and references therein). Maintaining low levels of oxygen in the atmosphere while  $\text{O}_2$  production in the oceans steadily rise would require, among other factors, large oxygen sinks, such as IFs, acting as buffers to the increasing  $\text{O}_2$  concentrations until they could no longer be counterbalanced.

However, as IFs were also deposited during times when the atmosphere was sufficiently oxygenated, their relationship with atmospheric oxygen levels may be more complex (e.g., Farquhar et al. 2014). As the deposition of IFs requires the conversion of  $\text{Fe}^{2+}$  into solid-phase oxyhydroxides via oxidation into  $\text{Fe}^{3+}$ , the mentioned oxygen oases were ideal environments for deposition in an otherwise oxygen-free Earth. Over decades of research, several oxidative mechanisms having been proposed.

The historical model is the  $\text{Fe}^{2+}$  oxidation via oxygenic photosynthesis of cyanobacteria (Fig. 1.2A), utilizing oxygenic photosynthesis (e.g., Han and Runnegar, 1992; Knoll et al. 2006; Javaux 2011). These microbes likely flourished in the photic, near-coastal zone and used free

oxygen of shallow oxygenated water and  $\text{Fe}^{2+}$  from reduced upwelling deep-water, which was rich in Fe at the interface between these two layers (redoxcline, e.g., Cloud, 1965, 1973; Bekker et al. 2014). This pathway however would require the existence of oxygenic photosynthesis on early Earth back until 3.7 Gy ago, which is still a matter of debate (e.g., Brocks 2011; Bekker et al. 2014).

The second, most commonly invoked, oxidation mechanism is the metabolic  $\text{Fe}^{2+}$  oxidation via microbial iron oxidizers (Fig. 1.2B). Three major pathways have been established: 1) microaerophilic, 2) anoxygenic photosynthesis and 3) nitrate dependent:

The first pathway, microaerophilic  $\text{Fe}^{2+}$  oxidation, is used by bacteria that were found to be widespread in marine systems, hydrothermal vent systems and in the chemocline (the boundary in a water body that separates the fresh upper water layer from a deeper water layer that is rich in dissolved species) in ferruginous lakes where iron-rich sediments are deposited (e.g., Søgaard et al. 2000; Lehours et al. 2007). The second pathway, anoxygenic photosynthetic, has microorganisms use  $\text{Fe}^{2+}$  as electron donor rather than  $\text{H}_2\text{O}$  during photosynthesis, producing  $\text{Fe}^{3+}$  instead of molecular oxygen (e.g., Widdel et al. 1993; Ehrenreich and Widdel 1994). This mechanism is particularly appealing because it could explain the deposition of IFs without the presence of molecular oxygen and is capable of oxidizing enough  $\text{Fe}^{2+}$  to a water depth of a few hundred meters (e.g., Konhauser et al. 2002, Kappler et al. 2005). The third possible microbially mediated pathway for  $\text{Fe}^{2+}$  oxidation is metabolically coupling of iron oxidation with nitrate reduction (e.g., Straub et al. 1996; Edwards et al. 2003). This pathway appears to be widespread in sediments (Straub and Buchholz-Cleven 1998) and requires an organic substrate (e.g., acetate). However, so far, no laboratory experiments were able to isolate a pure culture of nitrate-reducing iron oxidizers, suggesting that a consortium of organisms may be required for this pathway.

Cairns-Smith (1978) proposed an alternative mechanism of  $\text{Fe}^{2+}$ -oxidation, in which ferrous iron is photooxidated by the high flux of ultraviolet photons prior the rise of atmospheric oxygen and the development of the protective ozone layer (Fig. 1.2C). This reaction has been shown to proceed in acidic water that is exposed to wavelengths in the 200 – 300 nm range (Cairns-Smith 1978) and could account for the deposition of high quantities of (e.g., Pickard 2002, 2003). However, these early abiotic models were tested under relatively simple conditions, with later models suggesting that the contribution of this mechanism is negligible compared to the previous two mechanisms (e.g., Konhauser et al. 2007).

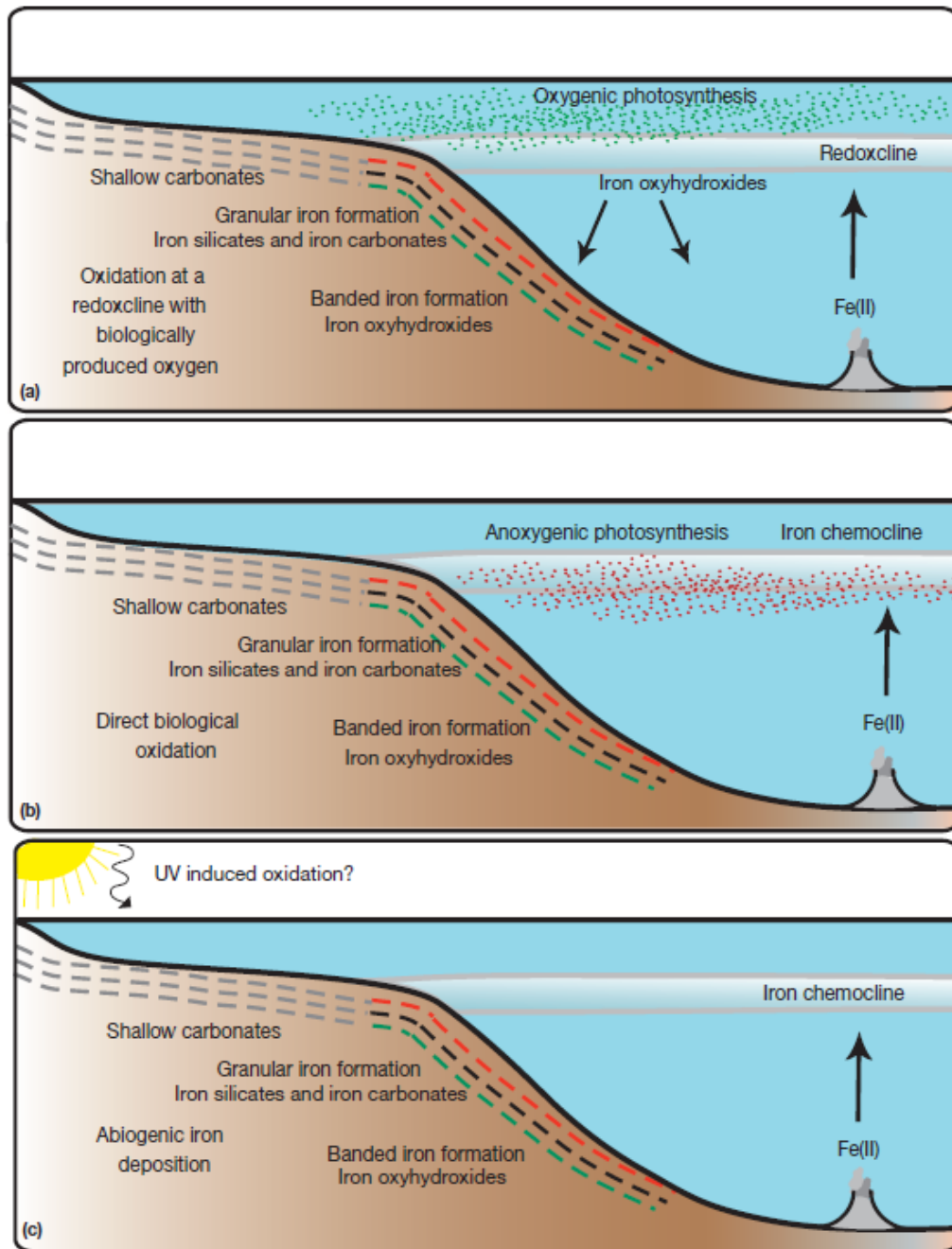


**Figure 1.2:** Simplified models for deposition of Archean and Paleoproterozoic IF with focus on iron oxidation mechanisms. Iron oxidation via oxygenic photosynthesis (A), metabolic oxidation (B), and abiogenic iron oxidation via UV photooxidation (C). From Bekker et al. (2014).

Deposition of large, economically important IFs often coincided with mantle plume breakout events and supercontinent assembly (e.g., Isley and Abbott 1999; Bekker et al. 2004; Barley et al. 2005; Hamilton et al. 2009; Viehmann et al. 2015), which could have led to an enhanced influx of hydrothermal iron and reductants (e.g.,  $H_2S$ ). The higher  $pCO_2$ , sea levels and surface temperature caused by plume events could have resulted in anoxic conditions in local basins or even globally (e.g., Bekker et al. 2014). Tectonic processes and setting as control mechanisms for IF deposition have also received increased attention (e.g., Bekker et al. 2010,

and references therein). Several authors argued that certain tectonic settings, such as isolated basins and graben systems, may have favoured IF deposition (e.g., Ohmoto et al. 2006; Beukes and Gutzmer 2008; Bekker et al. 2014). While Algoma-type IFs were likely deposited in close association with volcanic systems and recycled into the mantle before large landmasses were developed, continental growth created crucial shallow water settings and enhanced Superior-type IFs preservation (e.g., Simonson 2003; see below section for a detailed discussion).

The following chapters will systematically, but only very briefly, discuss the most important characteristics of IFs, which are described in detail in numerous review papers (e.g., Bekker et al. 2014; Konhauser et al. 2017; Mänd et al. 2022). Special attention will be given to their geochemical characteristics and the disparate occurrence and suspected modes of origins of Archean and Paleoproterozoic IFs versus Neoproterozoic IFs.

#### 1.2.1.1 *Mineralogy and Petrology*

The mineralogy of IFs is defined by silica and a variety of Fe-rich and Al-poor minerals, which often occur in characteristic alternating layers of varying scale (BIFs). In the best-preserved sequences (little weathering and low-grade metamorphism), the mineralogy is remarkably uniform, comprising silica, hematite, magnetite, Fe-rich silicate minerals (stilpnomelane, minnesotite, grennalite, and riebeckite), carbonate minerals (siderite, ankerite, calcite, and dolomite), and, to a lesser extent, sulfide (pyrite and pyrrhotite).

*Chert* is ubiquitous in all IFs regardless of type or facies. In BIFs, chert most commonly occurs in layers of wavy to wrinkly laminae (Fig. 1.1E and Fig. 1.2A-D; e.g., Bekker et al. 2014). In granular iron formations (GIFs), it occurs as chert peloids with open packing, indicating precompaction lithification.

The most common Fe-oxide mineral in IFs is *hematite*. Together with magnetite it defines the lamination in most chert layers, occurring in millimeter- to centimeter-thick layers (Fig. 1.2C-D). It is the primary iron-bearing mineral in IFs younger than 2.4 Gy and in IFs of the Lake-Superior type. The timing of hematite growth is ambiguous, but it is thought to form during the very early stage of IF deposition.

*Magnetite* occurs as euhedral, fine- to coarse-grained crystals and is abundant as laminae in cherty Fe-rich layers (Fig. 1.2A). It is commonly found in older IFs (>2.4 Ga) and Algoma-type IFs. It is a secondary mineral and is associated with metamorphism and deformation (e.g., Bekker et al. 2014, and references therein).

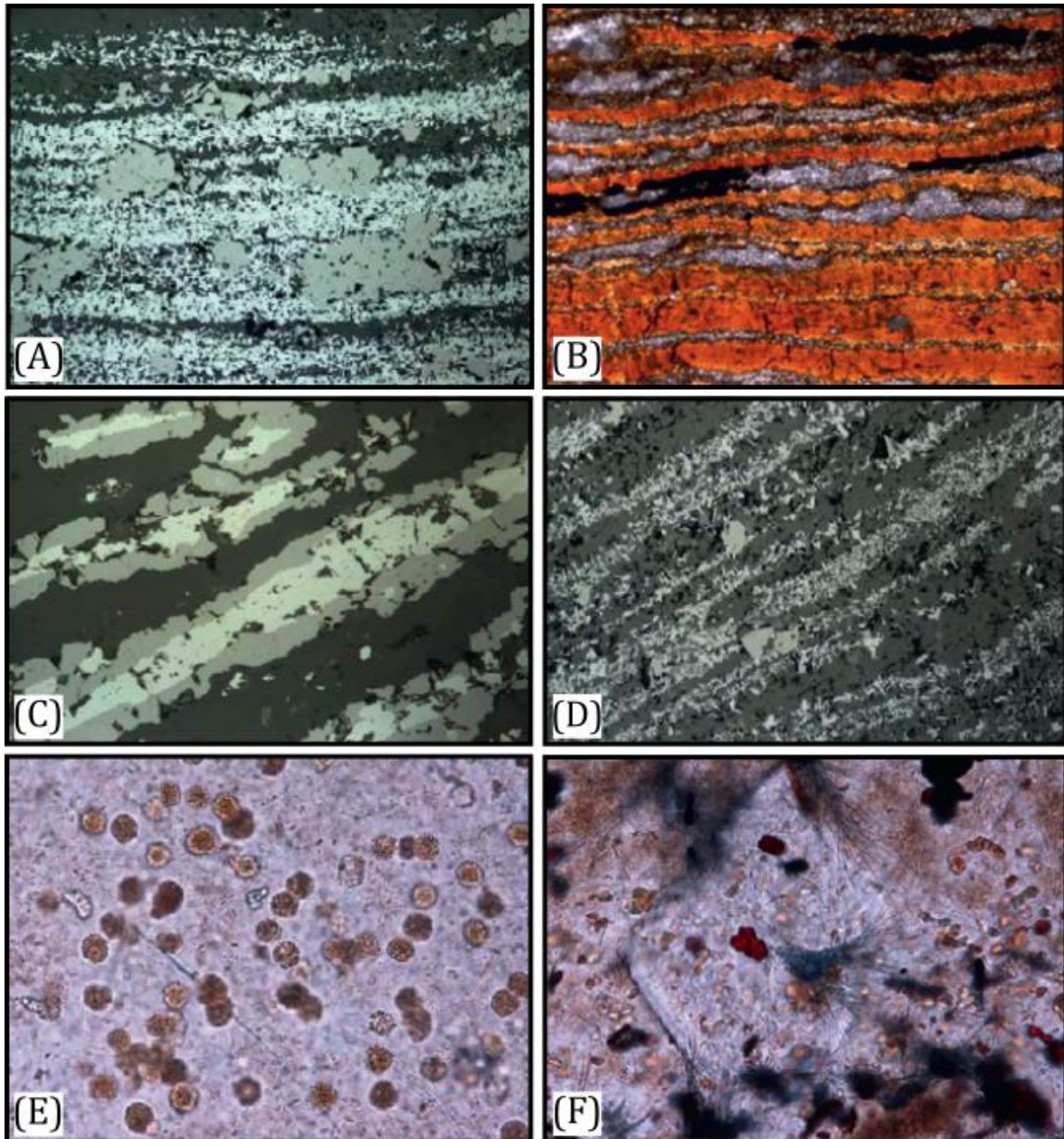


**Figure 1.3:** Mineralogy of iron formations represented by the Dales Gorge Member, Brockman Iron Formation (Australia). (A): Several large clusters of euhedral magnetite in a band of laminated hematite. Field of view: 2.5 mm. (B): Bands of laminated stilpnomelane and fine-grained siderite. Field of view: 0.625 mm (C): Alternating laminae of silica and iron oxides. Cores of hematite are surrounded by magnetite. Field of view: 0.3 mm. (D): Alternating laminae of fine-grained hematite with chert. Field of view: 0.6 mm. (E): Spherical structures of stilpnomelane in a chert matrix. Field of view: 0.6 mm. (F): Coarse-grained euhedral crystals of ankerite enclosing crystals of hematite and riebeckite in a chert matrix. Field of view: 0.625 mm. From Bekker et al. (2014).

The most-common Fe-rich silicate mineral is *stilpnomelane* (Fig.1.2B and 1.2E), indicating lower greenschist facies conditions. Above 400°C it is replaced by biotite. *Minnesotite* is less abundant, and forms during metamorphism and late-stage hydrothermal alteration. *Grennalite* and *riebeckite* are less common but can be important on a regional scale (e.g., Bekker et al. 2014). *Siderite* (Fig. 1.2B) is the most common carbonate and occurs as either tiny single crystals or layers of microcrystalline crystals and can be linked to near-ore alteration. *Ankerite*

*and ferroan dolomite* (Fig. 1.2F) can occur in chert layers and are among the last minerals to form. *Trace minerals* that can be observed in IFs include pyrite, apatite, monazite, xenotime, zircon, ilmenite, and K-feldspar (e.g., Bekker et al. 2014).

None of the minerals described above are primary in origin, as the initial precipitate mineralogy of IFs is not preserved. The observed minerals rather reflect multiple, significant post-depositional alteration events during diagenetic or metamorphic conditions, causing progressive changes in mineralogy, including replacement, recrystallization, change of grain size, and obliteration of the primary texture (e.g., Klein 2005). Traditionally, the initial mineralogy of IFs is interpreted to be comprised of ferric oxyhydroxide phases, e.g. ferrihydrite ( $\text{Fe}(\text{OH})_3$ ). Precipitation occurred directly from seawater via oxidation of dissolved  $\text{Fe}^{2+}$  in the photic zone of paleo oceans or enclosed waterbodies (e.g., Mänd et al. 2022 and references therein) during times where concentrations of ferrous iron in seawater was significantly higher (0.03 to 0.5 mM in the Archean compared to 2.0 nM in modern oceans; e.g., Holland 1973; de Baar and de Jong 2001). More recent work suggests that the concentration of dissolved silica was also elevated in the Archean (2mM compared to < 0.10 mM in modern oceans; e.g., Tréguer et al. 1995; Maliva et al. 2005). It has, therefore, been suggested that the initial precipitates may have been ferric oxyhydroxide-Si-gels (e.g., Percak-Dennett et al. 2011). However, studies have shown that iron-silicates were not quantitatively important (e.g., Rasmussen et al. 2017; Robbins et al. 2019) and that iron-rich and chert bands represent different watermasses (Bau et al. 2022), making homogeneous ferric oxyhydroxide-Si-gels unlikely.

Iron formations have been broadly divided into Algoma type and Lake Superior type deposits (Gross 1980). Lake Superior-type IFs are often interbedded with carbonate, quartz arenite and black shale but seldom with volcanic rock (e.g., Gross 1980). Deposition is considered to have taken place in near-shore on passive-margin and continental shelf settings dominated by sedimental input (Fig. 1.4C, e.g., Konhauser et al. 2017). Sources of Fe are considered to be distant from the deposition site (up to a thousand km), giving insight into the strong influence of  $\text{Fe}^{2+}$  bearing, hydrothermal waters on the Archean and Paleoproterozoic ocean chemistry (e.g., Konhauser et al. 2017; Mänd et al. 2022).

Algoma-type IFs are associated with volcanic rocks and sometimes greywackes. They are generally linked to submarine-emplaced volcanic rocks and often spatially coupled with volcanogenic massive sulfide deposits (VMS) (e.g., Bekker et al. 2010; Konhauser et al. 2017). Deposition likely occurred close to volcanic arcs or spreading centers with significant influence of hydrothermal vent activity (Fig. 1.4B, e.g., Barrett et al. 1988; Gross 1980, 1983). Granular iron formations (GIFs), as well as any sedimentological features besides fine banding, are absent. Algoma-type IFs are, therefore, considered to be deposited in comparably deeper-water settings, far from continental landmasses (e.g., Bekker et al. 2010). They ideally reflect the

influence of local hydrothermal vent fluids on partially closed basins or even open seawater systems (e.g., Gourcerol et al. 2016).

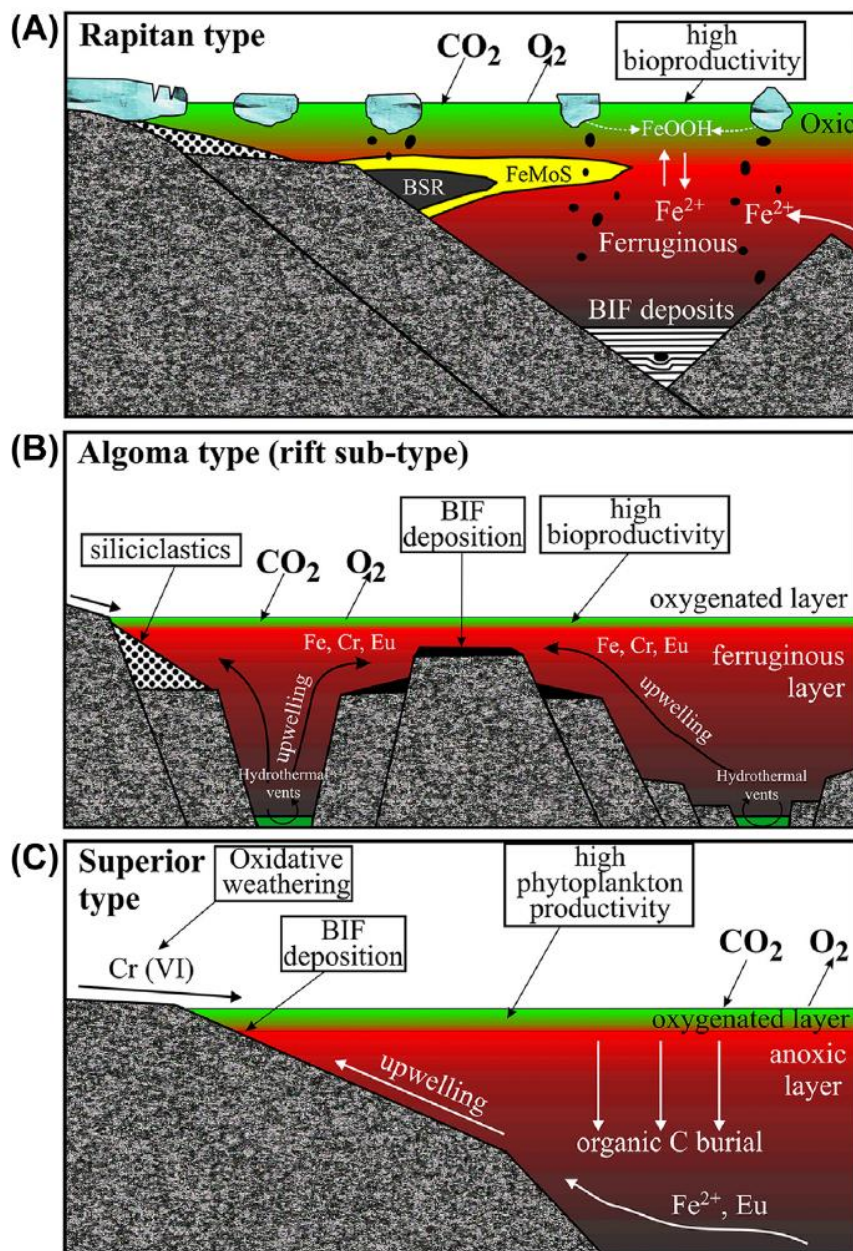


**Figure 1.4:** Depositional types of Iron Formations. (A) Deposition model of Rapitan type BIF by the example of the Rapitan Group. (B) Deposition model of Algoma type BIF of the Jucurutu Fm. (NE Brazil). (C) Deposition model of Lake Superior type BIF of the Yerval Fm. (Uruguay). From Gaucher et al. (2016).

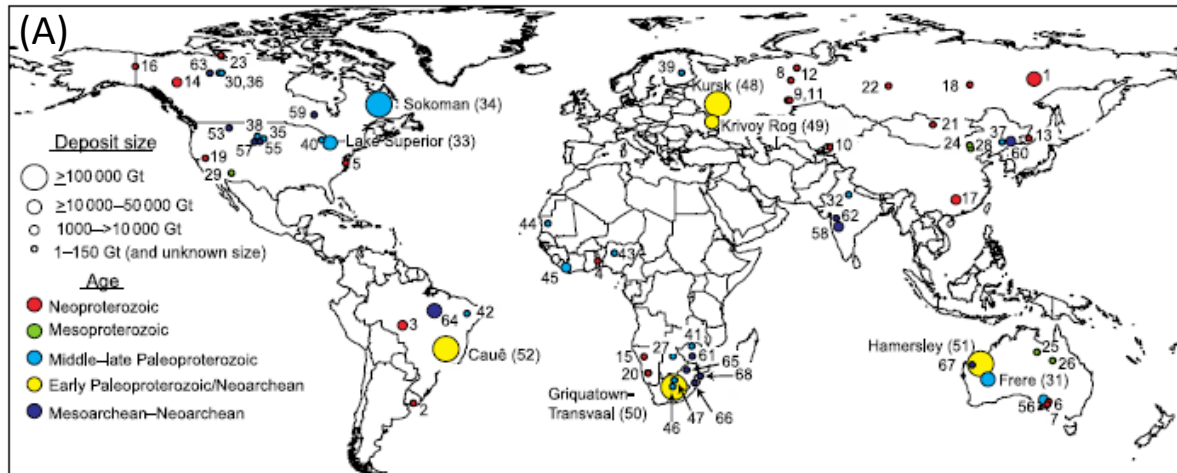
Iron formations older than 3.0 Gy are generally ascribed to the Algoma-subtype, although 2.7 – 2.6 Gy old examples are known (e.g., Konhauser et al. 2017). Their occurrences are generally slimmer and laterally smaller than Lake Superior type IFs, reaching only a maximum thickness of 50 m and lateral extension of 10 km along strike (e.g., Bekker et al. 2014). However, they are more numerous in terms of deposits and general distribution. Original size and distribution of these occurrences is most likely underestimated, as most experienced

advanced deformation and/or tectonic displacement (e.g., Gole and Klein 1981; Bekker et al. 2014). Lake Superior-type IFs are typically thicker and more extensive. The largest deposits initially containing up to  $10^8$  Mt at 15 wt% Fe (James 1983; Isley 1995) and spanning an area of 100,000 km<sup>2</sup> (e.g., Bekker et al 2010).

A clear differentiation between the two IF-types has not always been easy and as studies advanced distinction became increasingly difficult. Hence, both types are nowadays seen as idealized endmembers of geochemical precipitates (Bekker et al. 2014, and references therein). Another type, namely the Rapitan-type (Fig.1.4A), is exclusive to the Neoproterozoic and associated with a glacially influenced deposition environment (for a detailed review see Chapter 2.2).

#### 1.2.1.2 *Ages and distribution of iron formations*

Iron Formations are present on all cratons and shields. They formed within three billion years of geologic history, first appearing in the Eoarchean and finally disappearing in the Ediacaran (from >3.7 Ga to ~ 560 Ma; Fig. 1.5A). As the Earth's system experienced drastic changes throughout its history, deposition of IFs happened under a multitude of environmental settings, indicated by diverse textures and mineral compositions (e.g., Mänd et al. 2022; Bekker and Kovalick 2021).



# Formation/Group/Deposit	Location	Age (Ma)	# Formation/Group/Deposit	Location	Age (Ma)
1. Maly Khingan Formation	Russia	560	38. Estes Formation	USA	2020-2100
2. Yerbel Formation	Uruguay	600	39. Paakkö Iron Formation	Finland	2080
3. Jacadigo Group (Urucum district)	Brazil	600	40. Glen Township Formation	USA	2100
4. Bisokpabe Group	Togo	600	41. Lomagundi Group	Zimbabwe	2100-2200
5. Chestnut Hill Formation	USA	600	42. Caldeirão belt	Brazil	>2078-~2687
6. Holvileña Ironstone	Australia	650	43. Malumfashi, Maru, Birnin Gwari, Kushaka, Muro, Egbo-Isanlu, and Obajana schist belts	Nigeria	2100
7. Braemar Iron Formation	Australia	650	44. Ijil Group	Mauntania	2200
8. Vil'va and Koyva Formations	Russia	650	45. Nimba (Ibiritite)	Liberia	>2100-~2615
9. Bakeevo (Tolparovo) Formation	Russia	650	46. Hotazel Iron Formation	South Africa	2200
10. Dzhetyntau Suite	Kyrgyzstan	650	47. Timeball Hill Formation	South Africa	2320
11. UK Formation	Russia	700	48. Kursk Supergroup	Russia	2450
12. Yamata Formation	Russia	700	49. Krivoy Rog Supergroup	Ukraine	2450
13. Lake Khanka Formation	Russia	700	50. Transvaal Province	South Africa	
14. Rapitan Formation	Canada	715	Griquatown Iron Formation	South Africa	2431
15. Chuos Formation	Namibia	715	Kuruman Iron Formation	South Africa	2465
16. Tindir Group	USA	715	Penge Iron Formation	South Africa	2480
17. Fulu Formation	China	741	51. Hamersley Basin	Australia	
18. Medvezhevo Formation	Russia	700-750	Boolgeeda Iron Formation	Australia	2445
19. Kingston Peak Formation	USA	700-750	Weeli Wollli Formation	Australia	2449
20. Numees Formation	Namibia	700-750	Brockman IF (Joffre Mbr)	Australia	2461
21. Mugur Formation	Mongolia	767	Brockman IF (Dales Gorge Mbr)	Australia	2461-2495
22. Nizhne-Angara Formation	Russia	800	Mt. Sylvia Formation	Australia	2505
23. Aok Formation (Shaler Supergr.)	Canada	840	Marra Mamba Iron Formation	Australia	2597
24. Xiamaling Formation	China	1368	52. Cauê Formation	Brazil	2450
25. Roper Group	Australia	1490	53. Indian Creek Metamorphic Suite	USA	2470-2750
26. South Nicholson Group	Australia	1500	54. Ruker Series	Antarctica	2450-2480
27. Shoshong Formation	Botswana	1600	55. Benchmark Iron Formation	USA	2480-2560
28. Chuanlinggou Iron Formation	China	1650-1600	56. Hutchison Group (Middleback)	Australia	2500
29. Pike's Peak Iron-Formation	USA	1728	57. Nemo Iron Formation	USA	2560-2890
30. Gibraltar Formation	Canada	1880	58. Chitradurga Group	India	2614
31. Frere Formation	Australia	1890	59. Beardmore-Geraldton assemblage	Canada	2700
32. Alwar Group (North Delhi fold belt)	India	1850-2000	60. Anshan Iron Formation	China	2700
33. Lake Superior region	USA + CAN		61. Manjeri Iron Formation	Zimbabwe	2700-2830
Gunfint Iron Formation	Canada	1878-1850	62. Bababudan Group	India	2720
Negaunee Iron Formation	USA	1874-1850	63. Central Slave Cover Group	Canada	2730-2920
Biwabik Iron Formation	USA	1880-1850	64. Carajás Formation	Brazil	2740-2750
Ironwood Iron Formation	USA	1880-1850	65. West Rand Group	South Africa	2960
Riverton Iron Formation	USA	1880-1850	66. Pongola Supergroup	South Africa	2960
34. Sokoman Iron Formation	Canada	1877	67. Jack Hills belt	Australia	>3080
35. Rochford Formation	USA	1884	68. Moodies Group	South Africa	3230
36. Basile Formation	Canada	1930			
37. Liaohé Group	China	1950-2050			

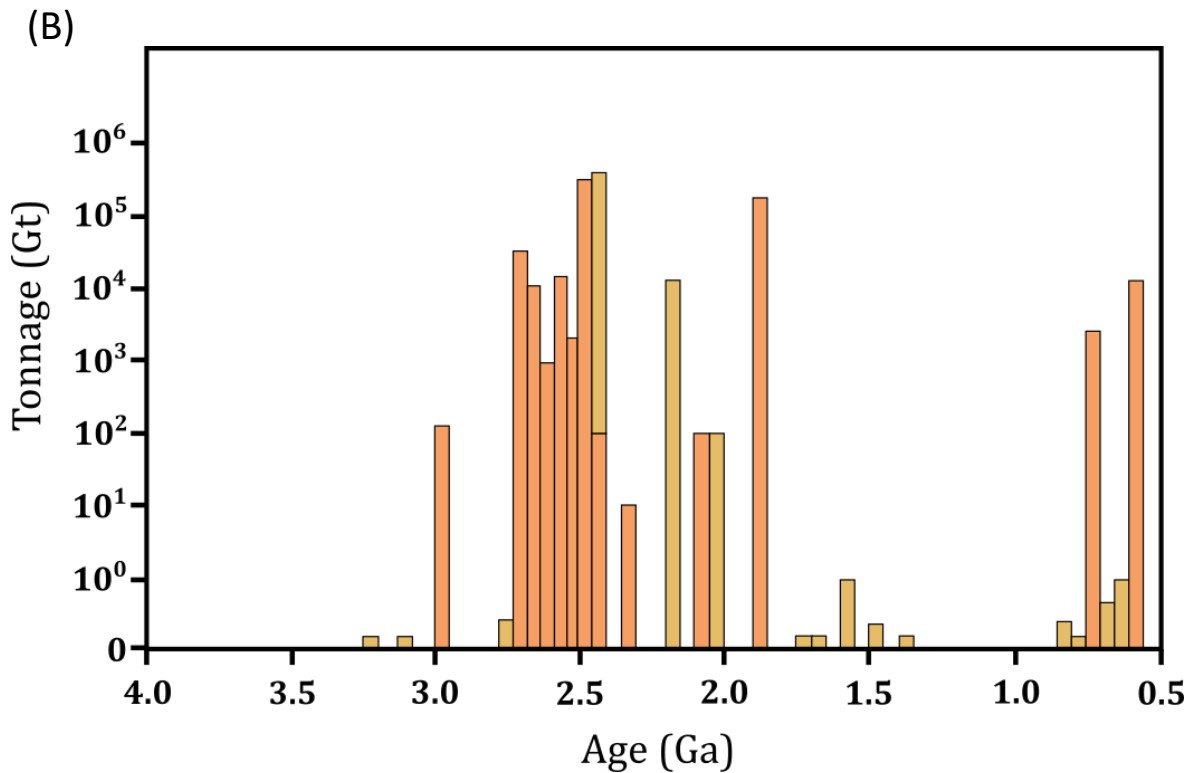


**Figure 1.5:** Major sediment-hosted iron formations globally (A), and their amount of iron in billion metric tons plotted against time (B). Deposits that have a poor age constrain are shown in pale orange. Note that (B) lacks deposits which have no published tonnage data. Adapted and modified from Bekker et al. (2014).

Iron Formations appear in the geological record as early as the Eoarchean (4.0 – 3.6 Ga) and are, together with Pillow basalts, the first geological indicator for the presence of oceans or submarine sediments. The oldest known successions are found in the >3.77 Ga Nuvvuagittuq Supracrustal Belt, Canada (e.g., Mänd et al. 2022; Mloszewska et al. 2012) and the >3.7 Ga Isua Supracrustal Belt, Greenland (e.g., Dymek and Klein 1988; Nutman et al. 2013). Deposits older than 3.0 Gy are scarce and often severely metamorphosed, but well preserved and economically important IF deposits are known (e.g., the ~ 3.5 Gy old Iron Ore Group of the Singhbhum cration, India; e.g., Mukhopadhyay et al. 2008). It remains unclear if the lack of widespread IF deposition during the Paleoarchean is due to unfavorable environmental conditions or simply due to preservational bias (e.g., Bekker et al. 2014). Deposits become more common during the Neoarchean (2.8 – 2.5 Ga). Between 2.60 and 2.45 Gy the most laterally extensive and economically valuable known IFs in Earth’s history were deposited (e.g., in the Hamersley Group, Australia, or in the Transvaal Supergroup, South Africa). These major depositions are associated with mantle plume breakout events (e.g., Heaman 1997) and immediately precede global scale, super-continent assembling, collision events (e.g., Barley et al. 2005). Iron formations deposited after 2.40 Gy significantly differ in texture and scale compared to their Archean counterparts. They are the first to contain intervals of iron silicates and carbonates of granular texture (GIF), and are much smaller in scale, however, large

deposits still occur (e.g., the 2.43 Ga Hotazel Formation, South Africa; e.g., Tsikos et al. 2003). The textural changes in these IFs are interesting, as their deposition immediately precedes the pervasive oxygenation of Earth’s atmosphere.

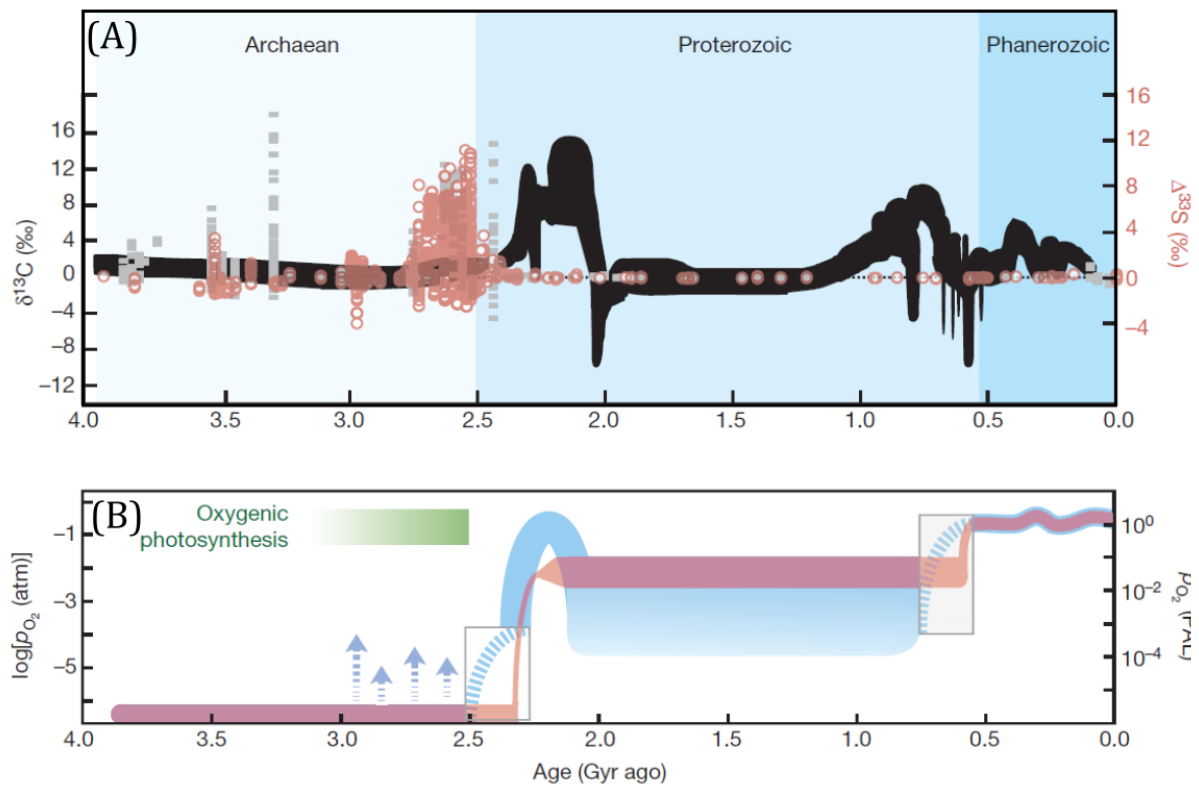


**Figure 1.6:** Summary of carbon (black) and sulphur (red and grey) isotope data (A) and the evolution of atmosphere throughout Earth’s history (B). From Lyons et al. (2014).

In a series of steps between 2.45 to 2.32 Gy, collectively referred to as “Great Oxidation Event” (GOE; e.g., Holland 2002; Bekker et al. 2004), Earth’s atmosphere underwent the gradual increase of free oxygen from basically being non-existent ( $\text{O}_2 < 10^{-5}$  present atmospheric level (PAL)) to permanent oxygen concentrations of  $\text{O}_2 > 10^{-5}$  PAL (Fig. 1.6B), resulting in many and profound changes in Earth’s environmental systems. They include, amongst others, the cessation of mass-independent S isotope (S-MIF) variations in sulfide and sulfate minerals after 2.3 Gy (Fig. 1.6A), which is considered nowadays as the “smoking gun” argument for the rise of atmospheric oxygen. The sulfur isotope record has long been linked to oxygen. Mass-independent fractionation before 2.4 Gy showed highly variable  $\delta^{33}\text{S}$  and  $\delta^{36}\text{S}$  values, while during 2.45 – 2.32 Gy, they became more uniform and very small. The change has been attributed to the increase in oxidative weathering, which was able to produce higher sulfate content in the oceans as well as microbial reduction of sulfate (see Farquhar et al. 2011; 2014, for detailed reviews). In addition, formation of several redox-sensitive minerals in the geological

rock record (like detrital uraninite, pyrite, and siderite) ceased after 2.4 Gy. Their presence has been interpreted to reflect a reducing Archean atmosphere. Furthermore, paleosols younger than 2.4 Gy show iron concentrations that are expected at higher O<sub>2</sub> concentrations. Also, red beds (coarse-grained siliciclastic sediments in arid fluvial and alluvial terrestrial settings, formed under oxidizing conditions) first appear in the geological record after 2.3 Gy. These changes are all indicators for the increase of atmospheric O<sub>2</sub>.

Concurrent with the GOE, Earth also experienced a series of extensive glaciation events. Up to three separate and extensive glaciation events have been determined (e.g., Bekker 2011), which have collectively been called the Huronian glaciation event (HGE; e.g., Kopp et al. 2005). These severe glaciations were likely caused by the loss of greenhouse conditions due to the rising levels of atmospheric oxygen via a series of climatic feedbacks (e.g., Bekker and Kaufman 2007). Greenhouse conditions before the GOE were maintained by a combination of atmospheric methane and carbon dioxide. The rise of atmospheric oxygen caused methane to oxidize, leading to a collapse of the greenhouse conditions, as the carbon dioxide levels alone were too low to maintain them, and resulting in the widespread glaciations.

Even during and after these drastic changes, small scale IFs still were deposited (e.g., Paakola 1971; Laajoki and Saikkonen et al. 1977; Frei et al. 2008). They are the proof that deep marine water was, if only periodically, still ferruginous and that shallow waters were sufficiently oxygenated for Fe<sup>2+</sup> oxygenation to occur (e.g., Wang et al. 2015; 2016). The smaller size of the deposits may have been due to a deeper oxygenation of the oceans, where Fe<sup>2+</sup>-rich anoxic waters were largely oxidized and precipitated in the deep oceans and only periodically ascended to the continental margins (e.g., Farquhar et al. 2014; Konhauser et al. 2017). Alternatively, it has been suggested that the marine sulfate levels may have been high enough for the precipitation of iron sulfides instead of iron oxides (e.g., Kump and Seyfried 2005; Planavsky et al. 2012; Scott et al. 2014).

Larger and more extensive IFs reappear in the geological record at around 1.88 Gy. These IFs contain a large number of hematitic GIFs and were deposited coeval with submarine basaltic volcanism (e.g., Fralick et al. 2002; Schulz and Cannon 2007). They have been related to a mantle plume breakout event during early assembly of the supercontinent Columbia (e.g., Hamilton et al. 2009; Konhauser et al. 2017; see Heaman et al. 2009 for an opposing view). However, it is unclear if these deposits reflect local-scale, restricted basin conditions or the global seawater composition. Contemporaneously with the deposition of the 1.88 Gy GIFs is a peak in deposition of volcanogenic massive sulfides (VMS). Several studies interpret these findings as indicator for anoxic and ferruginous deep-water conditions in open marine settings (e.g., Slack et al. 2007; Slack and Cannon 2009). A set of younger, regionally extensive, IFs were deposited around 1.85 Gy. They mineralogically and texturally differ from their 1.88 Gy counterparts (e.g., James et al. 1968; Cannon et al. 2008; Cannon et al. 2010). They were

likely deposited in deep waters and are linked to submarine mafic volcanism (e.g., Konhauser et al. 2017).

After 1.85 Gy, the occurrence of IF deposits decrease drastically. IFs and iron rich lithologies occurring only sporadic for the next 1.1 Gy (1.85 – 0.72 Ga). These deposits are small in scale and occur in sedimentary rock-dominated successions in a shallow water setting. The cause of the disappearance of IFs deposits has long been debated and is still not fully clear. The current consensus argued for a varying redox state of the ocean from 1.85 – 0.72 Gy, with both euxinic and ferruginous deep waters existing below an oxygenated shallow water zone (e.g., Planavsky et al. 2011; Bekker et al. 2014). This would argue that the deposition of IFs is more dependent on an enhanced input of hydrothermal vents rather than the redox state of the oceans.

Notable IF deposits re-emerge in large quantities in the Neoproterozoic (1.0–0.538 Ga) coinciding with dramatic changes in the hydro- and atmosphere (e.g., Pierrehumbert et al. 2011; Hoffman et al. 2017). During the Neoproterozoic, the Earth underwent a series of major geological events, such as (i), severe glacial, commonly referred to as “Snowball Earth” (e.g., Kirschvink 1992; Hoffman et al. 1998), (ii) the break-up of a supercontinent, Rodinia, and the return to anoxic, ferruginous ocean conditions (e.g., Canfield et al. 2008). Geological evidence of this time period indicates that ice sheets were present at even low latitudes during, at least, two long lived glaciations: The older Sturtian (~715-660 Ma) and the younger Marinoan (~650-635 Ma) glaciation (e.g., Hoffman et al. 2017). While earlier works argued for a hard “Snowball Earth”, where Earth was, save for a few “oases”, entirely covered by a global ice layer (e.g., Kirschvink 1992; Hoffman et al. 1998), more recent studies favour a soft, “Slushball Earth” (e.g., Allen and Etienne 2008; Pierrehumbert et al. 2011; Sansjofre et al. 2011). Under “Slushball Earth” conditions, the Earth was still largely covered by massive ice sheets; however, parts of the planet remained ice free, especially around the equatorial zone.

The majority of Neoproterozoic IF are closely associated with glaciogenic sediments. Deposition supposedly occurred during declaciation, as indicated by the presence of dropstones (isolated rock-fragments within fine-grained sediments or pyroclastic beds) and interlayering with diamictites/tillites (unsorted and unstratified material directly deposited by glacial ice). Some of these IF deposits are intercalated with volcanogenic rocks, which are most likely related to the breakup of the supercontinent Rodinia. Texturally, they differ from their Archean and Paleoproterozoic counterparts (for example, hematite is the major iron-bearing mineral, not magnetite). Their occurrence supports long and sever glaciation events as well as the existence of redox-stratified basins. However, “Snowball Earth” conditions might not be a requirement for their deposition. Other factors, such as tectonics, mantle plume events and changes in sea-levels, may have had a larger impact on the formation of Neoproterozoic IFs (e.g., Bekker et al. 2014; Gaucher et al. 2015). The influence of hydrothermal vents in

particular has been discussed vigorously. While Neoproterozoic IFs lack indicators for high-temperature (>250°C) hydrothermal vent fluids (e.g., Viehmann et al. 2015), several suggested the presence of low-temperature (<250°C) hydrothermal vent fluids (e.g., Alexander et al. 2008; Basta et al. 2011; Huang et al. 2021).

With the onset of the Phanerozoic, IFs disappear from the geological record, with conditions on Earth no longer suited for their deposition. Instead, they are replaced by ironstones as iron-rich sediment deposits, with peak depositions in the Ordovician-Devonian and Jurassic-Paleogene (e.g., Bekker et al. 2014, and references therein). Ironstones are generally composed of iron oxide ooids of goethite or limonite cemented in Fe-carbonates, have little chert and are only several meters in thickness. They are thought to have been deposited during times of low sedimentation rates that indicate the beginning of rising sea-levels (e.g., Burkhalter 1995; Taylor et al. 2002), but, as with IFs, their genesis and the source of iron remain controversial (e.g., Bekker et al 2014, and references therein).

#### 1.2.1.3 *Neoproterozoic Iron Formations*

Neoproterozoic Iron Formations (NIFs) not only provide us an exclusive IF-type (the Rapitan type), but they also mark an apparently sudden reappearance of IFs after one billion years of absence in the sedimentary record (e.g., Bekker et al. 2010). They formed in entirely different settings, with different compositions and textures (e.g., Klein and Beukes 1992) compared to Archean and Paleoproterozoic BIFS. Neoproterozoic IFs have been reported on every continent except Antarctica and were deposited during a time where  $pO_2$  should have been significantly higher than during the Archean and Paleoproterozoic. Their deposition therefore indicate drastic changes in the Earth's system, most likely the return of anoxic and ferruginous conditions in marine basins or sub-basins due to the "Snowball Earth" and the ongoing break-up of the supercontinent Rodinia (e.g., Cox et al. 2013).

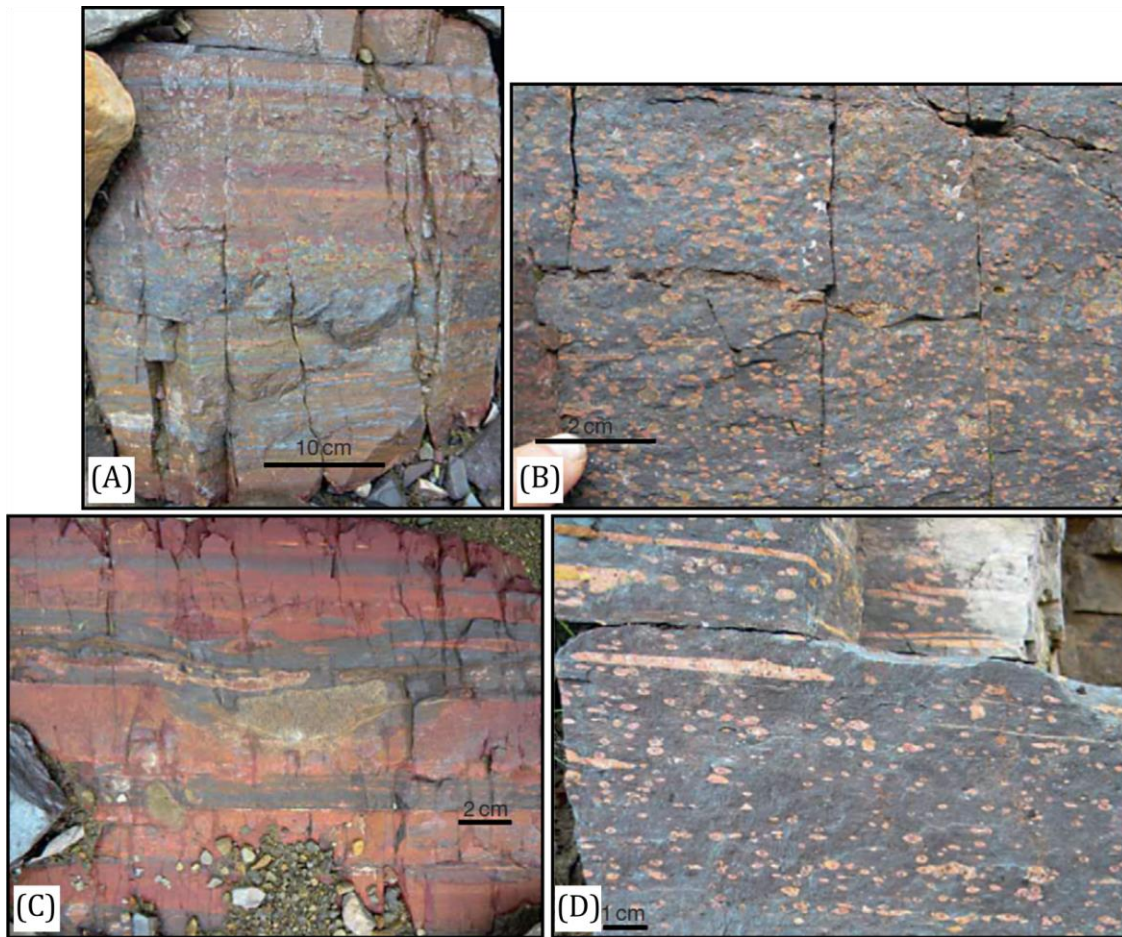


**Figure 1.7:** Example of a Neoproterozoic Iron Formation of the Rapitan IF at Cranswick River, Mackenzie Mountains, Northwestern Territories, Canada. (A) Nodules and bands of jasper interlayered with banded hematite and overprinted by anastomosing hematite. (B) Nodules and lenses of jasper in massive hematite. (C) Bands of jasper and hematite with dropstones, overprinted by anastomosing hematite. (D) Nodules and lenses of jasper in massive hematite. From Bekker et al. (2014). Photographs are courtesy of E. Turner.

Banding in NIFs is generally composed of laminated hematite, jaspilite, massive magnetite, hematitic mudstone, and jasper, with bedding often poorly developed or even entirely absent (Fig. 1.7A-D). Instead, NIFs are more commonly present as ferruginous siltstone or within a matrix of diamictite. Some NIFs host significant amounts of manganese, typically forming discrete Mn-rich beds (e.g., Klein and Ladeira 2004). Many deposits occur in rift basins and in contact with massive to poorly stratified diamictites or compact diamictite horizons. Other Neoproterozoic IF deposits lack diamictites but can host dropstones or be interlayered with tillites (Fig. 1.7C; e.g., Hoffman et al. 2011). These associations point to deposition in a glacially influenced environment. However, this is not true for all NIF occurrences. Several deposits show association with volcanic rocks or carbonate and shale successions (e.g., Gaucher et al. 2015). As the first NIF deposits were found, initially, the age of deposition was determined by dating stratigraphically adjacent and/or correlative formations. These first datings constrained the age of several Neoproterozoic IFs into the proximity of the Sturtian glaciation (e.g., Hoffman et al. 2004; Fanning and Link 2008; MacDonald et al. 2010). It was, therefore, initially thought

that all Neoproterozoic Iron Formations are related and were deposited during the Sturtian glaciation (e.g., Cox et al. 2013; Gaucher et al. 2015). This claim was eventually questioned as more and more IFs of this era were found and dated. Several iron formations show deposition ages that make them much older than the Sturtian glaciation (e.g., Basta et al. 2011; Stern et al. 2013; Xu et al. 2013). Other NIF deposits show deposition ages that make them younger than the Sturtian glaciation, but still relate them to younger Cryogenian or Ediacaran glaciation events (e.g., Blanco et al. 2009; Gaucher and Poiré 2009; Piacentini et al. 2013). However, many ages are poorly constrained as there has been no reliable dating method for direct dating of IFs. Finding a reliable tool in the direct dating of chemical precipitates has been a major goal, as it allows a better assessment of depositional ages of NIFs and globally correlate Neoproterozoic ice ages.

Nonetheless, these findings imply that the deposition of the majority of NIFs is somewhat related to the major glaciation events of the Sturtian (~715-660 Ma) or Marinoan (~650-635 Ma) glaciations of “Snowball Earth”, or the later, rather locally occurring, Ediacaran Gaskiers (~580 Ma) glaciation. An appealing theory for the deposition of these Rapitan-type iron formations is that the global glaciation events of the Cryogenian shifted the environment to conditions more favorable for IF deposition. During glaciation, ice sheets covered large parts of the oceans and basins, limiting the exchange between the hydro- and atmosphere or cutting it off entirely. Under these conditions, the water masses became more reducing, related to biological oxygen consumption, as atmospheric oxygen was no longer supplied, which allowed the metals derived from hydrothermal vent fluids or submarine rock alteration to remain in solution. During glacial retreat the interaction of the oceans and atmosphere reappeared and subsequently oxidizing conditions returned to the water column, leading to the precipitation of ferric oxyhydroxides and associated carbonates. At the same time, the melting glaciers and sea ice introduced clastic material and drop stones into the IF succession (e.g., Angerer et al. 2016). However, it has become clear that glaciation is not as crucial for the return of IFs as initially thought. As mentioned, not all NIFs show indications for a glacial environment. Instead, elevated hydrothermal activity and rifting associated with the breakup of Rodinia and mantle plumes are considered to be more important for the development of NIFs (e.g., Gaucher et al. 2015, and references therein).

One of the most significant NIF deposits occurs in the Jacadigo Group, Brazil. These IFs deposits have been extensively studied in the last decades (see Chapter 2.2) and serve as an important archive about the environmental conditions and evolution of the late Neoproterozoic. This NIF was, therefore, selected for the intended Re-Os study on Neoproterozoic IFs.

To summarize, deposition of Neoproterozoic Iron Formations is not restricted to the middle-Cryogenian Sturtian Glaciation. They occur in the Tonian, Cryogenian and the Ediacaran, spanning a deposition time of over 150 Ma. Several NIFs show no signs of glacial influence,

indicating that the global glaciation events alone were not responsible for the return of IF deposits, and that other parameters, e.g., basin-structure or tectonics, have a significant influence on favourable conditions for deposition.

#### 1.2.1.4 *Iron formations as proxies for ancient seawater composition*

Due to their long record in geological time, IFs have been used to constrain redox conditions and transitions in the atmosphere-ocean system, the composition of paleo-seawater and the evolution of the marine biosphere (see Konhauser et al. 2017 for reviews). Their usefulness, however, is based on a number of assumptions and conditions that have to be met. First, it must be assumed that the primary precursor mineral phases have preserved the elemental and isotopic composition of the waters columns from which the IF precipitated (which is most often a mixture of seawater and hydrothermal waters, see Chapter 1.2.1.4.1). These assumptions have been verified through a series of adsorption and diagenesis experiments (e.g., Døssing et al. 2011; Robbins et al. 2015; for a different view see Halevy et al. 2017). Second, we must assume that the measured geochemical signal is commonly uncontaminated by continentally derived detrital materials, providing a “pure”, authentic signal of the marine chemistry. This must be verified for each IF individually, which is typically done by measuring the concentrations of detrital sourced elements, such as Al, Ti, and Zr. Last, it must be assumed that, due to the low permeability and elemental mobility in IF, the geochemical signals of seawater are able to survive high levels of metamorphism and do not experience widespread alteration by secondary fluids, except later-stage ore formation (e.g., Robbins et al. 2015). As with detrital contamination, this has to be verified for each IF deposit individually. However, several studies on metamorphosed IF deposits highlighted that certain signatures, such as Ni and Zr values, as well as Fe isotope values, remain unaffected by metamorphism and preserve their authigenic signal (e.g., Frost et al. 2007; Robbins et al. 2015). These findings further support the notion that IFs in general preserve the geochemical signal of their depositional environment.

There are, however, a few complications that make interpretation more challenging. One is that the back-calculations of isotope ratios and elemental concentrations of paleoseawater based on IF data are often very simplistic, as many parameters, such as elemental adsorption coefficients, are only known through empirical observations (e.g., Konhauser et al. 2007). Therefore, they often fail to fully take into account the complexity of the system, e.g., competing ions in solution (e.g., Robbins et al. 2016; Mänd et al. 2022). This problem is worsened due to the lack of a modern analogue to IF, as we are unable to study the mechanisms in their natural environment. Although their lithologies are genetically different from those of IFs, ironstones, marine iron-manganese-oxide crusts and hydrothermal exhalative deposits have been studied

and may improve our understanding of IF formation mechanisms (e.g., Goto et al. 2020). A second problem is the inefficient adsorption of some elements, leading to low authigenic concentrations in the IF. Even minimal additions of detrital material or volcanic ash can overprint the primal seawater chemical signals (e.g., Viehmann et al. 2015a; 2015b; 2016; Angerer et al. 2016; Haugaard et al. 2016). It is, therefore, essential to gain a better understanding of the mineral host of the studied chemical component and mixing relationships with detrital material. Third, one must take caution in interpreting the chemical signals of IF, as they may not depict characteristics of open seawater. As mentioned above, the deposition of IF may have taken place in a mixture of seawater and hydrothermally derived plume water (e.g., Planavsky et al. 2010; Smith et al. 2013). It has been argued that the deposition of IF was likely to primarily have occurred not in a homogeneously stratified ocean but in partially enclosed basins, where the water chemistry may have differed from the open ocean (e.g., Bekker et al. 2010, 2014; Mänd et al. 2022). In recent years there have also been suggestions that the iron-bearing minerals in the IF formed through post-depositional oxidation of primary Fe(II)-silicate minerals (e.g. Rasmussen et al. 2017; Muhling and Rasmussen 2020). In these models, IF would track the geochemical signal of basal oxidizing fluids and not of seawater.

#### 1.2.1.4.1 Geochemistry

Iron formations have long been popular in investigating the composition of ancient seawater because it can be assumed that they are very likely to retain the chemical signature of the water from which they precipitated. Secular changes in the composition of IFs have been used as proxies for the evolution of seawater and the availability of nutrients in the marine environment over time (Bekker et al. 2014, and references therein). Examples are briefly discussed below.

### **Phosphorus, Nickel, and Chromium**

Phosphorus, nickel, and chromium are prominent trace elements that can be used as proxy to track seawater composition. The dissolved phosphate concentrations of ancient oceans can be determined with IFs because the amount of solid-phase P in iron oxides scales directly with the dissolved P concentrations (e.g., Feely et al. 1998; Edmonds and German 2004). Furthermore, most P is retained in the iron oxides, even during recrystallization and secondary apatite precipitation (e.g., Poulton and Canfield 2006), and these processes are largely controlled by the surface chemistry of the iron oxides (e.g., Bjerrum and Canfield 2002). Similar, nickel concentrations also follow a distribution coefficient relationship during the precipitation of ferric oxyhydroxides, allowing to track first-order trends in dissolved Ni concentrations in seawater (e.g., Konhauser et al. 2009; Bekker et al. 2014). Nickel is a

bioessential nutrient for marine organisms, playing a key-role in several enzyme systems (e.g., Ragsdale 2009). Its availability is, therefore, of special interest and can have far-reaching consequences. Iron-normalized Ni concentrations in IFs show dramatic changes over time, dropping significantly at 2.7 Gy (from  $>0.0004\text{M}$  to  $0.0002\text{M}$ ) and slowly approaching modern values ( $<0.0001\text{M}$ ; e.g., Konhauser et al. 2009). Finally, enrichment in chromium can be used to track the terrestrial Cr flux to the oceans (e.g., Frei et al. 2009; Konhauser et al. 2011). While IFs that are deposited nearshore are often not suited to derive seawater compositions, they do allow insights into the composition and supply of continental derived waters and, by extension, the weathering processes on the continents and the state of atmospheric oxygenation during the time of their deposition. It has been suggested that, while Cr isotope fractionation did happen, Cr was largely immobile on land until 2.5 Ga, after which Cr enrichment increases in shallow-water IFs, peaking at 2.32 Gy, synchronous with the loss of mass-independent fractionation of sulfur isotopes (e.g., Bekker et al. 2004; Konhauser et al. 2011). These findings were used to argue that Cr was extensively solubilized, yet Cr isotope fractionations do not support extensive aqueous  $\text{Cr}^{4+}$  transport during that time, arguing against oxidative weathering (e.g., Frei et al. 2009). Rather, Cr had to be mobilized in its reduced  $\text{Cr}^{3+}$  form. Microbially catalysed oxidation of crustal pyrite is then the most likely candidate to have generated the degree of acidity needed for  $\text{Cr}^{3+}$  to solubilize in sufficient quantity (e.g., Rai et al. 1989). This suggests that the  $\text{Cr}^{3+}$  pulse at  $\sim 2.48$  Ga shows the beginning of bacteria utilizing  $\text{O}_2$  to oxidize the previously stable crustal pyrite reservoir (e.g., Konhauser et al. 2011).

### **Rare Earth Elements**

Shale-normalized rare earth element and yttrium (REE + Y, or REY) patterns are a popular tool for investigating depositional environments for IFs. These elements show similar behaviour as they display a constant ionic charge ( $\text{REE}^{3+}$ ). Differences are, therefore, only linked to their ionic radii, with the exceptions of Ce and Eu, which are redox-sensitive and may occur as  $4+$  and  $2+$  respectively. Rare earth elements + yttrium patterns in literature are generally reported normalized to a post-Archean shale value (suffix PAAS; e.g., McLennan 1985). This is done because the REY distribution in Post-Archean shales is relatively constant and the normalization makes deviations in observed patterns more pronounced (e.g., Nance and Taylor 1976; Bau and Dulski 1996). Under oxidizing conditions, Ce can be oxidized from  $\text{Ce}^{3+}$  to  $\text{Ce}^{4+}$ , greatly reducing its solubility, leading to negative anomalies in the REY patterns. On the other hand, Eu can be reduced from  $\text{Eu}^{3+}$  to  $\text{Eu}^{2+}$  in high temperature ( $>250^\circ\text{C}$ ) hydrothermal vent systems, causing positive anomalies of Eu relative to other REE in hydrothermal fluids (e.g., Bau and Dulski 1999). In low temperature, aqueous systems, light REE show a much higher sorption affinity relative to heavy REE, which can lead to deviations from expected patterns. REY patterns are, therefore, able to account for high-temperature, hydrothermal, and low-temperature aqueous processes.

Interpretation of REY patterns of iron formations are based on the observations REY in modern seawater. Although not consistent through time, iron formations generally show features in REY patterns that strongly resemble those observed in the pattern for modern seawater:

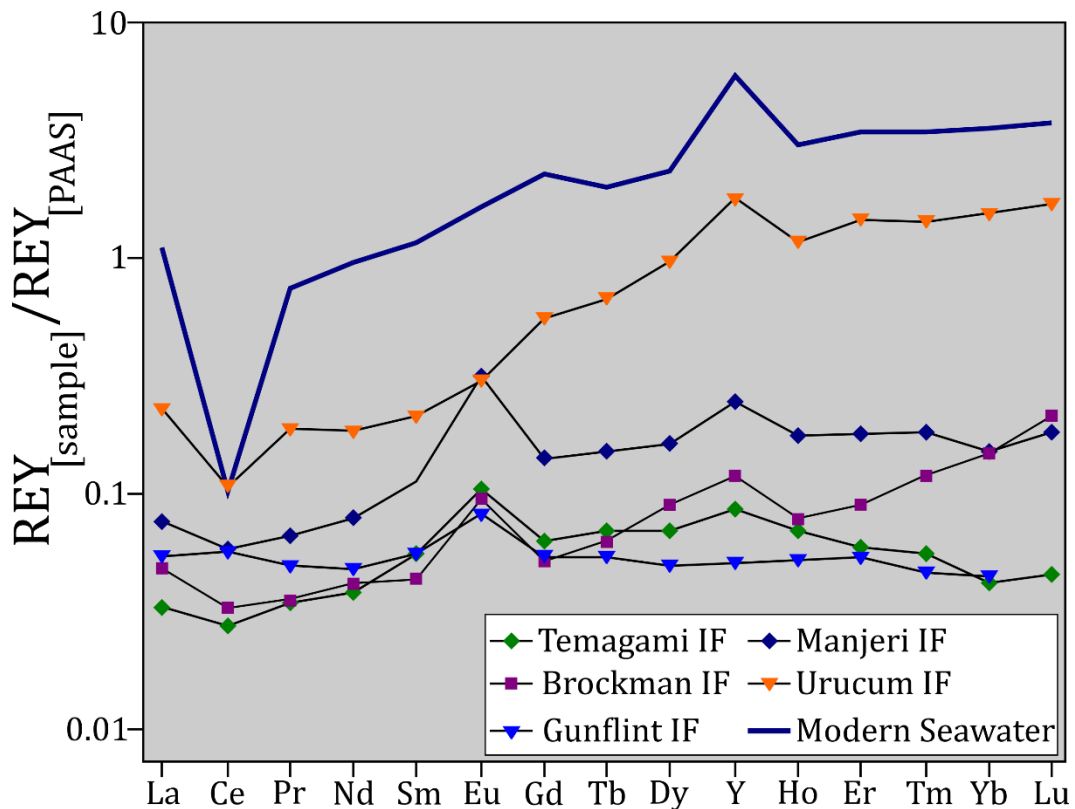


**Figure 1.8:** Shale-normalized REY pattern of selected Archean (the 2.7 Ga Temagami and Manjeri IF), Paleoproterozoic (the ~ 2.4 Ga Brockman and the 1.88 Ga Gunflint IF) and Neoproterozoic (the ~ 590 Ma Urucum IF) iron formations, and modern-day seawater. REY patterns of the Temagami, Manjeri, Gunflint, and Brockman IF were taken from Planavsky et al (2010). REY pattern of the Urucum IF was taken from Viehmann et al. (2016). REY pattern of modern seawater from Douville et al. (2002).

- (I) Light REE depletion: In oxygenated marine settings, light REE are preferentially removed relative to heavy REE due to the preferential adsorption of light REE onto particle-reactive surfaces, especially Mn-Fe oxyhydroxides. Due to reductive dissolution of Mn-Fe oxyhydroxides, the  $REE_{light}/REE_{heavy}$  ratio increases significantly across the redox boundary (e.g., German et al. 1991).
- (II) Superchondritic Y/Ho ratios: Y/Ho ratios are significantly higher in aqueous fluids and precipitates compared to igneous rocks and epiclastic sediments, where they are near-chondritic (e.g., Nozaki et al. 1997; Bau and Dulski 1999). Yttrium is less particle reactive than Ho, leading to superchondritic Y/Ho ratios in marine fluids and its precipitates. In anoxic waters, where Mn-Fe rich particles dissolve, the Y/Ho ratios decrease due to the increase in Ho (e.g., Planavsky et al. 2010).

- (III) Cerium anomalies: Generally, oxygenated marine settings show a strong negative Ce anomaly when normalized to a shale composite ( $Ce_{SN}$ ), while suboxic and anoxic waters lack a negative Ce anomaly. This is due to the oxidation of  $Ce^{3+}$  to the less soluble  $Ce^{4+}$  on particle surfaces and subsequent removal of Ce from solution (e.g., Bau and Koschinsky 2009).
- (IV) Eu anomalies: In high temperature ( $>250^{\circ}C$ ) hydrothermal fluids, Eu is typically enriched relative to other REE and present as  $Eu^{2+}$ . During mixing of ocean water and the hydrothermal fluids, Eu from the high-temperature fluid is oxidized to  $Eu^{3+}$  and added to the  $Eu^{3+}$  already present, resulting in higher concentrations (e.g. Bau 1993). Enrichment in Eu in chemical sediments precipitated from seawater is, therefore, considered an indication for a strong influence of hydrothermal vent fluids on the seawater (e.g., Danielsson et al. 1992; Viehmann et al. 2015a).

Iron formations preceding the GOE generally show depletion in light REE, a high Y/Hi ratio, a lack any form of Ce anomaly and a pronounced positive Eu anomaly. This implies the lack of a discrete redoxcline in the Archean and early Paleoproterozoic oceans, and that the  $Fe^{2+}$  oxidation mechanism was independent from  $O_2$ . Hydrothermal vent systems were also significantly higher and played a major contribution to the REY budget of the iron formations. This interpretation is further supported by the lack of Ce anomalies in shallow water carbonates from Archean carbonate platforms (e.g., Planavsky et al. 2010). In contrast, Paleoproterozoic iron formations deposited after the GOE show negative Ce anomalies, a significant range in  $REE_{light}$  to  $REE_{heavy}$  ratios, and Y/Ho ratios which can both be both higher and lower than the comparative shale value. They either show only faint Eu anomalies or none, hinting that the influence of high-temperature hydrothermal vent fluids was greatly diminished (e.g., Konhauser et al. 2017). This supports varying redox conditions in the various late Paleoproterozoic basins and oceans and the presence of a strong redoxcline, separating an upper oxic layer from a deeper, suboxic to anoxic water layer (e.g., Planavsky et al. 2009, 2010).

Neoproterozoic iron formations generally show a small depletion of light REE and superchondritic Y/Ho ratios. There is no consistency concerning negative Ce or positive Eu anomalies (e.g., Gaucher et al. 2015; Cox et al. 2016; Viehmann et al. 2016). The Eu anomalies observed in Neoproterozoic iron formations do not resemble that of a hydrothermal vent (e.g., Cox et al. 2013), however, that does not imply the absence of such systems. Rather, the small positive Eu anomalies and the absence of such are seen as an indicator for the presence of low temperature ( $<250^{\circ}C$ ), hydrothermal vent systems (e.g., Alexander et al. 2008). Hence, their deposition environment is characterized by reducing, ferruginous conditions, with distal hydrothermal vent sources.

#### 1.2.1.4.2 Isotope geochemistry

Isotope geochemistry uses the partitioning of isotopes (atoms of an element with different number of neutrons) between phases or chemical species as a tool to advance the understanding of geochemical and geological processes. The general distinction is between systems where the isotopes do not decay over time (stable isotope systems) and systems where one of the isotopes is radioactive (the nuclei decay over time: radiogenic isotope systems). Stable isotope systems are further divided into traditional stable isotope systems, composed of the light elements of H, C, N, O, and S, and the non-traditional stable isotope systems, which encompass a variety of metals (e.g., Li, Mg, Cu, Fe, Zn), metalloids (e.g., Bi, Si, Ge) and non-metals (e.g., Cl, Se, Br) with a greater atomic mass (e.g., Hu and Teng 2021; Stern and Wieman 2021).

In the study of iron formations, various stable isotope systems have been utilized to gain understanding of the palaeoenvironmental characteristics through time (e.g., Robbins et al. 2016; Mänd et al. 2022), while fewer radiogenic isotope systems have been used mostly for radiometric age dating (e.g., the Rb-Sr, Sm-Nd, and Re-Os isotopic system; e.g., Johnson et al. 2013; Viehmann et al. 2013, 2015a, 2015b, 2016; Schulz et al. 2021; Usma et al. 2021). Isotopic systems of redox-sensitive elements especially are a valuable tool, as they can act as tracer for the evolution of oxygen in Earth's atmosphere and oceans. The following paragraphs will present a brief description of the most important isotope systems for IF research:

#### **Stable isotope systems**

Data for stable isotope systems are typically expressed in terms of the delta ( $\delta$ ) notation, the relative difference in parts per thousand (‰) between the isotope ratio of a sample and that of a standard reference material. Oxygen and carbon are two traditional stable isotope systems that have been popular tools in the study of iron formations.

Oxygen isotope compositions of IF-related chert has been used to study a variety of paleoconditions, such as Precambrian ocean temperatures, source of silica in IFs, and degree of metamorphic overprint (e.g., Mänd et al. 2022, and references therein). Chert in Paleoarchean IFs show  $\delta^{18}\text{O}$  values  $< +22\text{‰}$  Standard Mean Ocean water (SMOW), increasing towards the Phanerozoic, which was interpreted as evidence for increased seawater temperatures of Archean oceans (e.g., Knauth and Lowe 2003). However, more recent works support the idea that secular changes in the oxygen isotopic composition are more likely caused by changes in the seawater composition (e.g., Mänd et al. 2022 and references therein).

Carbon isotope studies in IFs have been used to further understand the genesis of IFs. Carbonates associated with IFs tend to be isotopically light (depleted in  $^{13}\text{C}$ ), with most values ranging from  $-8$  to  $-6\text{‰}$  against Vienna Pee Dee Belemnite (V-PDB, e.g., Johnson et al. 2008; Heimann et al. 2010). Petrographic evidence as well as oxygen isotope studies suggests that most Fe-rich carbonates in IFs were formed during late diagenesis (e.g., Heimann et al. 2010). Their formation is therefore considered to be linked to fermentative metabolism and anaerobic respiration of microorganisms in the anoxic water column and sediments (e.g., Perry et al. 1973; Walker 1984). Dissimilatory iron reduction (DIR) coupled with complete C and Fe retention in sediments is a popular invoked mechanism (Heimann et al. 2010). While this is the most popular model, other plausible explanations have been proposed (e.g., Konhauser et al. 2005; Beal et al. 2009; Crowe et al. 2011).

Non-traditional stable isotopic systems have seen a steady increase of interest in the last several years, in part due to great advancements in analytical instruments.

Chromium isotope fractionation (expressed as  $\delta^{53}\text{Cr}$  values) most severely occurs during the oxidation of  $\text{Cr}^{3+}$  through oxidative weathering, resulting in the production of aqueous and soluble  $\text{Cr}^{4+}$  (e.g., Frei et al. 2009, Wei et al. 2020). Oxidation of  $\text{Cr}^{3+}$  and the transport of the fractionated  $\text{Cr}^{4+}$  to the oceans in turn require the generation of  $\text{Mn}^{4+}$ -oxides during weathering as well as the absence of  $\text{Fe}^{2+}$  in rivers. Therefore, fractionation of  $\delta^{53}\text{Cr}$  values in sediments has been seen as a potential proxy for atmospheric oxygenation (e.g., Frei et al. 2009). Iron Formations show positive deviations from igneous background  $\delta^{53}\text{Cr}$  composition, which have been interpreted as an indicator for short-lived oxygen peaks in the Precambrian atmosphere (e.g., Frei et al. 2009; Crowe et al. 2013). However, the interactions are not as straight forward, and complications need to be taken into account (as, for example, modern weathering in outcrops is able to affect the primary Cr budget significantly; e.g., Albut et al. 2018; Heard et al. 2021).

The iron isotopic signature (usually expressed as  $\delta^{56}\text{Fe}$ ) is an obvious choice and has been used since decades to track the biogeochemical cycling of iron and paleoredox conditions on early Earth (see, for example, references in Bekker et al. 2014). Samples of IFs have shown a large variety of  $\delta^{56}\text{Fe}$  values (e.g., Dauphas et al. 2017; Huang et al. 2021). Positive  $\delta^{56}\text{Fe}$  values can be found in almost all Archean and Paleoproterozoic IFs, while IFs younger than 3.0 Ga show negative  $\delta^{56}\text{Fe}$  values (e.g., Dauphas et al. 2017; Huang et al. 2021; Mänd et al. 2022, and references therein). Positive, heavy  $\delta^{56}\text{Fe}$  values are considered to reflect partial  $\text{Fe}^{2+}$  oxidation (only portion of the dissolved Fe was oxygenated) and  $\text{Fe}^{3+}$  mineral precipitation (e.g., Dauphas et al. 2017). On the other hand, negative  $\delta^{56}\text{Fe}$  values have been explained as reflecting the progressive oxidation of hydrothermal fluids following a Rayleigh fractionation-type model, depleting them of heavy Fe isotopes (e.g., Dauphas et al. 2017 and references

therein; Huang et al. 2021). Another possible explanation for light  $\delta^{56}\text{Fe}$  values in IFs is the near-quantitative oxidation of  $\text{Fe}^{2+}$  via dissimilatory iron reduction (DIR). However, there is still much debate and uncertainties concerning the Fe isotope mass-balance of BIFs, requiring more work to better understand their influences.

Molybdenum isotopes (usually expressed  $\delta^{98}\text{Mo}$ ) fractionate drastically by adsorption onto manganese oxides under oxic conditions, allowing for the quantification of the redox conditions in the oceans (e.g., Barling and Anbar 2004). In iron formations,  $\delta^{98}\text{Mo}$  values have been primarily used to track local  $\text{Mn}^{4+}$  oxide formations, as they indicate the presence of oxygen oases in otherwise anoxic oceans (e.g., Planavsky et al. 2014). Recently, Goto et al. (2020) proposed a quantitative model for estimating  $\delta^{98}\text{Mo}$  values of seawater from measured values of IFs combined with their Fe/Mn ratios, as these two variables show an anti-correlation. Ultimately, this could lead to iron formations being able to assess the global balance of redox conditions on the seafloor.

While the U-Th-Pb isotopic system is one of the oldest and most refined radiometric dating systems, the “stable” uranium isotope system (expressed as  $\delta^{238}\text{U}$ ) has recently seen development as a proxy for palaeoredox conditions (e.g., Lau et al. 2019). Fractionation of  $\delta^{238}\text{U}$  is significant during the biotic reduction of soluble  $\text{U}^{4+}$  to the insoluble  $\text{U}^{6+}$  in anoxic sediments. Similar to  $\delta^{98}\text{Mo}$ , marine  $\delta^{238}\text{U}$  values show a negative correlation with the areal extent of anoxic conditions on the seafloor (e.g., Andersen et al. 2014; Mänd et al. 2022). While this is a promising start, more research needs to be done, as the incorporation of U in iron formations is still poorly understood (e.g., Skomurski et al. 2011; Wang et al. 2018).

## **Radiogenic isotope systems**

Radiogenic isotope geochemistry has two principal uses. The first is geochronology, where the constant rate of radioactive decay of an isotope is used to measure timespans. It is a fundamental understanding of nature and has seen applications in many fields of science (e.g., White 2015). The second application is for tracer studies, where differences in the ratio of the radiogenic daughter isotope to other isotopes of the element are used to provide insights into the formation and evolution of the Earth and other cosmic bodies.

In iron formations, radiogenic isotope systems have primarily been used to constrain the geochemical influences on the water bodies from which the IFs precipitated. The Re-Os isotopic system is discussed separately (see Chapter 1.3.2)

The Rb-Sr isotopic system is based on the beta decay of  $^{87}\text{Rb}$  to  $^{87}\text{Sr}$ . Rubidium has a large ionic radius and is among the most incompatible elements. Hence, it is strongly concentrated in the Earth's crust and depleted in its mantle. Strontium is also an incompatible element, but not as highly, as it can comfortably substitute for Ca in several minerals. The high fluid mobility

of both Rb and Sr makes the Rb-Sr system an unattractive choice for geochronology (e.g., White 2015). However, Sr isotope ratios can be used to date sediments. Sr has a long residence time in the ocean and variations in the  $^{87}\text{Sr}/^{86}\text{Sr}$  ratios are relatively uniform geographically. Hence, changes of the  $^{87}\text{Sr}/^{86}\text{Sr}$  ratio in seawater can be plotted over geological time. By comparing the  $^{87}\text{Sr}/^{86}\text{Sr}$  ratios of seawater derived sediments with the Sr isotope seawater curve, one can determine the influence of mantle derived vs continental input during the time of deposition (for more details, see Chapter 1.3.2). In the research of iron formations, the Sr isotope ratios seen use in determination of the Sr isotope composition of the Precambrian seawater from which they precipitated and, in some cases, to determine their age in combination with other dating methods (e.g., Johnson et al. 2013; Usma et al. 2021). Fe-normalized Sr concentrations of IF samples are also a popular to monitor the impact of postdepositional alteration (e.g., Schulz et al. 2021).

The Sm-Nd isotopic system is based on the alpha decay of  $^{147}\text{Sm}$  to  $^{143}\text{Nd}$  with an extremely long half-life of 106 Gy. Both samarium and neodymium are intermediate rare earth elements and share similar geochemical behaviours (see Chapter 1.2.1.4.1). Both elements are considered insoluble in aqueous phases and slightly incompatible, with Nd being slightly more incompatible (e.g., White 2015). The Sm/Nd ratio is little affected by weathering, making the Sm-Nd isotopic system popular in dating fine grained sediments and computing crustal residence times (e.g., White 2015). Samarium-Nd measurements have been used in dating the deposition time of iron formations as well as a proxy for the source contribution to the ancient seawater (e.g., Shimizu et al. 1990, Viehmann et al., 2013, 2015b, 2016).

The Lu-Hf isotopic system utilizes the beta decay of  $^{176}\text{Lu}$  to  $^{176}\text{Hf}$ . Lutetium is the heaviest rare earth element, while hafnium is a member of the IVB elements, which include Ti and Zr, and shares chemical similarities with both elements (especially Zr). Like Sm and Nd, both Lu and Hf are considered insoluble and immobile, but the Lu-Hf system has some advantages to the Sm-Nd system. Most notably, the half life of  $^{176}\text{Lu}$  is noticeably shorter ( $t_{1/2} = 37$  Gy) than that of  $^{147}\text{Sm}$ . Secondly, common rocks and minerals show larger variations in their Hf isotopic composition compared to their Nd isotopic composition, as Lu and Hf show different geochemical behaviour, while Sm and Nd behave similar (as both are REE). Due to the chemical similarities between Hf and Zr, Hf is concentrated in zircon, a robust and popular mineral used in radiogenic dating (e.g., White 2015). In iron formation research, the Lu-Hf system has been used occasionally to provide further information on depositional ages (e.g., Sun et al. 2023).

The Hf-W isotopic system is a recent addition to the research of BIF. It utilizes the decay of the now extinct  $^{182}\text{Hf}$  to  $^{182}\text{W}$  with a half life of 8.9 Ma. This isotopic system is uniquely useful for early Earth accretion and differentiation. Hafnium is lithophile, while W shows siderophile behaviour. During the differentiation of early Earth, most of the Earth's W partitioned into the

metallic core, while Hf remained in the Earth's silicate mantle. Hence, the mantle evolved a high Hf/W ratio and  $^{182}\text{W}/^{184}\text{W}$  ratio (e.g., Kleine and Walker 2017). Because W concentrations in modern seawater are homogenous and Mn-oxides and  $\text{Fe}^{3+}$ -oxyhydroxides are major W sinks (e.g., Kashiwabara et al. 2017), the W isotope composition of seawater depends on the W flux from various sources. This, in turn, implies that seawater derived sediments, such as BIFs, directly reflect the W isotopic composition of seawater during time of precipitation, allowing the study of the geodynamic evolution of Earth's mantle and continents through time. Mundl-Petermeier et al. (2022) provided the first high precision  $^{182}\text{W}$  isotope data of the 2.7 Ga Temagami iron formation, Canada. They found distinct differences in the W isotope composition of the alternating chert and magnetite layers, concluding that BIFs may be able to track the geodynamic evolution of the crust-mantle system through Precambrian times.

### 1.3 Highly siderophile elements and the Re-Os Isotopic system

#### 1.3.1 Highly siderophile elements

Highly siderophile elements (HSE) are a group of d-group elements that show a strong affinity to partition into metal and sulfide relative to silicate. If metals are absent, they behave chalcophile and concentrate in sulfides (e.g., Day et al. 2016 and references therein). They are comprised of Re, Au and the six transition metals of the platinum group (PGE). Platinum group elements can further be sub-divided into the iridium-group (I-PGE: Os, Ir, Ru, Rh) and the platinum-group PGE (P-PGE: Pt, Pd). Highly siderophile elements are generally enriched in the mantle relative to the crust.

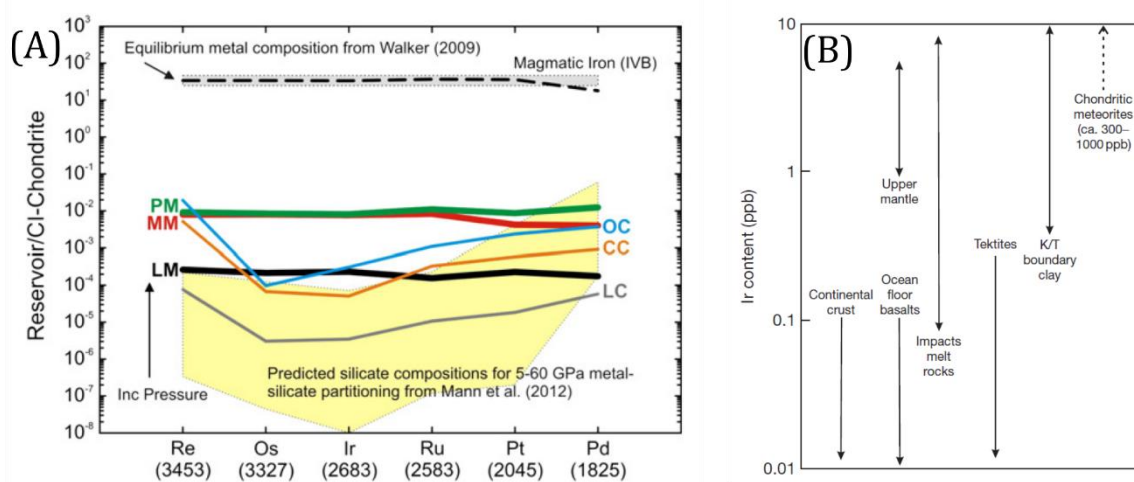


**Figure 1.9:** Baseline distribution of HSE (with the exception of Re and Au) in different core, mantle, and crust reservoirs of the Earth, Moon, and Mars (A), and range of Ir concentrations in terrestrial and extraterrestrial

materials (B). PM = primitive mantle, MM = martian mantle, LM = lunar mantle, OC = terrestrial oceanic crust, CC = terrestrial continental crust, LC = lunar crust. (a) from Day et al. (2013), (b) from Koeberl (2014).

Because of their strong affinity for iron, it was assumed that the silicate Earth was largely depleted of HSE during core formation, although the true extent remains uncertain (e.g., Righter et al. 2000; Brenan et al 2016). However, Re/Os and Pt/Os ratios of the terrestrial mantle are within  $\sim \pm 5\%$  and  $\sim \pm 10\%$  of chondritic values, respectively (Fig. 1.9A). Several models have been proposed to account for these discrepancies. Many authors argue in favour of the “late-veener” hypothesis, a late accretion or “veener” of chondritic material after the major phases of core formation of Earth (and the Moon) (e.g., Chou 1978; Morgan et al. 2001). Highly siderophile elements provide geochemical tools for the identification of meteoritic components in impact melt rocks or extraterrestrially contaminated seawater sediments, for core-mantle interaction (in form of the Pt-Os isotope system), and for radiogenic dating (in form of the Re-Os isotopic system, see below for detailed discussion). Detection of meteoritic components via HSE is possible because of the distinctively higher concentrations of HSE in chondritic (and iron) meteorites compared to the continental crust (Fig. 1.9B; e.g., e.g., Koeberl 2014). Hence, elevated HSE concentrations in terrestrial rocks are an indication for a meteoritic component. Iridium is most commonly used as chemical impact marker, with a variety of techniques available (e.g., Koeberl 2014).

#### 1.3.1.1 *Highly siderophile elements in seawater*

Compared to the UCC (upper continental crust), the abundance of HSEs in modern seawater is extremely low (see Appendix 8-2). They are  $\sim 7$  ppt for Re,  $\sim 0.01$  ppt for Os (Stein and Hannah 2014), range from  $\sim 0.04$  to  $\sim 0.30$  ppt for Pt (Mashio et al. 2017), from  $\sim 0.001$  to  $0.003$  ppt for Ir (Li et al. 2007), are  $\sim 3$  to  $11$  ppt for Ru (e.g., Koide et al. 1987), and range from  $\sim 0.02$  to  $0.07$  ppt Pd (Lee 1983). They are present as a mixture of organic complexes, colloids, nanoparticles, aqueous clusters, and organic complexes (e.g., Seward 1989). Whereas Re is highly soluble under oxidizing conditions, occurring as an unreactive  $\text{ReO}_4^-$  oxyanion (e.g., Anbar et al. 1992; Colodner et al. 1993) with comparably long residence times of  $750.000\text{y}$  (e.g., Colodner et al. 1993), Os occurs as dissolved  $\text{H}_3\text{OsO}_6^-$  (e.g., Sharma et al. 1997),  $\text{H}_2\text{OsO}_5$ , or  $\text{OsCl}_6^{2-}$  (e.g., Koide et al. 1991), with a residence time of  $\sim 28.000\text{y}$  (e.g., Paquay and Ravizza 2012). Pt can also be transported in solution to some extent in form of the chloride complex  $\text{PtCl}_5(\text{OH})^{2-}$  (e.g., Mashio et al. 2017). Ir is less soluble and its behaviour in natural water is still poorly understood (e.g., Siebert et al 2005; Li et al. 2007). The concentrations of the HSE are sufficiently higher in the suspended load (the part of the sediment that is uplifted by the water's flow) than in the dissolved load due to fact that HSE may still be adsorbed onto clay particles (e.g., Southam et al. 2009).

Marine environments attribute their highly siderophile elements content to a variety of crustal, mantle and cosmic sources. Crustal sources, therefore, generally display low concentrations of HSE but have a more radiogenic (positive) isotopic composition (because Os is highly compatible and Re is incompatible during mantle melting; see discussion below) than the mantle sources, as they accumulate more radiogenic isotopes over time. The influence an input of the various sources is not constant over geological time, as seen at the dynamic nature of the marine Os isotope record (see discussion below). Continental (crustal) sources dominate the modern-day HSE seawater budget and are responsible for up to 80% of the HSE content in seawater (e.g., Hannah and Stein 2012). The major contribution to marine HSE is the input of continents via riverine runoff. Rivers provide marine waters with continental sourced HSE, which typically displays radiogenic (positive) isotopic values. However, concentration and isotopic composition is not uniform for river waters and depends on the terrain from which they receive their drainage (e.g., Peucker-Ehrenbrink and Ravizza 2000). Atmospheric contribution via dissolution of aeolian dust in seawater is another source which primarily provides HSE of radiogenic isotopic composition. While concentrations of highly siderophilic elements in aeolian dust is generally considered to be low, the extent and volume of input into the seawater still is largely unknown (e.g., Peucker-Ehrenbrink and Ravizza 2000). Mantle derived HSE is delivered into the oceans primarily via the alteration of oceanic mantle-derived rocks through the interaction with high-temperature submarine hydrothermal fluids. Abyssal peridotites show elevated concentrations of HSE compared to crustal rocks and an unradiogenic isotopic composition, making them an appealing source. However, the effect of hydrothermal fluid circulation through the oceanic crust on the seawater budget has not been quantified (e.g., Peucker-Ehrenbrink and Ravizza 2000). Extraterrestrial input via the dissolution of cosmic dust is a significant source of the HSE in continental surface environments. In modern seawater, it provides a constant annual flux comparable to that of hydrothermal sources (e.g., Stein and Hannah 2012). However, as the marine Os record shows dynamic behaviour, the constant extraterrestrial flux is not seen as a main HSE contributor in seawater. However, large impact can deliver large volumes of highly siderophile elements in a short amount of time and lead to significant anomalies on the HSE record through time (e.g., Peucker-Ehrenbrink and Ravizza 2000).

### 1.3.2 The Re-Os isotopic system

Naturally occurring rhenium is composed of two isotopes:  $^{185}\text{Re}$  (37.398%) and  $^{187}\text{Re}$  (62.602%). Osmium has seven naturally occurring isotopes:  $^{184}\text{Os}$  (0.02%),  $^{186}\text{Os}$  (1.59%),  $^{187}\text{Os}$  (1.96%),  $^{188}\text{Os}$  (13.24%),  $^{189}\text{Os}$  (16.15%),  $^{190}\text{Os}$  (16.26%) and  $^{192}\text{Os}$  (40.78%), whereas  $^{187}\text{Os}$  is the product of beta-decay of  $^{187}\text{Re}$  with a decay constant of  $\lambda = 1.666 \times 10^{-11} \text{ year}^{-1}$

(corresponding to a half-life of 41.6 Gy; Smoliar 1996). There are still uncertainties in the Re decay constant, but they have been greatly reduced by back-calculating the decay constant from Re-Os systematics of already well dated iron-meteorites (3% uncertainty in the 1990's to  $\pm 0.31\%$  today; e.g., Shen et al. 1996; Smoliar et al. 1996). Rhenium and Os both exhibit siderophile and chalcophile tendencies and strongly partition into metals and sulphides in magmatic systems (see discussion above). They show slightly different geochemical behaviour, with Os being highly compatible in mantle sulphides and metal alloys and Re being only mildly compatible. This leads to large elemental fractioning, as Re is transferred more efficiently into the crust than Os during partial melting (e.g., Reisberg and Lorand 1995), leading to high and variable Re/Os ratios in crustal reservoirs (averaging around 50, being up to three magnitudes higher than mantle ratios). Due to the radioactive decay of  $^{187}\text{Re}$ , high Re/Os ratios can cause significant ingrowth of radiogenic  $^{187}\text{Os}$ , producing an enormous range of  $^{187}\text{Os}/^{188}\text{Os}$  ratios in crustal materials that are orders of magnitude higher compared to the mantle and extraterrestrial reservoirs (i.e., meteorites). The Re-Os system is, therefore, an effective tool to distinguish crustal reservoirs, with show high Re/Os ratios, from mantle reservoirs, which show low-Re/Os (e.g., Stein and Hannah 2014).

Besides disentangling source contributions in marine reservoirs, the Re-Os isotope system can also be used for age dating (more specifically, dating the time since the host-rock was equilibrated with and derived from its source; e.g., White 2015).

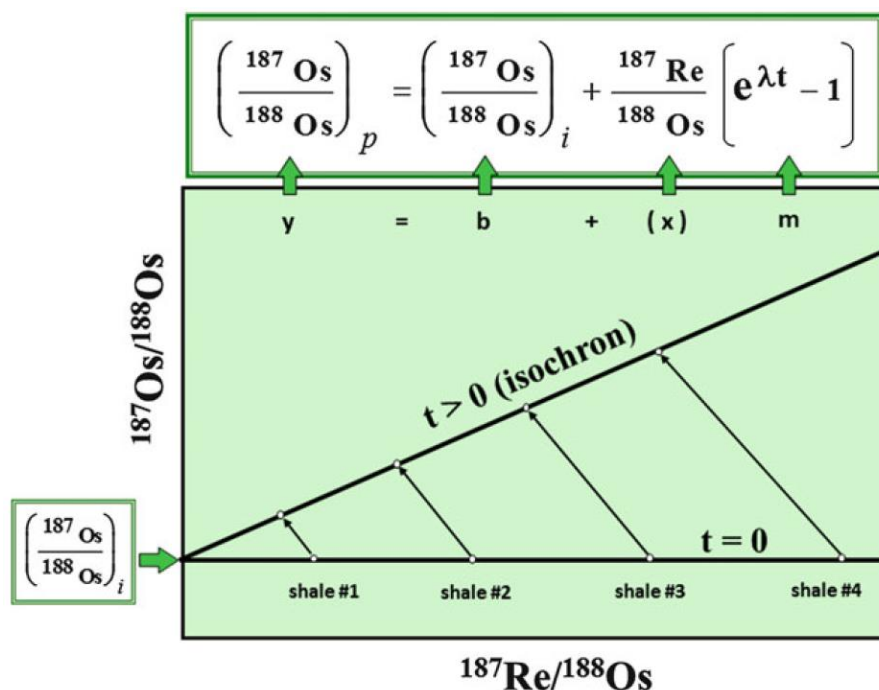


**Figure 1.10:** An example Re-Os isochron plot with four shale samples. Minerals, mineral separates or whole-rock samples (from a suite of co-magmatic rocks) acquired the same initial  $^{187}\text{Os}/^{188}\text{Os}$  ratios at the time of the last isotope equilibration (e.g., crystallization, deposition) but, due to different  $^{187}\text{Re}/^{188}\text{Os}$  ratios, evolve over time to different present-day  $^{187}\text{Os}/^{188}\text{Os}$  ratios (which are measured in the mass spectrometer; see Method section). This implies an isotopically closed

system. The slope of the isochron ( $m$ ) is a function of the age of the sample and the decay constant, while the  $y$ -intercept ( $y$ ) is the initial  $^{187}\text{Os}/^{188}\text{Os}$  at  $t = 0$ . From Stein and Hannah (2014).

Fig. 1.10 shows the basic age equation for the Re-Os isotope system. The measured ratios are determined via mass spectrometry,  $\lambda$  is the known decay constant of  $^{187}\text{Re}$ , leaving us with two unknowns: the desired age ( $t$ ) of the sample in years, and the initial  $^{187}\text{Os}/^{188}\text{Os}$  ratio during time of sample equilibration. The initial  $^{187}\text{Os}/^{188}\text{Os}$  ratio of a sample cannot be determined analytically but can be back-calculated whenever the Re/Os ratio and the age of the sample are known. However, without a known age, the initial  $^{187}\text{Os}/^{188}\text{Os}$  can be calculated from the intercept of an isochron in a  $^{187}\text{Re}/^{188}\text{Os}$  versus  $^{187}\text{Os}/^{188}\text{Os}$  diagram (Fig. 1.10).

#### 1.3.2.1 *The marine osmium isotope record*

Both Re and Os are redox-sensitive elements. They are mobile under oxidizing conditions and immobile under reducing, anoxic to euxinic, low-temperature conditions (Stein and Hannah 2015). In marine settings, the Os isotopic composition is the result of various Os sources in the seawater. While oxidative weathering of the crust (i.e., crustal alteration) contributes a typically “radiogenic/low Os” ( $^{187}\text{Os}/^{188}\text{Os}$  of  $\sim 0.5$  to  $1.0$  with around 30-60 ppt Os; see Peucker-Ehrenbrink et al. 2000) signature to the marine Os-budget either as dissolved riverine runoff or detrital input, mantle-derived sources, such as hydrothermal vent systems (black smokers) in the deep sea, typically contribute a far less radiogenic (near chondritic) but higher abundance Os signal ( $^{187}\text{Os}/^{188}\text{Os}$  of  $\sim 0.12$  to  $0.2$  with komatiitic Os concentrations of a few hundred ppt to a few ppb Os; e.g., Day et al. 2013). In addition, extraterrestrial sources (meteorite impacts or cosmic dust) could -in principle- contribute a chondritic contribution ( $^{187}\text{Os}/^{188}\text{Os}$  of  $\sim 0.12$  and Os abundances of up to 600 ppt Os, depending on the impactor type; see, for example, Tagle and Berlin 2008) to the Os seawater budget. Thus, different contributions of these sources (to the seawater) through time lead to variations in the marine Os isotope (and Os concentration) signature.

By plotting the  $^{187}\text{Os}/^{188}\text{Os}$  ratio versus age it is possible to monitor the secular variations in the marine Os budget through time. This Os isotope seawater curve has often been compared to the isotope seawater curve of Sr, which is the most widely used and robust proxy for changes in silicate weathering (e.g., Peucker-Ehrenbrink and Ravizza 2012). Osmium exhibits a residence time in the oceans of around 28,000 y (although still discussed, e.g., Paquay and Ravizza 2012; Georg et al. 2013), which is longer than the mixing time of the oceans ( $\sim 1,000$  -  $2,000$  y; e.g. Holland 1984), but shorter than that of Sr ( $\sim 2$  m.y.; e.g., Richter and Turekian 1993; Peucker-Ehrenbrink and Ravizza 1996). Thus, Os can be expected to be well mixed in the oceans (e.g., Stein and Hannah 2014, and references therein), but still be prone to short-

term effects (Fig. 1.12A), such as bolide impacts (e.g., the Chicxulub impact event at the K-Pg boundary at around 65.05 Ma; e.g., Renne et al. 2013; Sprain et al. 2018), glacials – interglacials cycles (e.g., less radiogenic values coinciding with the height marine isotope stages 2 and 6 at ~20 k.y. and ~ 160 k.y. respectively; Petit et al. 1990) or the erosion of mafic igneous provinces (e.g., the Deccan flood basalts around 67 Ma to 64 Ma; Ravizza and Peucker-Ehrenbrink 2003).

Neither Re nor Os were largely mobilized in the anoxic surface environment of the Archean (e.g., Hannah et al. 2004), although a recent study by Schulz et al. (2021) from the 2.7 Ga Temagami BIF provided evidence for (at least partial) mobilization of Re and Os from terrigen environments. Still, continental Re (and radiogenic  $^{187}\text{Os}$ ) predominantly accumulated and sequestered in organic-rich sedimentary rocks. Osmium isotope balance is therefore strongly controlled by weathering of organic-rich sediments, providing complementary data to the Sr seawater curve, which in turn is strongly influenced by weathering of carbonates and silicates (e.g., Ravizza 2007). Together, both elements can monitor the potential causes of changes in the marine chemistry through time (e.g., Hanna and Stein 2014). Temporal variations in the  $^{187}\text{Os}/^{188}\text{Os}$  ratio of seawater can span entire ranges of magnitude (e.g., Peucker-Ehrenbrink and Ravizza 2000), compared to in the  $^{87}\text{Sr}/^{86}\text{Sr}$  ratio in seawater, which is smooth and less sensitive due to the longer residence time of Sr in the oceans (2 Ma, McArthur et al. 2000).

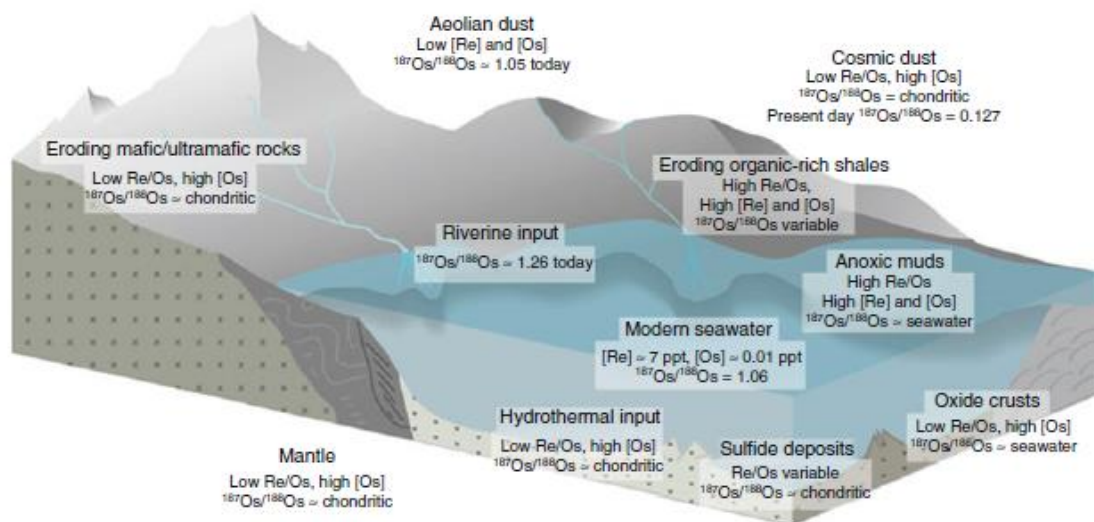


**Figure 1.11:** Re and Os concentrations and Re/Os ratios of sources and sinks of Re and Os in seawater. From Stein and Hannah (2014)

Current available Os isotope data allows the high-resolution reconstruction of the marine  $^{187}\text{Os}/^{188}\text{Os}$  back into the Mesozoic (Fig. 1.12B). The K-Pg boundary, the most prominent excursion in the Os record, is associated with the impact of an asteroid with carbonaceous chondrite composition, which delivered up to  $1 \times 10^9$  mole extraterrestrial, unradiogenic Os (e.g., Peucker-Ehrenbrink and Ravizza 2000 and references therein). The large influx of

unradiogenic Os decreased the Os isotopic composition from close to 0.6 to meteoritic or mantle-like values of 0.2 to 0.15 (e.g., Peucker-Ehrenbrink and Ravizza 2012).

Another prominent excursion from radiogenic to unradiogenic values is observed in the late Eocene, with a rapid shift to an unradiogenic Os ratio (like at the K-Pg boundary), which again coincides with elevated Os and Ir concentrations, possibly linking the excursion to impact events at Chesapeake Bay and Popigai (e.g., Koeberl et al. 2001; Peucker-Ehrenbrink and Ravizza 2012, and references therein).

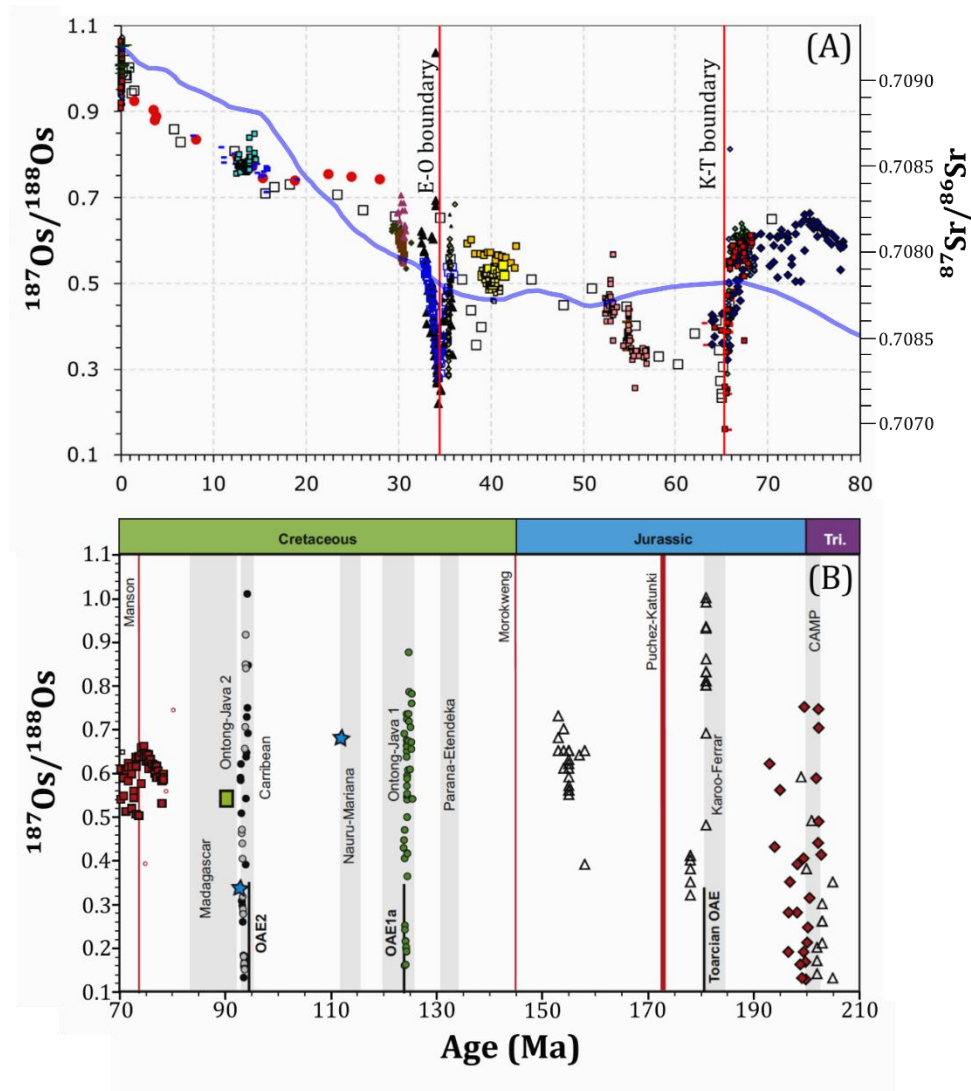


**Figure 1.12:** (A) “Best” published  $^{187}\text{Os}/^{188}\text{Os}$  data for paleoseawater of the past 80 million years. The Sr isotopic evolution curve for the same time frame is displayed in pale blue. For data sources, see Peucker-Ehrenbrink and Ravizza (2020), and references therein. Adapted and modified from Peucker-Ehrenbrink and Ravizza (2020). (B) Marine  $^{187}\text{Os}/^{188}\text{Os}$  record for the Cretaceous, Jurassic, and Late Triassic. For data sources, see Peucker-Ehrenbrink and Ravizza (2012), and references therein. From Peucker-Ehrenbrink and Ravizza (2012). In both (A) and (B), red vertical lines indicate well-dated impact events.

Both the K-Pg boundary and the Late Eocene impact events show a characteristic shape of near instantaneous shift to unradiogenic values followed by an exponential return to more radiogenic values (Fig. 1.12A). This, in principle, allows the probing the sedimental record for other, yet undetected impact events (e.g., Peucker-Ehrenbrink and Ravizza 2012). As the

marine Os isotope data basis for the Neoproterozoic (and earlier eons) is comparably poor (and non-existent in some cases), BIF analyses provide an additional tool to search for similar effects in the Os isotope evolution curve through deep time. This approach might be promising also in light of the higher impact flux onto the early Earth (e.g., Koeberl 2006). Besides the geochronological approach (i.e., age dating) as outlined in this chapter (Goal of this study), it is, therefore, intended to screen the data presented in this study for the ~ 590 Ma old Urucum BIF for possible impact signatures.

While the Cenozoic record of  $^{187}\text{Os}/^{188}\text{Os}$  in seawater is relatively robust, efforts to reconstruct the Os isotopic seawater curve further back in time faces additional challenges. As the age of a sample increases, so does the potential of a secondary diagenetic and metamorphic overprint, compromising the primary nature of the Os budget of samples. Compared to the Cenozoic, the Mesozoic Os isotope record is poorly established, because data sets in are few and mostly solitary, focusing on oceanic anoxic events (OAE) (Fig. 1.12B) or era boundaries. For example, just before the onset of OAE 2 (~94 Ma), there is a sharp drop in  $^{187}\text{Os}/^{188}\text{Os}$  ratios (from 0.6 to 0.16, e.g., Turgeon and Creaser 2008) followed by a prolonged duration of unradiogenic  $^{187}\text{Os}/^{188}\text{Os}$  values. Similar shifts have been observed during OAE1s (e.g., Tejada et al. 2009). Xu et al. (2009) yielded two isochrones with initial  $^{187}\text{Os}/^{188}\text{Os}$  values of 0.67 and 0.83 for the Anisian-Ladinian boundary within the Triassic. These studies show that the dynamic range of  $^{187}\text{Os}/^{188}\text{Os}$  in seawater during the Mesozoic, however additional work is needed, especially to assess potential regional variations (see Peucker-Ehrenbrink and Ravizza 2012 for a detailed discussion).

Pre-Phanerozoic records are even more scarce compared to the Mesozoic (Fig. 1.13). The available data suggest significant changes over the past 2.7 Gy (e.g., Lu et al. 2017). Despite large uncertainties, the Precambrian Os records display two major features that are considered robust (e.g., van Acken et al 2013; Sperling et al. 2014; Tripathy and Singh 2015). However, the datasets available are sparse and almost exclusively rely on data from organic-rich mudrocks (ORM). One should, therefore, use caution in interpreting these datasets. The first major feature are initial  $^{187}\text{Os}/^{188}\text{Os}$  ratios that are practically indistinguishable from the Os mantle evolution curve (provided uncertainties are considered; e.g., Kendall et al. 2014). Positive deviations from the mantle evolution curve have been attributed to oxidative weathering of crustal sulphide minerals with high Re/Os (e.g., Sekine et al. 2011; Kendall et al. 2015). On the other hand, initial  $^{187}\text{Os}/^{188}\text{Os}$  ratios that are indistinguishable from a chondritic mantle evolution curve are attributed to low atmospheric  $\text{O}_2$  levels (e.g., Hannah et al. 2004).

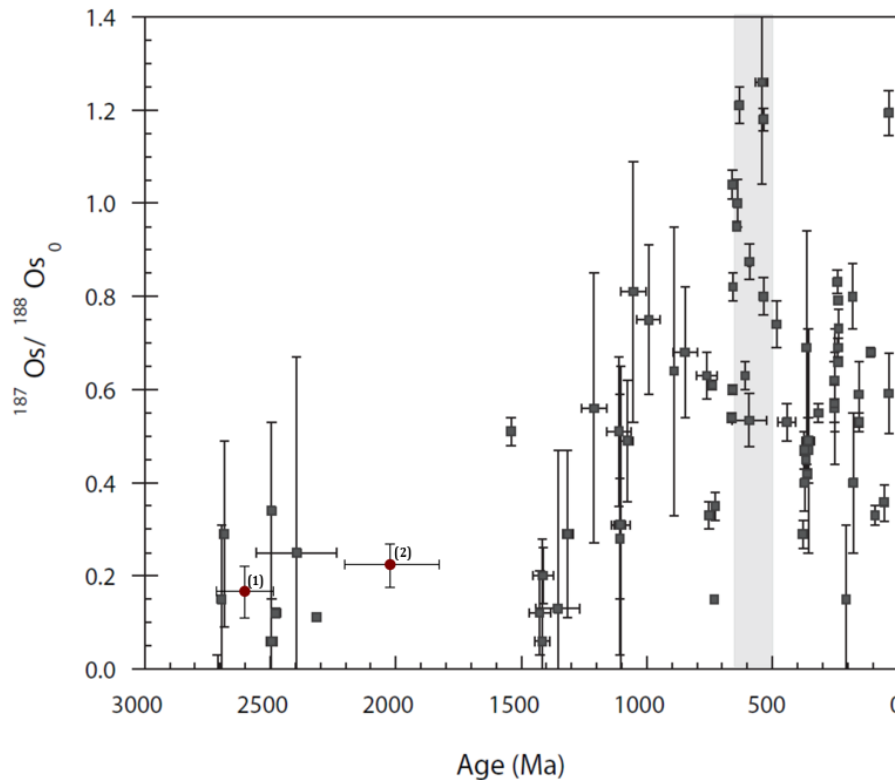


**Figure 1.13:** Initial  $^{187}\text{Os}/^{188}\text{Os}$  data and Re-Os isochron ages of published ORM (see Peucker-Ehrenbrink and Ravizza 2020, for data sources). Additionally, initial  $^{187}\text{Os}/^{188}\text{Os}$  data of (1) the ~2.7 Gy old Temagami BIF (Schulz et al. 2021), and (2) the 2.2 to 1.8 Gy old Biwabik BIF (Ripley et al. 2008) were added to the graph as red dots. The shaded bar highlights an apparent interval of high initial  $^{187}\text{Os}/^{188}\text{Os}$  ratios in the Ediacaran to Cambrian period. Note that the under sampling of pre-Cenozoic  $^{187}\text{Os}/^{188}\text{Os}$  variations makes statements about long term trends difficult. Adapted and modified from Peucker-Ehrenbrink and Ravizza (2020).

The second prominent feature in the Precambrian Os record is an interval of high  $^{187}\text{Os}/^{188}\text{Os}$  ratios (up to 1.2 to 1.4) in the late Neoproterozoic that lasts into the Cambrian (Fig. 1.13). During this interval, initial  $^{187}\text{Os}/^{188}\text{Os}$  ratios of organic rich mudrocks can reach up to 1.44, exceeding that of modern-day seawater (e.g., van Acken et al. 2013). The cause of this prominent shift in is still debated, but several hypotheses have been proposed, all of them arguing for enhanced weathering of old crustal rocks as source of radiogenic Os (e.g., Lyons et al. 2014, Rooney et al 2014, Tripathy and Singh 2015). While evolved continental crust was emerged and available for erosion and terrestrial weathering since the Neoproterozoic, if not longer (e.g., Viehmann et al. 2014, 2018), the dataset is sparse and the potential influence of those continental masses on the seawater chemistry requires further investigation. Several authors present Paleoproterozoic (e.g., Sekine et al. 2011) and Neoproterozoic (e.g., Rooney et al. 2015; Peucker-Ehrenbrink et al. 2016) sediment samples dominated by water-derived (hydrogenous) Os. In both time periods, temporal excursions to high  $^{187}\text{Os}/^{188}\text{Os}$  ratios from much lower ratios (from ~0.4 to ~1.2 and from ~0.5 to ~1.0, respectively) during deglaciation were observed. Recently, Schulz et al. (2021) reported Os isotope data combined with HSE data in alternating layers of the ~2.9 Gy old Temagami BIF, Ontario. These authors reported a  $^{187}\text{Os}/^{188}\text{Os}$  seawater ratio of 0.11 to 0.22. Global correlation on the existing available data

is difficult and controversially discussed, but they provide a basis for further hypothesis testing and higher resolution work.

To summarize, the Cenozoic  $^{187}\text{Os}/^{188}\text{Os}$  seawater isotope record shows a dynamic nature and is a useful tool that allows the observation of short-term events and fluctuations (i.e., impact events). However, reconstruction of the isotope record becomes more challenging for geologically older time periods. The Mesozoic  $^{187}\text{Os}/^{188}\text{Os}$  seawater isotope record is poorly established and primarily focused on OAEs and era boundaries. Available data shows that the marine Os isotope record of the Mesozoic is comparable to the Cenozoic. The reconstruction of the pre-Phanerozoic marine Os isotope record is still in its infancy and has only a handful of datasets. The available data indicate that the seawater was dominated by mantle-derived/hydrothermal vent sources. A prominent excursion to radiogenic values is first seen in the Neoproterozoic; however, the cause of this shift is still debated.

## 2 Geological setting of the Urucum Iron Formation

### 2.1 The South American Platform

The Geology of the South American Continent is dominated by four major lithotectonic domains: the South American Platform, the Andean Mountain Belt, the Patagonian Massif to the west, and the Atlantic oceanic crust to the east (Fig. 2.1). The South American platform makes up the interior of the continent and is mainly composed of Precambrian metamorphic and igneous complexes. Archean terranes have been largely preserved (35%), while accreted juvenile crust of Paleoproterozoic age (mainly 2.2 – 1.9 Gy) make up the majority of the Platform (54%). Meso- to Neoproterozoic material (10%) and a small amount of Phanerozoic rocks (1%) complete the platform (e.g., Sato and Siga Jr. 2000; Teixeira et al. 2007). These cratonic complexes and nuclei agglutinated over the course of several Archean, Proterozoic, and Early Paleozoic orogenic cycles, the most notable the Brasiliano/Pan-African orogeny (600 – 500 Ma) (e.g., Trompette et al. 1994), and the closure of several ocean basins into the South American Platform, remaining a part of the supercontinent Gondwana until the opening of the South Atlantic in the Mesozoic (e.g., Engler 2011).

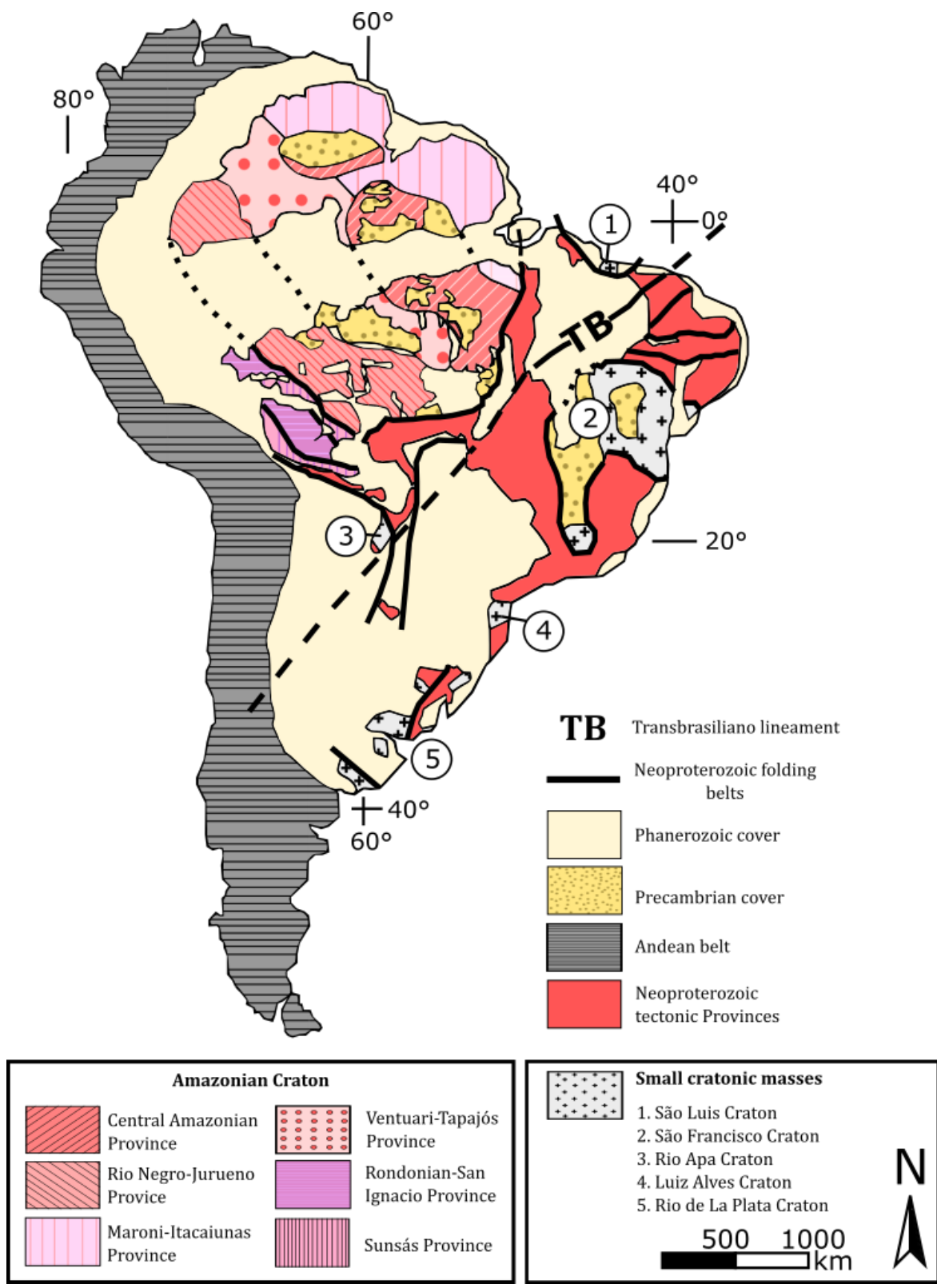


**Figure 2.1:** Geotectonic provinces of South America and the major provinces of the Amazonian Craton. Modified after Engler (2011) and Cordani et al. (2000).

Archean and Proterozoic provinces are mainly exposed in three shield areas that are surrounded by Neoproterozoic fold belts. Some of these provinces are briefly discussed below.

## **The Amazonian Craton**

With a size of around 4.4 million km<sup>2</sup> the Amazonian Craton is one of the largest cratonic areas of the world. It makes up much of the continental interior of the northern South American Continent and includes parts of Brazil, French Guiana, Guyana Suriname, Venezuela, Colombia, and Bolivia. The cratonic area is overlain by the sub-Andean basin to the west and constrained to the east and south by the Neoproterozoic Paraguay, Araguaia and Tucavaca folding belts. Via the Paleozoic Solimões-Amazonas basin the larger Craton area is divided into a northern and southern Precambrian shield (the Guaporé shield and the Guiana shield respectively), which have been stable since 1.0 Gy (e.g., Engler 2011). Geochronologically, the Amazonian Craton can be divided into six major provinces: The Archean Central Amazonian Province (> 2.3 Ga), the 2.24 – 1.95 Gy old Maroni-Itacaiúnas Province, the Ventuari-Tapajós Province (1.95 – 1.8 Ga), the Rio Negro-Juruena Province (1.8 – 1.55 Ga), the 1.55 – 1.30 Gy old Rondonian-San Ignácio Province, and the marginal rock of the Sunsás Province (1.25 – 1.0 Ga) (e.g., Cordani et al. 2009; Tassinari et al. 2000). The western part of the Amazonian Craton is significantly affected by younger metamorphic and magmatic overprint, while the eastern part is affected to a lesser extent. The Archean predecessor of the Amazonian Craton was most likely composed of independent microcontinents that amalgamated between 2.2 and 1.95 Ga and developed the Paleoproterozoic orogenic belts. Development of magmatic arcs between 1.95 – 1.45 Gy allowed accretion of juvenile continental crust (Ventuari-Tapajós, Rio Negro-Juruena, and parts of the Rondonian-San Ignácio Province) on the western margin of the continent. The cause of these arcs remains a matter of debate, one possibility could be the subduction of oceanic lithosphere due to the collision of the Amazonian provinces with another continental mass (e.g., Cordani et al. 2009). The final orogenic evolution of the Amazonian Craton took place between 1.4 – 1.0 Gy, as the Amazonian Craton collided with Laurentia to form the supercontinent Rodinia (e.g., Engler 2011).

## **The São Francisco Craton**

Located in the central-eastern part of Brazil, the São Francisco Craton is one of South America's major shield areas. It is considered the northwestern extension of the Congo-Zaire Craton of Central Africa and is surrounded by folding belts of the Brasiliano/Pan-African orogeny. Archean and Paleoproterozoic basement rocks are exposed in the N-NE (Bahia) and the southern part of the craton (Minas Gerais), the central part is dominated by basement rocks that were tectonically reworked between 1.8 Gy and 1.2 Gy. An N-S elongated rift-thrust belt developed during that period, allowing the deposition of the Paleo to Mesoproterozoic Espinhaço Supergroup in its grabens and basins (e.g., Heilbron et al. 2017). The ~ 1.75 Ga Paramirin polyphase province can be distinguished along an NNW-SSE axis of the craton,

whose gneissic rocks and supracrustal sequences experienced reworking and isotopic resetting during the Brasiliano cycle (e.g., Alkmim and Marins-Neto 2012). The largest part of the cratonic crystalline basement is covered by sediments of Neoproterozoic and Phanerozoic age (e.g., Heilbron et al. 2017).

### **The Rio Apa Craton**

With a size of 13,200 km<sup>2</sup> the Rio Apa Craton is a one of the smallest cratonic fragments that make up the Precambrian terranes of South America and is therefore seldom mentioned. However, due to its proximity and significance for the Corumbá area it shall be briefly discussed. The cratonic masses of the Rio Apa block crop out in southern Brazil (State of Mato Grosso del Sul) and northeastern Paraguay. It is bound eastward by the southern Paraguay belt, a Neoproterozoic folding belt, and is considered part of its cratonic domain (e.g., Cordani et al. 2010). The central part of the region hosts the oldest basement rocks comprised of medium- to high-grade metamorphic granites, banded gneisses and migmatites (Morraria and Porto Murtinho basement), and homogeneous orthogneisses (Caracol leucocratic gneisses) of Precambrian age (1.95 – 1.72 Ga) (e.g., Lacerda-Filho et al. 2006; Araújo et al. 1982). These basement rocks are intruded by the felsic magmatic rocks of the Alumiador batholith, a large elongated, NNE trending intrusion (e.g., Lacerda-Filho et al. 2006; Cordani et al. 2010). A second large portion of the suite forms an NW trending extension to the North and is surrounded and intruded by a gabbro-anorthositic suite (Serra da Alegria) (e.g., Lacerda-Filho et al. 2006). The northern parts of the Craton are comprised of the supracrustal, low- to medium-grade metavolcano-sedimentary rocks of the Alto Terrorê association (e.g., Godoi et al. 2001). Metabasic rocks occur scattered in many locations, in the northeastern part, near the town of Baía das Carças, the association is intruded by three small, slightly foliated granitic massifs. In the southern parts several outcrops of low- to medium-grade metamorphic sequences were combined under the informal name of “Amolar Domain” (e.g., Lacerda-Filho et al. 2006), comprised of supracrustal and meta-volcanic rocks intruded by small granitoid plutons. They are correlative with the Sunsás orogeny of the Amazonian craton (1.10 – 1.00 Ga) and, therefore, late Mesoproterozoic in age (e.g., Cordani et al. 2010).

Large areas of the Rio Apa basements are covered by recent (Pantanal Formation) or Paleozoic (Aquidauana Formation) sediments. In the eastern, along the Serra de Bodoquena, and the southernmost part of the craton, the intercratonic cover of the Neoproterozoic Corumbá Group overlies the basement. It shows an increase in metamorphism and tectonics towards the East, where the low-grade metasedimentary rocks of the Paraguay belt crop out in the easternmost part. According to Cordani et al. (2010), all pre-Neoproterozoic basement rocks are related to a series of magmatic arc complexes, originating from different sources in different times. Based on Sm-Nd model ages they divided the Rio Apa Craton into an eastern and

western distinct tectonic block, separated by a roughly meridian boundary, most likely a major fault zone. The Craton itself correlates well with the SW corner of the Amazonian Craton and was probably attached to it during Proterozoic times.

## 2.2 The Santa Cruz Deposit

### 2.2.1 Geological Overview

Located in the humid Pantanal floodplains, the Corumbá area is situated in the Tocantins Province, a large collisional province derived through tectonic interaction between the Amazonian, Rio Apa and São Francisco paleo-continentes during the Brasiliano orogeny (Fig. 2.2A-B; e.g., Trompette et al. 1994). The area is enclosed by a series of folding belts: the larger Araguaia and Brasília belts, the NNE stretching northern Paraguay belt, the SSE stretching southern Paraguay belt and the WNW stretching Chiquito-Tucavaca aulacogen. The Brasília belt is commonly divided into three major domains (the Goiás Magmatic Arc, the Internal Zone and the External Zone), aligning parallel to the São Francisco margin (e.g., Fuck et al. 2006) and is comprised of oceanic island rocks, back-arc basin sediments, supra-crustal rocks and crystalline basement in sub-greenschist to (amphibolite-) greenschist facies (e.g., Cordeiro et al. 2014, D'el-Rey Silva et al. 2016). The lithostratigraphic model of the Paraguay belt can be divided into three structural domains, parallel to the Amazonian margin, and resembles an eastward deepening basin (e.g., Alvarenga and Trompette 1993; Alvarenga et al. 2011). The Maronian diamictites of the Puga Formation compromise the westernmost glaciomarine environment and unconformably overly the crystalline basement. Eastwards the Puga Formation gradually passes into the Cuiabá Group (diamictite, quartzite and phyllite), illustrating a continental slope deposition environment with a glacial diamictite-turbidite sedimentation on the eastern outer slope. In the Corumbá area, basal diamictites equivalent to the Puga Fm. can be found in the Jacadigo and the Boqui Groups, Araras lithotypes in the southern Paraguay belt and the Tucavaca aulocogen constitute the Corumbá Group (e.g., Trompette et al. 1994).

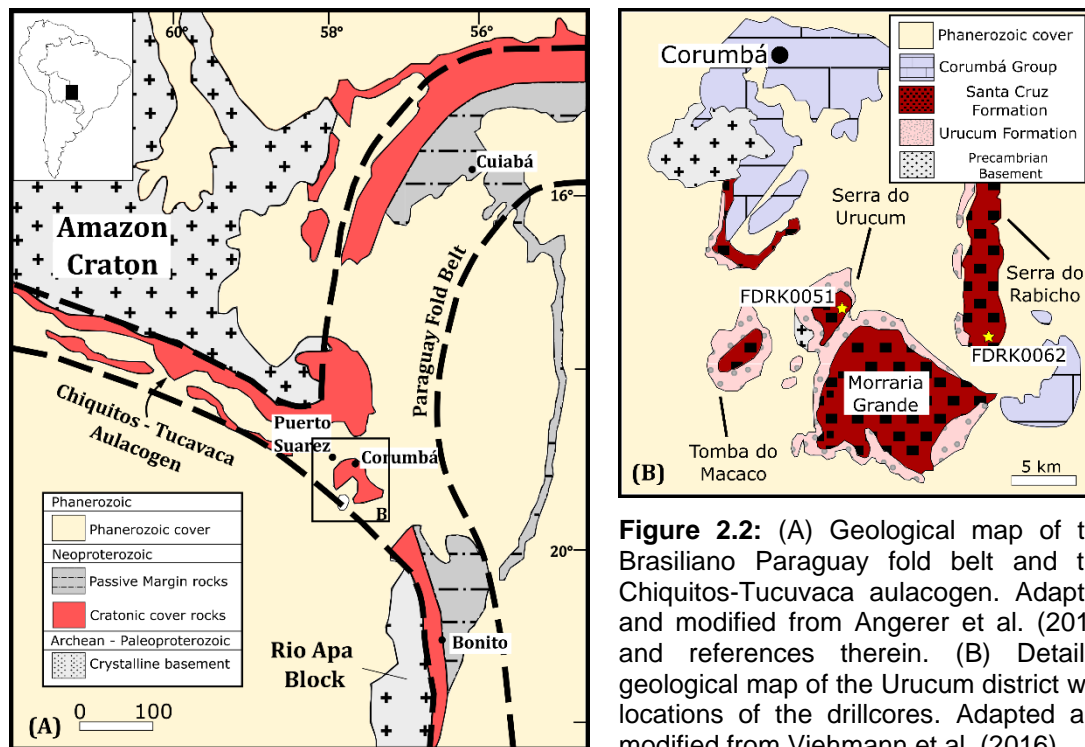


**Figure 2.2:** (A) Geological map of the Brasiliano Paraguay fold belt and the Chiquitos-Tucavaca aulacogen. Adapted and modified from Angerer et al. (2016) and references therein. (B) Detailed geological map of the Urucum district with locations of the drillcores. Adapted and modified from Viehmann et al. (2016).

The series of folding belts have their origin in the closing of the Goiás, (e.g., Pimentel et al. 2004) or Clymene Ocean (e.g., Casquet et al. 2012). Starting at ca. 630 Ma, several collision events between Amazonia and marginal cratons (São Francisco, Paraná) finalised the assemblage of Gondwana, indicated by the NE-SW Transbrasiliano shear zone (e.g., Cordani et al. 2013). Collision of Amazonia and São Francisco from 650 – 580 Ma built up the Aaguaia belt and Brasilia belt. Simultaneous subduction of the eastern margin of the Paraná block under the São Francisco craton imprinted late crustal NE-SW shortening (see Tectonics) through the whole southern segment of the Brasilia belt (e.g., D’el-Rey Silva et al 2011, 2016).

Subsequent soft collision events between the Paraná block and the Amazonia-Rio Apa craton in 540-513 Ma formed the Paraguay belt, making it one of the youngest Gondwana-forming orogens (e.g., Geraldés et al. 2008; Tohver et al. 2010). Synchronously extensional tectonics along the southern margin of the Amazonian Craton generated a system of small rifts parallel to the borders of the craton (e.g., Trompette et al. 1994), finalising the R-R-R triple junction structural domain of the Northern and southern Paraguai Belt and the the Chiquitos–Tucavaca aulacogen. These rifts separated into isolated basins, forming the Corumba graben system (e.g., Freitas et al. 2011; Walde and Hagemann 2007).

## 2.2.2 Age and Stratigraphy

Neoproterozoic sediments in the Urucum district crop out as a dome-like structures of several inselbergs within the WNW-ESE striking Chiquito-Tucavaca aulacogen, divided by steeply dipping faults (e.g., Walde and Hagemann 2007; Piacentini et al. 2013; Viehmann et al. 2016). The domes are oriented along the major deformation faults and small-scale deformation faults, the long axis being NE-SW oriented (e.g., Freitas et al. 2011). They overlie the crystalline basement, which consists of intensively folded metamorphic rocks composed out of various types of gneisses, schists, amphibolites and quartzites (e.g., de Almedia 1945, Dorr II 1945), which are intruded by granites and pegmatites with ages between 1200 Ma (e.g., Walde 1981) and 822 Ma (e.g., Hasui and de Almeida 1970), as well as younger, basic dikes.

Two lithostratigraphic groups can be distinguished: the Jacadigo Group; hosting the IF; and the Corumba Group. According to Dorr II (1945), the Jacadigo Group consists of the Urucum, the Córrego das Pedas and the Banda Alta Formation. Because the rocks of the Córrego das Pedas and the Banda Alt Fm. are closely related in genesis, alternative lithostratigraphies often group these Formations together in the Lower and Upper Santa Cruz Formation (e.g., de Almeida 1945). The Corumbá Group is comprised of five formations, but only three are present in the Corumbá area (e.g., D'el-Rey Silva et al. 2016). They are the Bociana Formation (conglomerate, rudstone and sandstone capped by dolomite/dolostone), the Tamengo Formation (limestone intercalated with marl, siltite and volcanic ash), and the Guiacurus Formation (siltite and pelite) (Fig. 2.3).

Depositional age of the Santa Cruz deposits is poorly constrained.  $^{40}\text{K}/^{40}\text{Ar}$  ages of basement granites have provided a maximum age of ca.  $889 \pm 44$  Ma for overlying sedimentary rocks (Hasui and de Almeida 1970). From the La Pimienta Fm. in Bolivia, a lower part of the Boqui Group, a  $^{40}\text{K}/^{40}\text{Ar}$  maximum age of  $635 \pm 15$  Ma of plutonic rocks has been reported (O'Connor and Walde 1985). Piacentini et al. (2013) reported  $^{40}\text{Ar}/^{39}\text{Ar}$  ages of  $587 \pm 7$  Ma and  $547 \pm 3$  Ma for Mn-horizon1-minerals cryptomelane (diagenetic age) and braunite (re-crystallization age), respectively. They concluded that the deposition age must be older than 590 Ma, interpreting the age of cryptomelane as the age of early diagenesis, as cryptomelane experienced Ar-loss via thermally induced diffusion. Viehmann et al. (2016) reports a Sm-Nd age of  $566 \pm 110$  Ma for pristine Urucum IF samples (the same sample set used in this thesis), relating the deposition of the Urucum IF to the Gaskiers glaciation.

In the Puga Formation, Southern Paraguay belt, U-Pb ages yielded a maximum deposition age of 709 Ma for detrital zircon in glaciogenic diamictites (e.g., Babinski 2013). Minimum deposition age is constrained by the presence of *Cloudina lucianoii* and *Corumbella weneri*, Ediacaran index fossils, in the Corumba Group (e.g., Walde et al. 1982, 2017; Gaucher et al. 2003). Additionally, U-Pb dating of zircons from volcanic ash layers within the Tamengo Formation yielded an age of  $543 \pm 3$  Ma (e.g., Babinski et al. 2008; Boggiani et al. 2010) and CA-ID-TIMS of tuff layers yielded an age from 541.85 to 542.37 Ma (Parry et al. 2017). These

constrains suggest deposition of the IF-Mn-F deposits during the offset of the Cryogenian and relate it to the Brasiliano collision around 590 Ma and the Gaskiers glaciation (~ 585 - 582 Ma). Nonetheless, a relation to the Marinoan glaciation (~ 660-635 Ma) cannot be excluded (e.g., Piacentini et al. 2013; Trompette et al. 1998; Angerer et al. 2016; Viehmann et al. 2016). Recently, Biondi and Lopez (2017) proposed a synchronous deposition of the Santa Cruz formation in the basin and the Tamengo and Bocaina Formation in the shallow marginal regions, making the Santa Cruz IF-Mn-F deposits not older than 550 Ma.

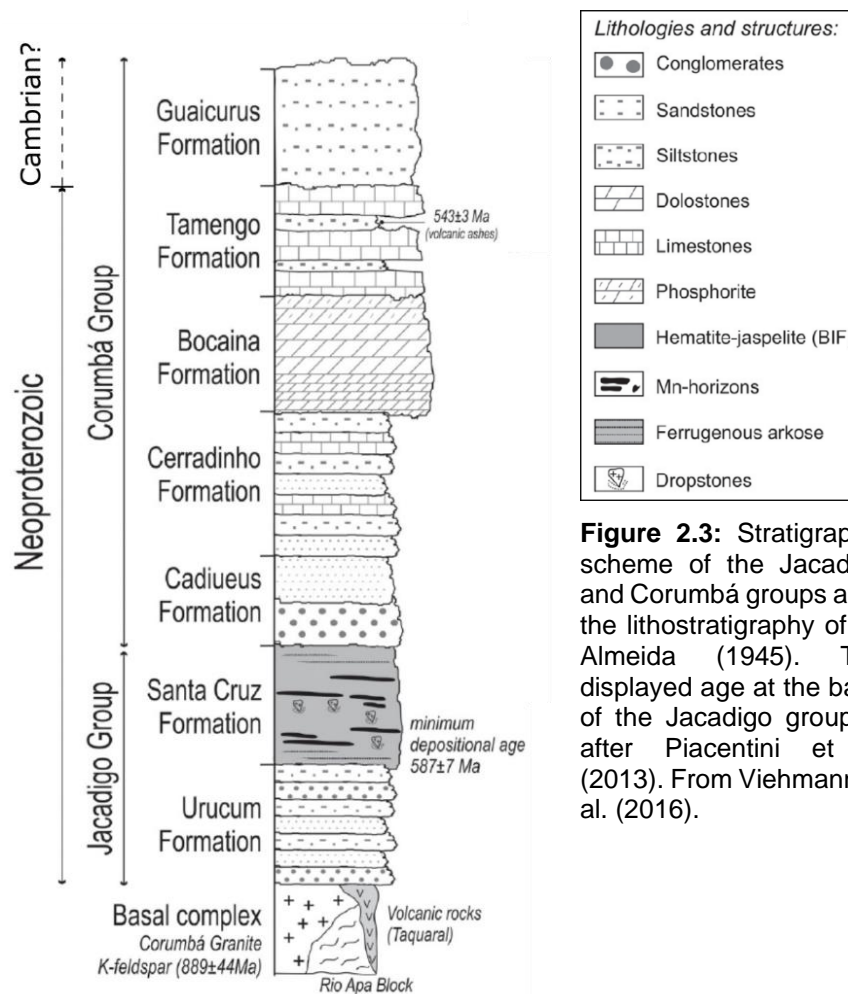


**Figure 2.3:** Stratigraphic scheme of the Jacadigo and Corumbá groups after the lithostratigraphy of de Almeida (1945). The displayed age at the base of the Jacadigo group is after Piacentini et al (2013). From Viehmann et al. (2016).

### The Urucum Formation

The base of the Jacadigo Group consists of the Urucum Formation, which lies above the crystalline basement of the Rio-Apa block with an angular unconformity (e.g., Dorr II 1945; de Almeida 1946). Its thickness ranges from 300m to 500 m and is composed mainly of massive, coarse to medium-coarse arkoses, sandstones, conglomerates and subordinated mudstones and carbonates. The arkose consists of calcite, quartz, feldspar, and a few accessory minerals. The feldspar makes up around 20% and is made up of crushed and sericitized, sodic plagioclase, which is dominant in the lower part, while in the upper part microcline is more abundant (e.g., Dorr II 1945; Urban et al. 1992; Freitas et al. 2011). Quartz grains in the arkose

are typically highly angular, showing no evidence of long transportation. The most abundant type of conglomerate in the Urucum Formation is composed of well-rounded pebbles, mainly of granite, but also includes limestones, gneisses, and schists of various compositions (e.g., Dorr II 1945). In the uppermost section of the Urucum formation and some conglomerates are defined by sparsely scattered pebbles or boulders in a moderately well sorted, clastic matrix, the texture similar to coarse sandstone. The rocks are generally cemented by carbonates and locally display cross-bedding and inverse grading (e.g., Dorr II 1945; Urban et al. 1992; Klein et al. 2004). The characteristics and features of the Urucum Formation represent an alluvial to lacustrine facies during rift initiation and early climax of the Corumba graben system. Spatial distribution suggests deposition in small, isolated graben which evolved to a wide, continuous fault-bounded graben, bordering alluvial fans and a bedload-dominated river system (e.g., Freitas et al. 2011).

### **The Córrego das Pedas Formation**

Conformably overlying the Urucum Fm are the siliciclastic deposits of the transitional Córrego das Pedas Formation, which predominantly consist of Fe- and Mn-rich sandstones, arcose and micro-conglomerates mixed with Granular Iron Formation. Composition is highly variable both vertically and laterally, and the upper and lower contacts of the formation are gradational, making its location arbitrary. Still, the base of the formation is generally considered to be defined by the extensively mined manganese horizon Mn1 of varying thickness (0 -7m), and glacial dropstones of granitic composition (e.g., Urban et al. 1992). Going upwards the rocks grade regularly from ferruginous arcose to hematitic jasper, with clastic quartz scattered around in the middle of the formation. Hematite is present in all rocks and can make up to 70 vol% of some beds, but generally a proportion < 50 vol% is common, with some beds going as low as < 30 vol%. Carbon is considered absent in the whole formation, but tiny rhombs of supposedly dolomite can be found in a few horizons in the middle and top of the formation (e.g., Dorr II 1945; Urban et al. 1992). As mentioned, the genesis of Córrego das Pedas Formation is closely related to the IF-Mn-F deposits of the Banda Alta Formation. Deposition most likely took place under marine to closed-basin conditions, with the environment shifting during deposition, indicated by aeolian and fluvial crossbedding at the base (e.g., Dorr II 1945).

### **The Banda Alta Formation**

Overlying the Córrego das Pedas Fm. are the ferruginous rocks of the Banda Alta Formation. They reach a maximum thickness of around 300 m and are defined by series of massive beds of banded hematitic jasper with an average thickness of 1.5 m (e.g., Dorr II 1945; Hoppe et al. 1987; Urban et al. 1992). Based on composition, a lower and upper carbonaceous zone, as well as an intermediate siliceous zone, can be distinguished. The beds in the carbonaceous

zones are composed of dolomite, jasper and hematite, while in the intermediate zone hematite and jaspilitic chert are more dominant. Generally, the BIF is defined by alternating beds of ferruginous minerals and silica that show fine lamination in the mm to  $\mu\text{m}$  range. The lamination is caused by variations of grain size, and, to a minor extent, by extremely fine fragments of angular detrital quartz along the bedding planes (e.g., Angerer et al. 2016). Three manganese oxide horizons, Mn<sub>2</sub>, Mn<sub>3</sub> and Mn<sub>4</sub> are present, having a thickness of up to 3m, decreasing upwards in thickness. They are all uniform in appearance and do not differ significantly in composition (e.g., Dorr II 1945; Urban et al. 1992; Frei et al. 2017). Major constituent of all manganese horizons is cryptomelane with hematite being the second most abundant mineral (e.g., Piacentini et al. 2013). Obscure bedding can be observed in fresh outcrops but is more likely bulky lamination rather than true bedding. On weathered outcrops, especially in the lower horizons, differential solubility has produced apparent bedding (e.g., Dorr II 1945). In the upper third of the formation clastic beds of siltstone, jasper, conglomerate, sandstone and conglomerated unbanded hematite of lenticular shape are common. Granitic dropstones with a size of up to 3m and channel fillings can be found sporadically throughout the whole Formation.

The IF and Mn-F of the Banda Alta Formation have low Al<sub>2</sub>O<sub>3</sub>, CaO and K<sub>2</sub>O concentrations, making them extremely pure (e.g., Frei et al. 2017). Average iron-oxide content is 66-68%, making the Banda Alta Fm. one of the highest-grade iron formations in the world (e.g., Dorr II 1973).

### 2.2.3 Deposition and Tectonics

In this thesis, I follow the genetic model of deposition of the Urucum BIF in a glaciogenic environment, which has been favored early on (e.g., Schneider 1984; Schreck 1984; Walde 1988; Urban et al. 1992) and since been further supported by geochemical, mineral chemical, and isotopic studies (e.g., Angerer et al. 2016; Viehmann et al. 2016; Frei et al. 2017, de Souza et al. 2019). Alternative models, which argue against glacial influence (e.g., Freitas et al. 2011), have also been proposed (see Walde and Hagemann 2007 for a detailed review).

After the glaciogenic model, the Urucum IF-Mn-F were deposited in a narrow and long graben system, or basin, which was filled with clastic sediments from riverine systems, providing a benthic source of iron and manganese, as well as experiencing faulting and volcanism associated with rifting, causing hydrothermal activity (e.g., Huang et al. 2021) During glaciation, the Urucum basin was closed-off from the atmosphere due to the presence glacial and sea ice, prevention O<sub>2</sub> ventilation and allowing the build-up of anoxic deep water. Upwelling currents transported low-temperature hydrothermal fluids and benthic flux, generated by bacterial reduction in the sediment, into the basin, providing a continuous supply of metals that remain in solution. During interglacials, the icesheets retreated, allowing

exchange between atmosphere, open seawater and the Urucum basin water, and generating a redoxcline between oxidized shallow water and anoxic deep water. As the metal bearing fluid was transported across the redoxcline, it was oxidized and precipitation of hydroxides, rich in Fe or Si as well as calcium carbonates, took place (e.g., Angerer et al. 2016). Deposition most likely occurred at the water-sediment interface in shallow environment, below the storm wave base, indicated by plane-parallel bedding and recurring peloid-rich beds (e.g., de Souza et al. 2019). Mn-rich chemical sediments were deposited simultaneously in shallower, more-oxidized environments with an enhanced influx of terrigenous material. The deposition was most likely dependent on the glacial-interglacial cycle, deposition primary ferrihydrite and manganese-rich sediments during interglacial periods, when the ice retreated, and seizing during glacial periods, when glacial ice advanced into the basin, cutting off the atmospheric and hydrospheric oxygen supply.

Following their deposition, the rocks of the Corumba graben system underwent progressive deformation and low-grade metamorphism (sub-greenschist) during the Brasiliano Cycle. D'el-Rey Silva et al. (2016) divided tectonic structures into three main phases: D1-D2-D3. Phase D1 displays pervasive foliation (sub-)parallel to bedding and rare intrafolial folds. These features are abundant in the Jacadigo Group and quite penetrative in the BIF deposits, consisting of fine mineral foliation of fine plates of hematite, displaying evidence for intense intra-stratal, layer-parallel ductile flow. S1-foliation has been interpreted as a record of the low-grade sub-greenschist metamorphism.

Phase D2 led to low angle frontal ramps and a reverse-sense kinematics with relative movement of the top to NW. Ductile regional flow in the SE-NW direction resulted in folds, axial planar foliation and thrust faults, deforming the bedding and D1 structures. F2 faults are extremely common, highly asymmetric, tight-isoclinal and moderately to gently inclined. S2 foliation is represented by a slaty cleavage in fine-grained siliciclastic rocks and hematite-rich layers, dipping at a low angle either to NW or SE. Evidence suggests that the D2 and D1 ductile flows were co-axial.

The last major phase of deformation, D3, is represented via crustal shortening D3p and D3t, which deform the bedding as well as D1 and D2 structures. Both shortenings show similar features (folds and planar foliation) and morphological characteristics but differ in their orientation. D3p, represented by up-right folds and strong axial planar foliations, indicates crustal shortening in the NW-SE direction. D3t structures on the other hand, while similar in morphology, indicate shortening in the NE – SW direction. Abundant field evidence suggests that the D3t deformation was superimposed on D3p structures, ending earlier than the D3p shortening. The crystalline basement was involved in all three major deformation phases, being shortened due to sub-horizontal stresses during D2-D3p deformation, which also inverted the normal faults of the Jacadigo Group.

### 2.3 Previous research on the Urucum iron formation

Ferruginous rocks in the Urucum district were discovered as early as 1894 (Evans 1894), but it took until the middle of the last century for the first comprehensive ore deposit model to appear (e.g., Dorr II 1945; de Almedia 1945). Based on field studies Dorr II (1945) proposed an epicontinental or marine basin in which Mn minerals accumulated due to weathering on the Amazonian Craton. Marine sediments as source of the Fe and Mn deposits were proposed by de Almeida (1946), Putzer (1958), and Haralyi (1972), largely adhering to Dorr's deposition model. The sharp contrast between Mn lenses and iron ore was attributed to changes in physico-chemical conditions (e.g., Putzer 1958).

In the 1980's alternative models began to emerge. Based on the occurrence of hydrothermal leached volcanic rocks several authors, most prominently Detlef H.G. Walde, suggested a partial volcanic origin for the Urucum deposit (e.g., Walde 1981; Walde et al. 1981; Leonardos and Walde 1982). This outlook was further supported by deposits of the La Pimienta Formation (Bolivia), consisting of volcanic-clastic rocks at the base of the Jacadigo Group (e.g., O'Connor and Walde 1985). A detailed study of the mineralogy and formation of the Urucum deposits and a geochemical classification and petrogenesis of manganese ore were published by Schneider (1984) and Schreck (1984), respectively, and later summarized by Urban et al. (1992), who proposed a comprehensive ore model. The genesis of the deposits was divided into a synsedimentary stage, followed by supergene enrichment. The synsedimentary stage was characterized by anoxic conditions in a partially ice-covered graben-system. During retrogression of the ice,  $Mn^{2+}$  and, to a lesser extent,  $Fe^{2+}$  ions were mobilized out of clastic material brought by glacial erosion and transported seawards in solution, where increasing oxidizing conditions in the graben-system lead to the precipitation of  $Mn^{4+}$  and  $Fe^{3+}$ , forming the distinct Mn horizons. Afterwards supergene enrichment took place during weathering, further enriching the ore minerals.

A sedimentary genetic model similar to Urban's model was proposed by van Leeuwen and Graf (1987) and Graf et al. (1994). Deposition was interpreted as to have happened in interconnected continental or epicontinental basins under an extensive ice cover. This ice cover led to an anoxic environment in the basins, Fe and Mn were derived from weathering of terrestrial rocks. Due to the early recognition of dropstones in the IF and diamictites in the stratigraphic succession, all models favoured deposition in a glaciogenic environment.

New understandings in the regional geological setting resulted in a new geological model by Haralyi and Walde (1986) and Walde (1988), who first proposed the existence of an extensional structure in the Urucum area: the Corumbá graben system. This new tectonic

model was used by Trompette et al. (1998) to propose a hydrothermal origin for the Urucum deposits. Leaching of a hidden mafic intrusion associated with the graben structure led to the formation of the deposits. Trompette et al. (1998) based his model not only on the graben system and associated fault zones but also on the occurrence of braunite (indicative for elevated P-T conditions), the existence of quartz-tourmaline veins cross-cutting the Jacadigo Group in the Urucum area (Dorr II 1945) and hydrothermal magnetite occurring in graben-related fault zones.

Based on limited REE and carbon isotope data on precursor ore samples Klein and Ladeira (2004) concluded that the Fe, Mn, and Si was sourced from ocean water with a limited hydrothermal component, indicated by the lack of a positive Eu anomaly and similarities to deep ocean waters in the REE patterns. Costa et al. (2005) used whole rock, trace element and REE data of manganese ore samples to interpret the deposition of the Mn ore and BIF in a marine environment, following the proposition of Graf et al. (1994). Walde and Hagemann (2007) further reinterpreted the geological setting for the Urucum deposit, arguing for a large graben structure with associated fault zones. Based on their observations they argued on favour of an influence of hypogene hydrothermal activity during the time of the formation and/or the upgrade of the deposits but stressed that their observations alone are not sufficient for a hydrothermal model.

A very detailed sedimentological study of the Jacadigo Group was provided by Freitas et al. (2011). Based on sedimentological and stratigraphical data of diamictites, conglomerates, and the BIF deposit, they provided a detailed tectono-sedimentary evolution of the graben-system. The Urucum deposits were interpreted as gravitational basin fill during mid to late rift climax, without relations to a glacial environment, when a major reactivation tectonic event led to a starved setting in a lake or marine gulf setting. Simultaneous input of hydrothermal fluids into the lake/gulf provided Fe and Mn while clastic intercalations derived from debris flows and turbidites. The study provided a plausible alternative to the popular glaciogenic deposition model; however the authors consider their model to be no longer probable (personal correspondence with Bernardo T. Freitas). A pioneer study on structural analysis of the Jacadigo Group was provided by D'el-Rey Silva et al. (2016). They found that the rocks of the Jacadigo Group experienced progressive deformation in three major phases, recording the closure of the precursor basin of the Paraguay belt, and low-grade metamorphism during the Brasiliano Cycle. Angerer et al. (2016) provided a detailed study of petrographical, geochemical, Fe and C isotope data to propose a chemostratigraphic model for the Urucum deposits. Viehmann et al. (2016) further supported this notion, suggesting that ancient open-ocean water derived from (meta-)sediments and juvenile volcanic material as source of the REY (and other elements) budget with neglectable post-depositional alteration. Mn ore deposits were envisioned to have been deposited in shallower, more oxidized parts of the

basin with enhanced riverine influence. They found no influence of high-temperature hydrothermal fluids. In recent years several authors focused on better understanding the ore genesis of Urucum BIF. Biondi et al. (2017) provided a study focusing on Mn ore deposition, arguing multiple flooding events, where the Urucum basin was flooded with  $Mn^{2+}$  and  $CO_2$  rich waters, as well as several tectonic events causing the repeated collapse of the bottom of the Urucum basin, allowing deposition of the Mn-horizons. Sedimentation was microbial mediated when the water was shallow and the environment oxidizing. In situ EMP and LA-ICP-MS analysis on hematite were undertaken by de Souza et al. (2019), arguing for deposition in a shallow environment below storm wave base. They confirmed the previous observations of Angerer et al. (2016) and Viehmann et al. (2016) that argued for a redox-stratified basin water. High-resolution Raman and Fourier-transform infrared spectroscopy on Mn ore samples by Biondi et al. (2020) argue for suboxic and semi-neutral to alkaline conditions during deposition. Ore genesis is ascribed to a complex interplay of diagenetic processes, including microbial activity. Further evidence for a microorganisms mediated ore formation was provided by Polgári et al. (2021). They proposed a dual system of microbial induced ore formation which is characterized by the main Fe- and Mn-oxidizing metabolic processes. The deposition environment is thought as to be low temperature and suboxic, with a neutral to slightly acidic pH. Angerer et al. (2021) attributed the high iron grade (up to 65 wt% Fe) of the Urucum IF to late-diagenetic alteration processes and proposed a three-stage, post-sedimentary hydrothermal-supergene mineralization model.

### 2.3.1 Geochemistry of the Urucum iron formation

Several geochemical studies were conducted on the IF-Mn deposits of the Urucum district (e.g., Klein et al. 2004; Angerer et al. 2016; Viehmann et al. 2016). BIF samples have a high Fe content (45-56 wt%), which is almost exclusively present as  $Fe_2O_3$  (Klein et al. 2004). Fe-rich samples generally show low Ti and Al concentrations ( $TiO_2 < 0.031$ wt%,  $Al_2O_3 < 0.25$  wt%) that were derived from detrital contamination, suggested by the positive correlation of both elements. Mn-rich samples of the Mn-horizons have higher  $Al_2O_3$  concentrations (0.429 – 2.78 wt%) and variable, but generally lower, Fe/Mn ratios that decrease with increasing Mn and/or Al concentrations (e.g., Viehmann et al. 2016). Trace element concentrations in the Urucum IF cover a broad range, with IF samples showing the lowest amount of immobile elements (Zr, Ti, and Th) followed by Mn-rich samples, and clastic samples showing the highest amounts (e.g., Viehmann et al. 2016). The concentration of these elements is non-uniform, suggesting different degrees of clastic contamination. The  $REY_{SN}$ -patterns of IF samples are comparable to the  $REY_{SN}$ -pattern of modern seawater and generally form two groups of distinct fractionation patterns. Group 1 shows depletion in LREE and consistent negative  $Ce_{PAAS}$ , and positive

Gd<sub>PAAS</sub>- and Y<sub>PAAS</sub>-anomalies, while Group 2 is characterized by a stronger depletion in LREE, higher base metal concentration, and near absence of a Ce<sub>PAAS</sub>-anomaly (e.g., Angerer et al. 2016). Both groups also show negligible contamination of aluminosilicates, similarities to BIF samples of the Rapitan IF (e.g., Klein et al. 2004; Baldwin et al. 2012; Angerer et al. 2016) and little to no influence of post-depositional processes (e.g., Viehmann et al. 2016). These findings have been interpreted to reflect temporal changes in redox conditions in the restricted depositional basin, with the source of the elements being a mixture of open-ocean water masses, riverine input, and terrigenous detritus, with no indications for input from the mantle or high-temperature hydrothermal fluids (e.g., Viehmann et al. 2016). Angerer et al. (2021) attributed the high Fe and Mn ore quality of the Urucum IF ores to late-diagenetic alteration processes. They proposed a three-stage, post-sedimentary hydrothermal-supergene mineralization model, in which silica was removed from the IF during late diagenesis, followed by supergene carbonate-phosphorous leaching, leading to highly enriched and high-grade iron ore.

### 2.3.2 Isotope Geochemistry of the Urucum iron formation

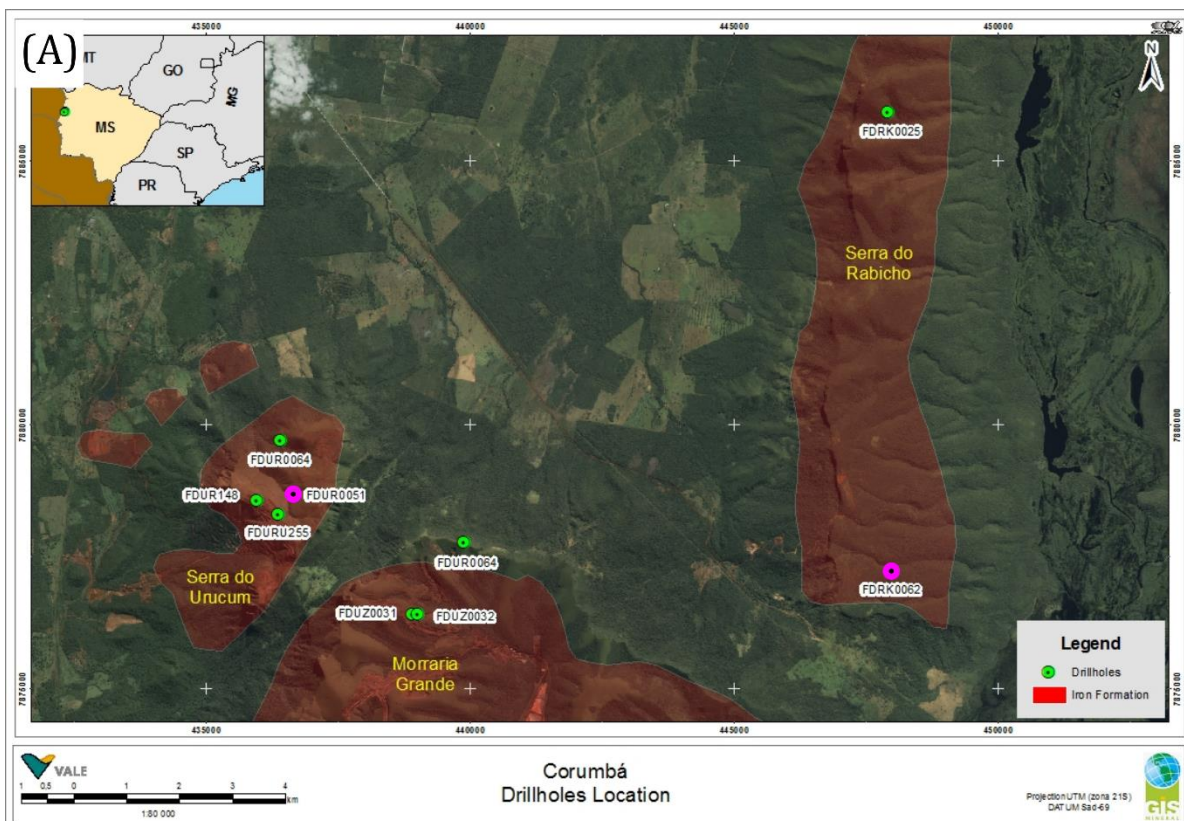
To better understand the genesis of Neoproterozoic Iron Formations, Klein et al. (2004) provided, among trace metal chemistry,  $\delta^{13}\text{C}$  values of carbonates from the Urucum IF, ranging from -5.2 to -7.0 ‰. These values are more negative than carbonates from the Rapitan IF (+0.83 to -3.37 ‰, Klein and Beukes 1993) and were argued to reflect a glacial setting. Similar values were reported by Angerer et al. (2016), showing  $\delta^{13}\text{C}$  values from dolomites with a total range of -3.4 to -7.0 ‰. Additional stable isotope analysis ( $\delta^{18}\text{O}$  and  $\delta^{13}\text{C}$ ) was provided by Polgári et al. (2021), with  $\delta^{18}\text{O}$  showing a broad range of values (-11.04 to +1.06 ‰).  $\delta^{13}\text{C}$  again show slightly negative values, from -2.53 to -5.01 ‰ and is considered to be an indicator for microbial activity. Angerer et al. (2016) also reported iron isotopes in hematite, showing negative  $\delta^{57}\text{Fe}$  values, ranging in total from -2.6 to 0.0 ‰. Each mineralogical group (dolomite-rich hematite BIF, chert-hematite BIF, hematite mud) show distinct data ranges, indicating lithologically controlled iron isotope fractionation. Similar values were found by Huang et al. (2021), who reported  $\delta^{56}\text{Fe}$  values for pure IF, impure IF, and Mn-F samples. They established a positive correlation between Fe/Mn ratios and  $\delta^{56}\text{Fe}$  values, with Mn-F samples having distinctively lower values. They related the low values to progressive partial oxidation via Rayleigh-type fraction. Frei et al. (2017) provided Cr isotope measurements, arguing for a surface Cr cycle under intense oxidating conditions, reflected by the strongly fractionated Cr isotope signature. Viehmann et al. (2016) reported Sm-Nd isotopic compositions for IF-, Mn-rich, and clastic samples. They generally show small variations in  $^{147}\text{Sm}/^{144}\text{Nd}$  values (0.1078

to 0.1359) and unradiogenic Nd values, being more negative than the values reported by Miller and O’Nions (1985), proposing that water masses precipitating in the Urucum, IF tapped their REE signatures from weathered and eroded rocks of the nearby Brasilia Belt.

### 3 Samples and Methods

#### 3.1 Samples

Iron formation samples selected and investigated in this thesis were acquired from two drillcores (FDUR0051 and FDRK0062), which intersected fresh and unweathered rocks of the Santa Cruz Formation (Fig.3.1A-B). The drillcores were taken in the 2010s by the Vale company, the then proprietor of the Urucum iron mines, as part of an mining evaluation of the Fe-Mn-ores. Drillcore FDRK0051 is located in the Serra do Urucum and encountered Mn-ore-horizons Mn1 and Mn2 as well as jaspilites and arkoses. The second drillcore FDRK0062 was drilled in the eastern Serra do Rabicho. It encountered hematitic and manganese-rich arkose, diamictites, arkoses, siltstones and jaspilites. These rocks show an excellent preservation compared to the usual Urucum rock record, which underwent intense and deep laterization accompanied by the removal Ca- and Si-rich mineral phases.



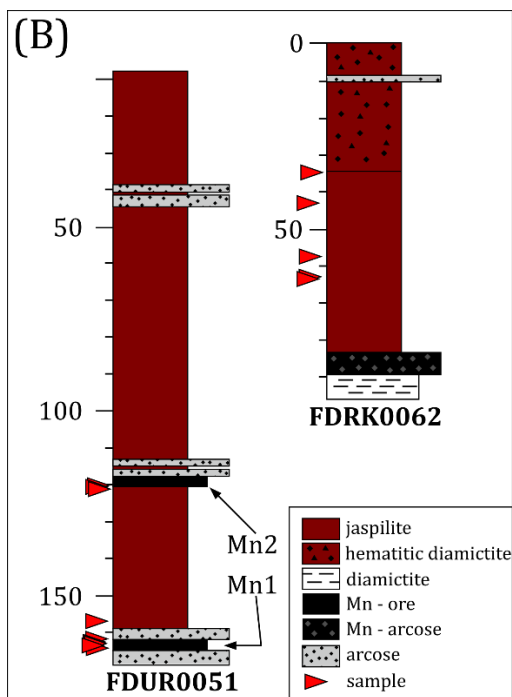


**Figure 3.1:** (A) Locations of the Urucum sample drill cores. This thesis uses sample material taken from drill cores FDRK0051 and FDRK0062 (marked in pink) taken and processed by Dr. Sebastian Viehmann. See Viehmann et al. (2016). Picture courtesy of Sebastian Viehmann. (B) Simplified column of the sample drill cores with marked samples used in this thesis. Modified after Viehmann et al. (2016) and Huang et al. (2021).

Sample preparation was done by Viehmann et al. (2016) at the Department of Physics and Earth Sciences at the Jacobs University of Bremen. Individual Si-, Fe-, and Mn-rich IF/Mn-F mesobands were cut using diamond saw blades. The individual mesobands were then milled in an agate mill to a fine powder, ensuring complete homogenisation. The homogenized powder of selected layers was then provided for this study. Geochemical characterization of these milled layers was provided by Viehmann et al. (2016) and Huang et al. (2021).

### 3.2 Methods

For Re-Os isotope and HSE analyses, approximately 0.2 to 0.3 g of whole rock powder was placed into quartz vials, followed by addition of a mixed  $^{185}\text{Re}$ ,  $^{190}\text{Os}$ ,  $^{191}\text{Ir}$ ,  $^{194}\text{Pt}$ ,  $^{99}\text{Ru}$  and  $^{105}\text{Pd}$  tracer solution. Two milliliters of HCl were then added in small increments to drive off  $\text{CO}_2$ . After cessation of  $\text{CO}_2$ -production, 5 ml of  $\text{HNO}_3$  were added to the samples. All sample-vials were sealed and treated for 4 hours at  $270^\circ\text{C}$  and 100-130 bars in an Anton-Paar high pressure asher at the Department of Lithospheric Research at the University of Vienna, Austria.

After opening the quartz vials, Os was separated from the other HSEs using a  $\text{CHCl}_3/\text{HBr}$  liquid extraction procedure (Cohen and Waters 1996). The Os-bearing HBr phase was then placed on a hot plate at  $60^\circ\text{C}$  and allowed to evaporate to complete dryness. Osmium was further purified using a  $\text{H}_2\text{SO}_4/\text{H}_2\text{CrO}_4$  microdistillation technique as described in Birck et al. (1997). After Os-extraction, all other HSEs were separated by ion-exchange chromatography using the procedure outlined in Pearson and Woodland (2000) (see Appendix 8-1 for recipes and further details regarding the ion exchange chemistry).

Measurements of Os concentrations and  $^{187}\text{Os}/^{188}\text{Os}$  ratios were carried out on a Thermo TRITON thermal ionization mass spectrometer in negative ion mode at the Department of Lithospheric Research at the University of Vienna, Austria. In thermal ionization mass spectrometry (TIMS), the desired element is placed on a metal filament and is then gently heated, causing the element to evaporate and ionize. In contrast to inductively coupled plasma mass spectrometry (ICP-MS) with ionization temperatures of several thousand degree Celsius. In TIMS elements from the sample are usually ionized at temperatures ranging from 800 to 2000 °C. The Re-Os isotopic system has long played only a minor role in geochronology because Re and Os were thought to be impossible to ionize and measure efficiently. However, the system became more prominent when it was discovered that both elements are efficiently ionized by ionizing them as negative ions (N-TIMS, e.g., Creaser et al 1991; Völkening et al. 1991). In negative mode Re and Os are ionized as separate oxides ( $\text{ReO}_4^-$  and  $\text{OsO}_3^-$ ), which makes the N-TIMS method unaffected by poor purification, although requiring a correction for the oxygen masses. The Triton TIMS at the Department of Lithospheric Research is equipped with a secondary electron multiplier, allowing to detect trace amounts of Os in the low pg range with signal intensities of typically up to 100.000 counts in single collector mode.

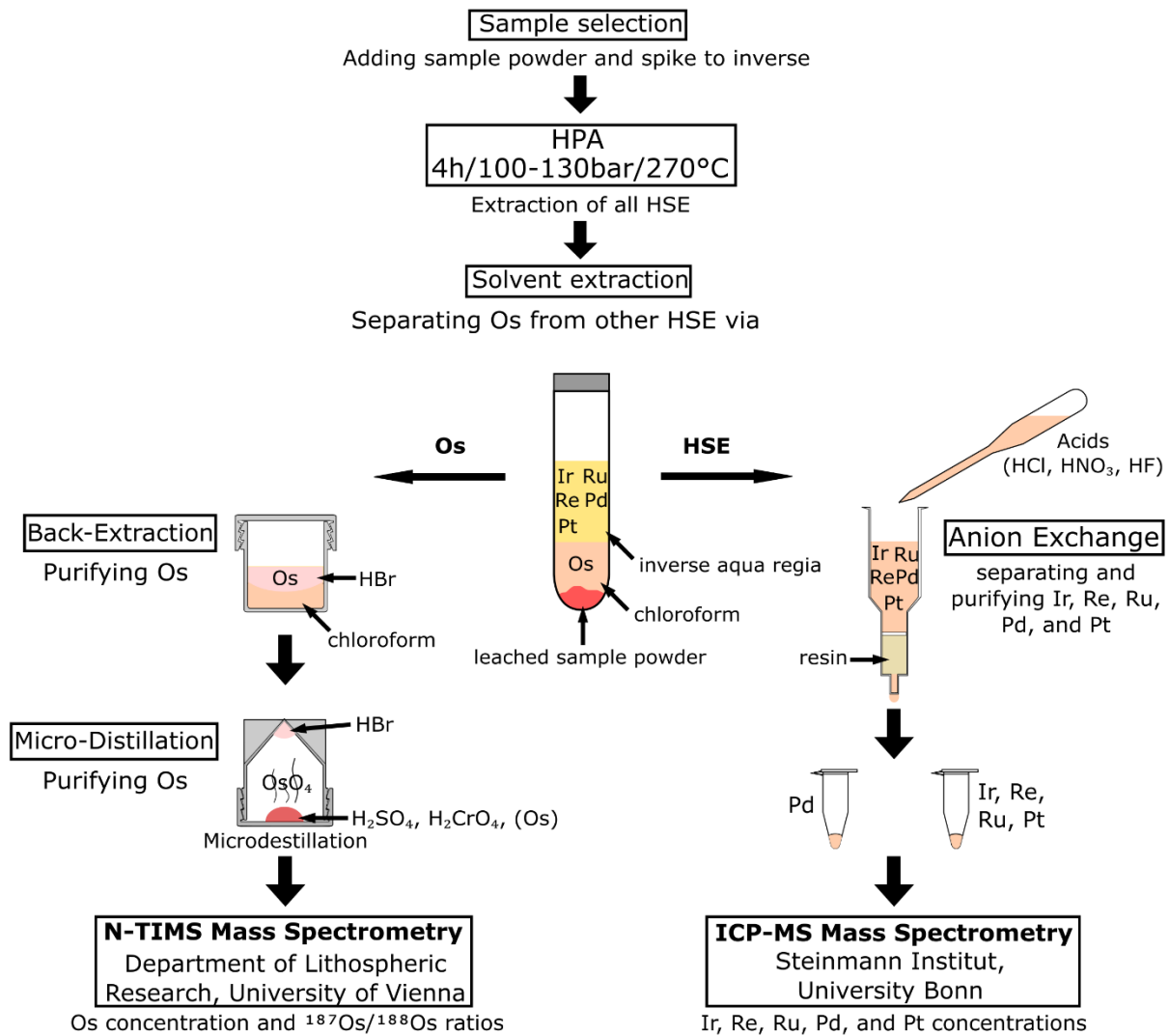


**Figure 3.2:** Graph depicting sample preparation and all steps of analytical methods applied in this study. Note that this is only an outline and many steps (e.g., the repeated evaporation during steps) are not depicted.

Prior to loading the sample onto single Pt filaments, the filaments were baked in air at high temperature for ~ 15min. (orange glow; e.g., Lugué et al. 2008). Osmium was then loaded as a bromide ( $\text{OsBr}_6^{2-}$ ) and covered with a  $\text{NaOH}/\text{Ba}(\text{OH})_2$  activator. The  $\text{NaOH}/\text{Ba}(\text{OH})_2$  activator acts as a source of O, allowing for more efficient ionization of Os. While isobaric interferences, attributable to W- or Pt-oxides, were not observed, isobaric interferences of  $^{187}\text{Re}$  on  $^{187}\text{Os}$  were significant in some cases and monitored by measuring  $^{185}\text{ReO}^{3-}$  (mass 233) and corrected, if observed (typically less than 5 to 10 counts on mass 233). Mass fractionation was corrected offline using  $^{192}\text{Os}/^{188}\text{Os} = 3.083$  (Brandon et al., 2005, Lugué et al., 2008). In some runs, oxygen was bled into the vacuum chamber of the mass spectrometer in order to raise ionization yields. The Os blank was ~ 0.9 ppt and required a blank correction for all samples. In addition to sample measurements, repeated measurements ( $n=5$ ) of 10 pg loads of a DROsS (Durham Romil Osmium Standard) solution were performed. The measurements were

performed using the electron multiplier at signal intensities that were typically achieved during the sample runs ( $\sim 1.000$  to  $\sim 100.000$  counts on mass  $240 = {}^{192}\text{OsO}^{-3}$ ) and were within the range of literature data (e.g., Luguët et al. 2008).

Concentrations for selected HSEs were obtained using a Thermo Fisher Element XR ICP-MS in single collector mode at the Steinmann Institute at the University Bonn, Germany, using methods described in Luguët et al. (2015). A 1 ppb in-house multi-element HSE standard solution was used to monitor instrumental drift and measured at the beginning, middle, and end of the analytical session. Mass bias was corrected relative to this standard solution using ratios of 0.5986 for  ${}^{185}\text{Re}/{}^{187}\text{Re}$ , 0.5957 for  ${}^{191}\text{Ir}/{}^{193}\text{Ir}$  and 0.2117 for  ${}^{198}\text{Pt}/{}^{195}\text{Pt}$ . Corrections were seen to be insignificant for all samples. Isobaric interferences caused by Hf on Ir and Pt were monitored and corrected offline.

To determine the oxide production, Hf-doped 1 ppb HSE solutions were run at the beginning, middle, and end of each analytical session. Rhenium, Ir, and Pt were measured using a cyclonic borosilicate glass spray chamber. Total procedural blanks for this study were 4 pg for Re, 0.8 pg for Ir, 55 pg for Ru, 37 pg for Pt and 56 pg for Pd. Blank correction was performed by direct subtraction of the blank contribution from the gross amount of analyte detected. Due to the samples HSE contents, blank corrections were applied in all cases, although in most cases insignificant. Analytical quality was monitored with repeated measurements of standard reference materials OKUM (Komatiite; Meisel et al., 2013) processed alongside the samples. All analyses of standard reference materials reproduce certified values within  $2\sigma$  error (see chapter below). Additional measurements of standard reference material IF-G were performed to further validate analytical measurement methods and calibration.

## 4 Results

### 4.1 Highly siderophile elements

The concentrations of selected HSEs vary for the analysed Urucum samples from 0.020 to 3.452 ppb for Re, from 0.015 to 4.380 ppb for Os, from 0.004 to 0.171 ppb for Ir, from 0.025 to 2.178 ppb for Pt, from 0.042 to 5.795 ppb for Ru, and from 0.309 to 2.309 ppb for Pd. Notably, the concentrations for all these elements overlap between the two drill-cores (FDUR0051 and FDRK0062). Urucum samples can be assigned to three major lithologies, namely Si-rich (chert), Fe-rich (IF), and Mn-rich (Mn-F) samples. Whenever appropriate, in the lithologies are separately discussed and labelled below, using different forms in the figures. Lithologies were defined by Viehmann et al. (2016), who also assigned samples into pure and impure based on their trace element trends (especially REY patterns).

**Table 1:** Highly siderophile elements data for iron-rich (IF), manganese-rich (Mn-F), and chert samples of Urucum. Sample IDs follow the notation of Viehmann et al. (2016).

Sample	Depth (m)	Type	Re (ng/g)	2s	Os (ng/g)	2s	Ir (ng/g)	2s	Pt (ng/g)	2s	Ru (ng/g)	2s	Pd (ng/g)	2s
UR51_10	120.20 - 120.30	Mn-rich BIF	0.109	0.002	0.269	0.009	0.005	0.002	0.553	0.031	0.817	0.005	0.609	0.016
UR51_14	120.95 - 121.00	Mn2	0.205	0.002	4.380	0.201	0.004	0.001	2.178	0.024	0.299	0.008	0.414	0.013
UR51_15	120.95 - 121.00	Mn2	0.694	0.080	0.021	0.004	0.024	0.006	0.285	0.038	1.689	0.018	1.223	0.087
UR51_16	120.95 - 121.00	Mn2 ark	0.033	0.002	0.030	0.004	0.016	0.003	0.480	0.018	0.444	0.005	0.586	0.027
UR51-20	143.25 - 143.45	IF	1.661	0.025	-	-	0.015	0.004	0.322	0.030	5.795	0.193	1.882	0.112
UR51_26	158.25 - 158.45	IF	0.098	0.004	0.082	0.003	0.009	0.001	0.099	0.015	0.042	0.001	0.312	0.015
UR51_30	161.30 - 161.50	IF	1.800	0.032	0.031	0.002	0.023	0.007	0.235	0.047	0.111	0.001	0.309	0.025
UR51_35	163.15 - 163.35	IF arkose	0.273	0.003	0.164	0.008	0.007	0.002	0.116	0.031	0.385	0.005	0.565	0.036
UR51_40	163.85 - 164.05	IF	0.388	0.006	0.359	0.035	0.031	0.011	0.963	0.029	4.757	0.176	2.309	0.143
UR51_45	164.35 - 164- 55	Mn1 (B)	0.982	0.012	0.529	0.006	0.099	0.003	0.732	0.021	1.761	0.024	1.782	0.039
UR51_47	164.35 - 164- 55	IF	0.020	0.005	0.115	0.003	0.126	0.008	0.524	0.052	0.699	0.006	0.805	0.034
UR51_51	165.00 - 165.15	Mn1 ark (A)	0.346	0.006	0.030	0.009	0.005	0.002	0.122	0.024	2.736	0.064	1.391	0.061
UR51_53	165.45 - 165.55	Mn1 ark (A)	0.981	0.011	0.241	0.027	0.018	0.001	0.272	0.021	3.013	0.049	1.391	0.052
UR51_55	166.40 - 166.50	Mn1 (B)	0.372	0.004	0.120	0.007	0.171	0.001	0.567	0.022	2.998	0.046	1.396	0.024
UR51_56	166.40 - 166.50	Mn1 (B)	0.699	0.006	0.223	0.009	0.072	0.003	0.628	0.013	0.220	0.002	1.058	0.026
UR51_70	168.75 - 168.85	IF	0.942	0.008	0.048	0.005	0.014	0.005	0.174	0.032	0.386	0.003	0.727	0.039
UR62_11	34.95 - 35.00	IF	3.452	0.073	0.331	0.007	0.005	0.002	0.025	0.001	0.712	0.013	0.513	0.001
UR62_15	43.70 - 43.90	IF	3.114	0.062	0.015	0.005	0.004	0.001	0.230	0.016	1.793	0.032	0.608	0.037
UR62_17	43.70 - 43.90	IF	0.985	0.016	0.036	0.002	0.007	0.003	0.128	0.030	5.073	0.173	1.325	0.087
UR62_25	58.60 - 58.70	IF	1.355	0.018	0.026	0.001	0.012	0.005	0.334	0.032	0.185	0.002	0.610	0.039
UR62_30	62.25 - 62.30	chert	2.166	0.022	3.349	0.150	0.007	0.004	0.307	0.022	0.665	0.016	0.547	0.029
UR62_31	62.25 - 62.30	IF	2.435	0.035	0.031	0.003	0.023	0.007	0.235	0.047	0.346	0.003	0.847	0.060
IFG <sup>e</sup>		Bulk BIF	0.171	-	0.029	-	0.005	-	0.164	-	-	-	-	-
IFG <sup>f</sup>		Bulk BIF	0.1408	0.0067	0.024	0.002	0.003	0.0018	0.280	0.027	1.208	0.014	0.606	0.026
OKUM <sup>a</sup>		Komatiite	0.566	0.08	0.79	-	0.943	0.08	11.44	-	4.15	0.08	12.2	1.46
OKUM <sup>b</sup>		Komatiite	-	-	0.78	-	0.99	0.07	11.44	-	4.53	-	11.93	-
OKUM <sup>c</sup>		Komatiite	0.475	-	0.79	-	0.843	-	10.7	-	4.19	-	11.1	-
OKUM <sup>d</sup>		Komatiite	0.471	-	0.722	-	0.813	-	12.6	-	4.4	-	11.5	-
OKUM <sup>e</sup>		Komatiite	0.514	-	0.746	-	0.812	-	12.14	-	-	-	-	-
OKUM <sup>f</sup>		Komatiite	0.461	0.014	0.811	0.015	0.868	0.022	11.93	0.28	3.835	0.207	13.28	0.21

<sup>a</sup>Savard et al. (2010) <sup>c</sup>Chen et al. (2016) <sup>e</sup>Schulz et al. (2021)

<sup>b</sup>Maier et al. (2012) <sup>d</sup>Puchtel et al. (2018) <sup>f</sup>this study

Iron formations (IF) samples from both drill-cores vary from 0.020 to 3.45 ppb for Re, from 0.015 to 0.359 ppb for Os, from 0.004 to 0.126 ppb for Ir, from 0.025 to 0.963 ppb for Pt, from 0.111 to 5.073 ppb for Ru, and from 0.309 to 2.309 ppb for Pd. IF-samples from drill-core FDRK0062 generally show higher Re concentrations (from 0.965 to 3.45 ppb Re) than IF sample from drill-core FDRK0051 (from 0.273 to 1.80 ppb Re). Contrary, samples of Mangan formations (Mn-F) were only encountered by drill-core FDRK0051. They vary from 0.033 to 0.982 ppb for Re, from 0.021 to 4.38 ppb for Os, from 0.004 to 0.171 for Ir, from 0.122 to 2.178 ppb for Pt, from 0.220 to 3.013 ppb for Ru, and from 0.414 to 1.782 ppb for Ru. Only one sample (UR62\_30) in our dataset represents Si-rich (chert) lithologies. Their HSE concentrations are 2.166 ppb for Re, 3.349 ppb for Os, 0.007 ppb for Ir, 0.307 ppb for Pt, 0.665 ppb for Ru, and 0.547 ppb for Pd.

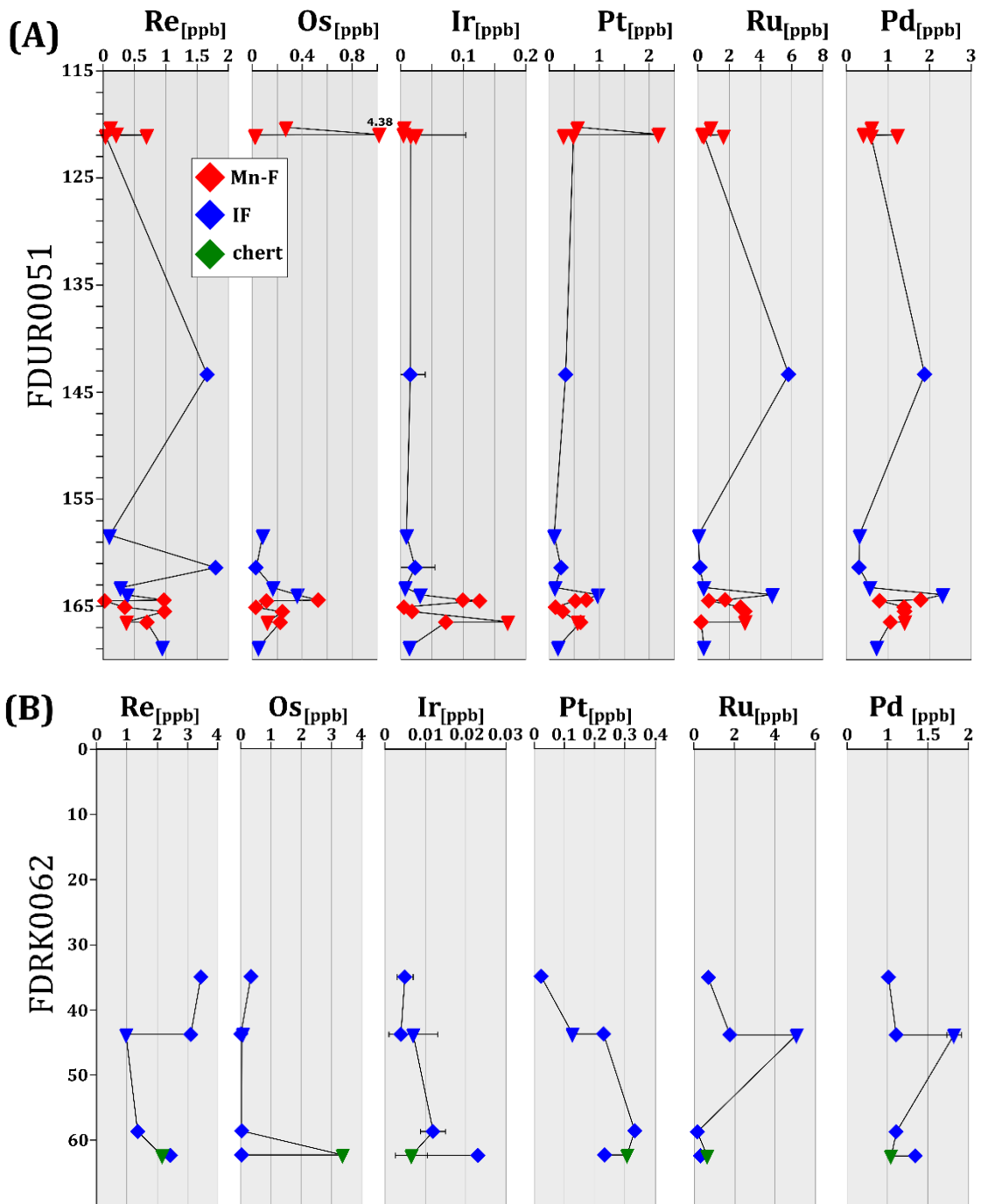


**Figure 4.1:** Stratigraphic distribution of measured HSEs of the Urucum samples of drill core FDUR0051 (A) and FDRK0062 (B). Isochronic samples (discussed below) are plotted as triangles.

Interelement ratios in Urucum samples cover a broad range of magnitudes. They are ranging from 0.17 to 201 for Re/Os, from 0.16 to 779 for Re/Ir, from 0.04 to 138 for Re/Pt, from 0.009 to 0.24 for Ir/Pt, from 0.91 to 515 for Os/Ir, and from 0.07 to 13.2 for Os/Pt in IF samples. In Mn-F samples, ratios range from 0.05 to 33.1 for Re/Os, from 2.06 to 69.2 for Re/Ir, from 0.07 to 2.84 for Re/Pt, from 0.002 to 0.30 for Ir/Pt, from 0.70 to 1095 for Os/Ir (from 0.70 to 13.4 excluding UR51\_14), and from 0.06 to 2.01 for Os/Pt. Chert samples UR51\_26 and UR62\_30

show Re/Os ratios of 1.29 and 0.65, Re/Ir ratios of 10.89 and 333, Re/Pt ratios of 0.99 and 7.06, Ir/Pt ratios of 0.091 and 0.021, Os/Ir ratios of 9.11 and 515, and Os/Pt ratios of 0.83 and 10.9, respectively. These values cover average values from all three possible sources that might contribute to the seawater chemistry: (i) crustal rocks (Re/Os = 6.387, Re/Ir = 9.000, Re/Pt = 0.388, Ir/Pt = 0.043, Os/Ir = 1.409, and Os/Pt = 0.061; Peucker-Ehrenbrink and Jahn 2001), (ii) mantle rocks (Re/Os = 0.09, Re/Ir = 0.10, Re/Pt = 0.05, Ir/Pt = 0.46, Os/Ir = 1.11, and Os/Pt = 0.51; Becker et al. 2006), and (iii) chondrites (Re/Os = 0.08, Re/Ir = 0.09, Re/Pt = 0.04, Ir/Pt = 0.49, Os/Ir = 1.07, and Os/Pt = 0.53; Horan et al. 2003). Interelement ratios follow a systematic trend, with Ir concentrations and Re/Os ratios becoming more variable with increasing Pt concentrations (Fig.4.2D). Samples with Pt concentrations between 0.5 and 1.0 ppb can reach Ir concentrations of up to 0.17 ppb, while samples outside of that Pt range only reach a maximum Ir concentration of 0.03 ppb.

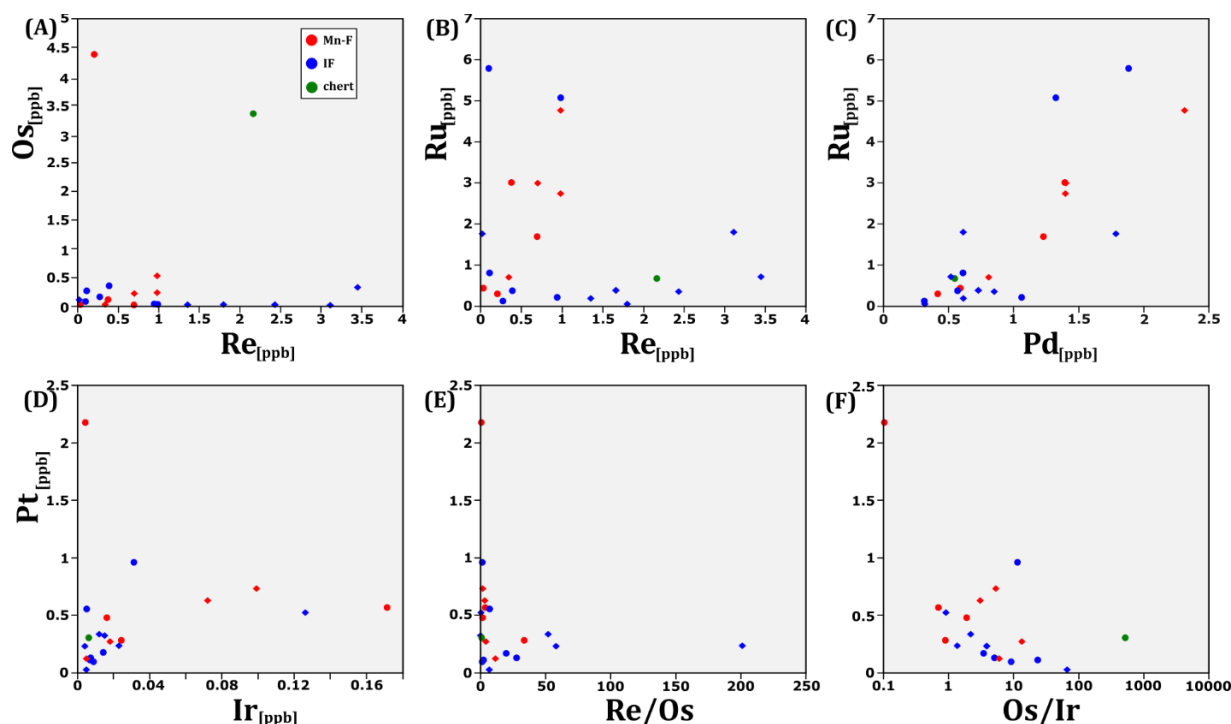


**Figure 4.2:** Interelement correlations between Re and Os (A), Ru and Re (B), Ru and Pd(C), and Pt and Ir (D), the Re/Os (E), and the Os/Ir ratio (F) of the Urucum samples. Isochronic samples (discussed below) are displayed as circles.

Additionally, samples show two distinctive trends in a Ru vs Re diagram, with one group of samples showing variable Ru concentrations and low Re content and vice versa (Fig.4.2B). Higher Ru concentrations are paired with higher Pd concentrations (Fig.4.2C). High Ru/low Re samples are primarily of the Mn-F-type, while low Ru/high Re samples are IF and chert samples. A linear increase of Ru with Pd can also be observed, with IF samples showing a broader distribution, while Mn-F samples increase in a more linear fashion (Fig.4.2C).

Repeated measurements of standard material OKUM yield a weighted average of 0.461 ppb for Re, 0.977 ppb for Os, 0.868 ppb for Ir, 11.93 ppb for Pt, 3.835 ppb Ru, and 13.28 ppb Pd. Standard material IFG yields a weighted average of 0.141 ppb for Re, 0.024 ppb for Os, 0.003 ppb for Ir, 0.280 ppb for Pt, 1.208 ppb for Ru and 0.606 ppb for Pd. Both standard materials are within  $2\sigma$  error margin of previously published measurements (Table. 5.1).

Datasets for HSEs in other BIFs in general are sparse. The existing studies were undertaken on older (Archean to Paleoproterozoic) formations that lack a distinct manganese-rich lithology. Koeberl et al. (2000) reported HSE concentrations for the ~ 3.8 Gy old Isua BIF, which range from below detection limit (for the used method, INAA: 20 ppt) to 0.18 ppb for Ir and up to 1.20 ppb for Pt for whole rock samples. Suzuki and Kato (2003) reported HSE data for individual bands of the same BIF. They report concentrations that range from 0.003 to 0.015 ppb and from 0.015 to 0.045 ppb for Os and Re, respectively. Siebert et al (2005) present a dataset of HSE concentrations for the ~ 3.1 Gy old Moodie Group of the Barberton Greenstone belt. They report Os concentrations of 0.016 and 0.042 ppb for two whole rock samples and 0.022 ppb and 0.057 ppb for a chert and magnetite sample, respectively. Re concentrations range from 0.025 to 0.075 ppb, for a whole rock sample concentrations of 0.011 ppb Ir and 0.053 ppb Pt were also reported. Ripley et al. (2008) reported Re-Os abundance and the Os isotopic composition of magnetite samples of the Biwabik Iron Formation, Lake Superior area. Rhenium concentrations for these samples range from ~ 0.011 to ~0.492 ppb, Os concentrations range from ~0.010 to ~ 0.082 ppb. The most recent and detailed study was presented by Schulz et al. (2021) on HSEs of the ~ 2.7 Gy old Temagami BIF. They report concentrations ranging from 0.011 to 3.996 ppb for Re, from 0.001 to 0.417 ppb for Os, from 0.001 to 0.104 ppb for Ir, and from 0.012 to 0.885 ppb for Pt.

The dataset for the concentrations of the HSEs in the Urucum Iron Formation, as well as interelement ratios, are largely comparable to those previously reported. However, the highest values for Os are up to one magnitude higher in the Urucum iron formation than in any other studied BIFs.

## 4.2 Re-Os Isotopes

Measured ratios for the for the analysed Urucum samples range from 0.22 to 976 for present-day  $^{187}\text{Re}/^{188}\text{Os}$  ratios and from 0.11 to 2.20 ppb for present-day  $^{189}\text{Os}/^{188}\text{Os}$  ratios. As with the concentration of HSE, the measured ratios overlap between the two drill-cores (Fig. 4.3A-B). Present-day  $^{187}\text{Os}/^{188}\text{Os}$  ratios show a continual growth from mantle-like ratios to highly radiogenic ratios, but this increase neither correlates with drill-cores, stratigraphy, or lithology. Iron formation samples have ratios from 0.89 to 1007 for  $^{187}\text{Re}/^{188}\text{Os}$ , and ratios from 0.1434 to 2.2028 for  $^{187}\text{Os}/^{188}\text{Os}$ . Manganese formation samples show ratios from 0.22 to 198.5 for  $^{187}\text{Re}/^{188}\text{Os}$  and ratios from 0.1103 to 2.097 for  $^{187}\text{Os}/^{188}\text{Os}$ . Chert sample UR62\_30 shows a

$^{187}\text{Re}/^{188}\text{Os}$  ratios of 3.09, and a  $^{187}\text{Os}/^{188}\text{Os}$  ratio of 0.1430. There seems to be no effect of the lithology on the  $^{187}\text{Re}/^{188}\text{Os}$  and  $^{187}\text{Os}/^{188}\text{Os}$  ratios, as all measured ratios overlap between the three lithologies. Both IF and Mn-F samples (Chert samples excluded, as there is only one) show  $^{187}\text{Re}/^{188}\text{Os}$  ratios that cover four ranges of magnitude.

**Table 2:** Highly siderophile elements data for iron-rich (IF), manganese-rich (Mn-F), and chert samples of Urucum. Sample IDs follow the notation of Viehmann et al. (2016).

Sample	Depth (m)	Type	$^{187}\text{Re}/^{188}\text{Os}$	2s	$^{187}\text{Os}/^{188}\text{Os}$	2s	$(^{187}\text{Os}/^{188}\text{Os})_0$
UR51_10	120.20 - 120.30	Mn-rich BIF	1.93	0.09	0.1434	0.0034	0.124
UR51_14	120.95 - 121.00	Mn2	0.22	0.01	0.1103	0.0080	0.108
UR51_15	120.95 - 121.00	Mn2	198.5	49.53	2.097	0.026	0.147
UR51_16	120.95 - 121.00	Mn2 ark	5.25	0.9	0.1619	0.011	0.110
UR51-20	143.25 - 143.45	IF	-	-	-	-	-
UR51_26	158.25 - 158.45	IF	5.72	0.46	0.1638	0.0053	0.108
UR51_30	161.30 - 161.50	IF	477	0.1	0.1233	0.0051	-4.564
UR51_35	163.15 - 163.35	IF arkose	7.98	0.49	0.1869	0.0048	0.109
UR51_40	163.85 - 164.05	IF	5.17	0.65	0.1654	0.0015	0.115
UR51_45	164.35 - 164- 55	Mn1 (B)	9.22	0.22	0.4518	0.0010	0.361
UR51_47	164.35 - 164- 55	IF	0.89	0.08	0.6512	0.0084	0.642
UR51_51	165.00 - 165.15	Mn1 ark (A)	55.88	25.34	0.2626	0.0070	-0.287
UR51_53	165.45 - 165.55	Mn1 ark (A)	19.44	2.7	0.1510	0.0078	-0.040
UR51_55	166.40 - 166.50	Mn1 (B)	15.03	1.08	0.27	0.0050	0.118
UR51_56	166.40 - 166.50	Mn1 (B)	14.98	0.76	0.1456	0.0019	-0.002
UR51_70	168.75 - 168.85	IF	106.2	11.98	1.1572	0.033	0.113
UR62_11	34.95 - 35.00	IF	49.81	2.15	0.14	0.018	-0.349
UR62_15	43.70 - 43.90	IF	1007	533.42	0.2669	0.0076	-9.63
UR62_17	43.70 - 43.90	IF	156.7	11.91	1.655	0.036	0.115
UR62_25	58.60 - 58.70	IF	302.9	16.3	1.79	0.012	-1.19
UR62_30	62.25 - 62.30	chert	3.09	0.18	0.14	0.0028	0.113
UR62_31	62.25 - 62.30	IF	477.0	31.46	2.2028	0.0027	-2.48
IFG <sup>e</sup>		Bulk BIF	36.81	1.1	2.4720	0.0290	2.11
IFG <sup>f</sup>		Bulk BIF	37.85	-	2.8030	0.0600	2.43
OKUM <sup>a</sup>		Komatiite	-	-	-	-	-
OKUM <sup>b</sup>		Komatiite	-	-	-	-	-
OKUM <sup>c</sup>		Komatiite	-	-	0.2690	-	-
OKUM <sup>d</sup>		Komatiite	-	-	0.2778	0.0001	-
OKUM <sup>e</sup>		Komatiite	-	-	0.2930	-	-
OKUM <sup>f</sup>		Komatiite	2.29	-	0.2771	0.0027	0.255

<sup>a</sup>Savard et al. (2010) <sup>c</sup>Chen et al. (2016) <sup>e</sup>Schulz et al. (2021)

<sup>b</sup>Maier et al. (2012) <sup>d</sup>Puchtel et al. (2018) <sup>f</sup>this study

The DROsS measurements yielded an average of  $0.16098 \pm 78$  for  $^{187}\text{Os}/^{188}\text{Os}$ ,  $1.2123 \pm 56$  for  $^{189}\text{Os}/^{188}\text{Os}$ , and  $1.9805 \pm 95$  for  $^{190}\text{Os}/^{188}\text{Os}$  ratios (errors refer to the last two digits). These values agree within the  $2\sigma$  uncertainty of the average values reported by Luguet et al. (2008), obtained for much larger Os loads of DROsS.

Plotting the present day  $^{187}\text{Os}/^{188}\text{Os}$  ratios of all samples against their  $^{187}\text{Re}/^{188}\text{Os}$  ratios reveals a highly rough correlation corresponding to an age of  $245 \pm 4.682$  Ma and an initial  $^{187}\text{Os}/^{188}\text{Os}$  ratios of  $0.225 \pm 0.0153$  (MSWD = 50000; Fig.5.4A).

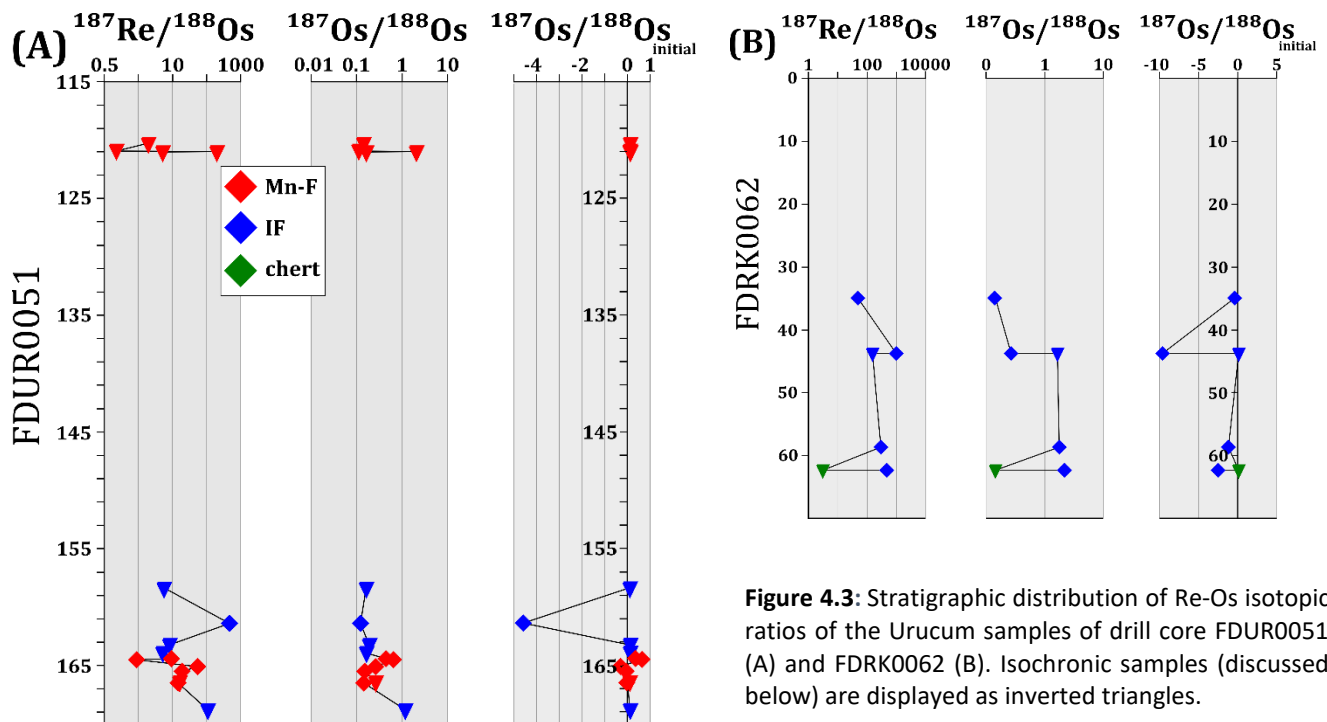


**Figure 4.3:** Stratigraphic distribution of Re-Os isotopic ratios of the Urucum samples of drill core FDUR0051 (A) and FDRK0062 (B). Isochronic samples (discussed below) are displayed as inverted triangles.

Previously reported  $^{187}\text{Re}/^{188}\text{Os}$  and  $^{189}\text{Os}/^{188}\text{Os}$  ratios are largely comparable to the data presented here. Suzuki and Kato (2013) reported initial  $^{189}\text{Os}/^{188}\text{Os}$  ratios of 0.12 – 2.1 for the Isua BIFs. Siebert et al. (2005) reported  $^{189}\text{Os}/^{188}\text{Os}$  ratios ranging from ~0.27 to ~0.61 for the same formation. For the Biwabik Iron Formation, Ripley et al. (2008) reported  $^{187}\text{Re}/^{188}\text{Os}$  ratios ranging from 5.77 to 60.24 and  $^{189}\text{Os}/^{188}\text{Os}$  ratios ranging from 0.57 to 1.42. The present-day best Re-Os isotope data were reported by Schulz et al. (2021) for the Temagami BIF. These authors presented  $^{187}\text{Re}/^{188}\text{Os}$  ratios ranging from 0.607 to 183.5,  $^{187}\text{Os}/^{188}\text{Os}$  ratios ranging from 0.173 to 10.8, and initial  $^{187}\text{Os}/^{188}\text{Os}$  ratios ranging from 0.014 to 1.065.

## 5 Discussion

It has been argued that banded iron formations in general are reliable geochemical archives and retain the geochemical signature of their depositional environment (see Chapter 1.2.1.4). However, post-depositional alteration processes (i.e., weathering, fluid-rock interactions during diagenesis or a metamorphic event) are able to imprint a lasting effect on the geochemical budget of banded iron formations (or marine chemical sediments in general). Previous studies determined the influence of post-depositional alteration processes on samples via analysing the concentration of immobile and fluid-mobile elements, classifying samples into pure and impure. A detailed study on the HSE and Re-Os isotopic budget of an iron formation was

provided by Schulz et al. (2021), who analyzed the 2.7 Gy Temagami iron formation (Canada). They concluded that, besides a potential secondary overprint, primary HSE and Re-Os isotope signatures were still present, allowing to draw some conclusions about the age of BIF deposition via isochron dating and the  $^{187}\text{Os}/^{188}\text{Os}$  seawater composition of the Paleoproterozoic marine environment in which the Temagami deposition took place.

The Urucum banded iron formation in particular has been extensively studied and its robustness as a geochemical archive for ancient seawater composition has been demonstrated. Previous studies determined no significant metamorphic overprint of the Urucum succession (e.g., Trompette et al. 1998; Ussami et al. 1999; Viehmann et al. 2016), as well as a lack of weathering index minerals, indicating insignificant weathering of the studied facies (e.g., Angerer et al. 2016). Viehmann et al. (2016) provided observations on the sample purity by plotting geochemical proxies against immobile and fluid-mobile elements (to account for the impact of detrital aluminosilicates and fluid-rock interaction, respectively). They concluded that the drill core samples examined are some of the best-preserved chemical sediments of the Urucum IF available, but that some samples show significant, variable influence of continental detritus.

To evaluate if the same conclusions can be drawn for the HSE and Re-Os isotopic composition of the Urucum, the robustness of the data obtained in this work is again tested, as done previously by Viehmann et al. (2016). Once the purity is established, the age is discussed that was derived via isochron dating, the  $^{187}\text{Os}/^{188}\text{Os}$  seawater composition of the Neoproterozoic marine environment in which the Urucum deposition took place, as well as the possibility of the presence of a meteoritic component in the Urucum IF.

### 5.1 Impact of alteration on the Re-Os distribution in the Urucum samples

To assess if the mineralogy controls the Os isotopic composition,  $^{187}\text{Os}/^{188}\text{Os}$  is plotted against the MnO and FeO contents (Fig. 5.1A-B). The clearly separated lithologies (i.e., IFs and Mn-Fs), based on XRD and major element data (cf. Viehmann et al. 2016) however, exhibit no apparent correlation, as the  $^{187}\text{Os}/^{188}\text{Os}$  ratio neither rises nor falls systematically with increasing or decreasing FeO/MnO values. Whereas  $^{187}\text{Os}/^{188}\text{Os}$  ratios in IFs (ranging from ~62 to ~86 wt%  $\text{FeO}_{\text{total}}$ ; Viehmann et al. 2016) range from 0.14 to 2.20, MnO formations (ranging from ~38 to ~68 wt% MnO; Viehmann et al. 2016) vary similarly from 0.11 to 2.10.

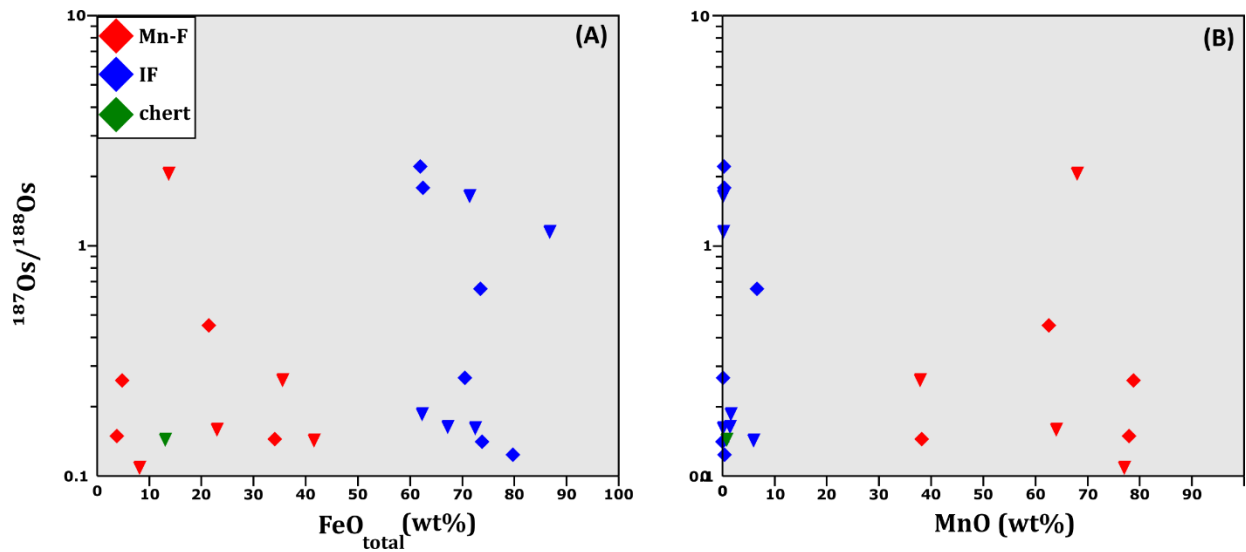


**Figure 5.1:** Diagrams of the  $\text{FeO}_t$  and MnO content against the  $^{187}\text{Os}/^{188}\text{Os}$  ratios (A and B, respectively) for the analyzed Urucum IF-Mn-F samples.  $\text{FeO}_t$  and MnO data was provided by Viehmann et al. 2016 (see Appendix 8-3 and 8-4).

A simple but powerful method to estimate for the extent of detrital contamination is to check the abundance of elements, such as Al, Zr and Ti in each sample. These elements are regarded as immobile in aqueous solutions, elevated concentrations are therefore regarded to be unrelated to seawater and being a contribution from continental hinterlands via weathering, erosion, or volcanic eruptions (e.g., Bau 1993; 1996). This method has proven to be reliable in estimating the extent of detrital aluminosilicates on the elemental budget of BIF (e.g., Bolhar et al. 2004; Kamber et al. 2004; Viehmann et al. 2015b; 2016). As mentioned above, Viehmann et al. (2016) already determined the impact of detrital contamination on the REY budget in the Urucum IF. We use the major and trace element measurements provided (see Appendix 8-3 and 8-4) of the same samples to determine the impact on their HSE budget (Fig. 5.2 and Fig. 5.3). Zr is not used as a detrital indicator as it is a particle reactive element and preferably sorbs on Mn-oxides.

## Detrital contamination

It is expected that Os or Re concentrations increase with Al concentration if detrital aluminosilicate contamination would play a role. However, as seen in Fig 5.2, there is no systematic increase in the Os or Re concentrations with increasing  $\text{Al}_2\text{O}_3$  concentrations in the samples. Re concentrations are highly diverse at low  $\text{Al}_2\text{O}_3$  abundances, covering two orders of magnitude (0.033 ppb to 3.45 ppb, Fig. 5.2A), and become more homogenous as the  $\text{Al}_2\text{O}_3$  content increases, not exceeding Re concentrations of 1 ppb (0.020 ppb to 0.981 ppb, Fig.5.2A). On the other hand, Os concentrations are similar regardless of Al content, ranging from 0.016 ppb to 0.529 ppb Os, with only two samples (UR51\_14 and UR62\_30) being the exception, showing Os concentrations of 4.38 and 3.35, respectively (Fig.5.2B). The detrital load introduced into the Urucum basin therefore had to have low concentrations of Os and Re, as otherwise, their concentration would increase with increasing  $\text{Al}_2\text{O}_3$  content. While our observations are therefore in agreement with Viehmann et al. (2016) concerning the classification of samples into pure (minimal detrital contamination) and impure (non-negligible contamination), an influence of the detrital aluminosilicates on the HSE budget, unlike the REY budget, cannot be observed. This leaves the question as to why samples with different  $\text{Al}_2\text{O}_3$  content show similar Re and Os concentrations. Additionally, both samples with high and low wt% of  $\text{Al}_2\text{O}_3$  show  $^{187}\text{Os}/^{188}\text{Os}$  initial ratios that group around 0.116, as well as negative  $^{187}\text{Os}/^{188}\text{Os}$  initial ratios.

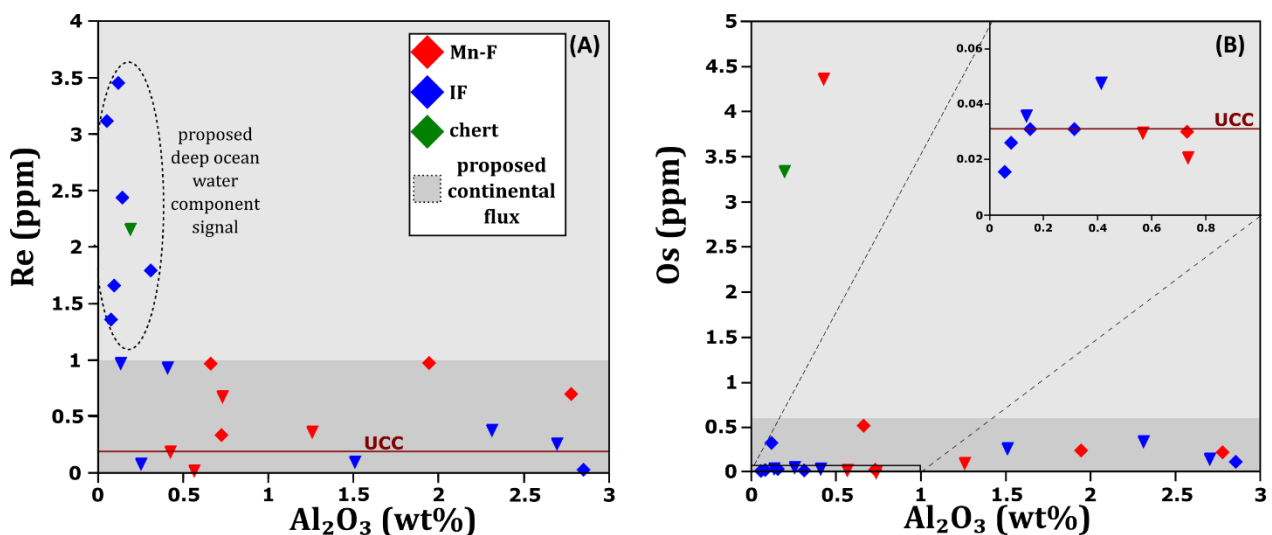


**Figure 5.2:**  $\text{Al}_2\text{O}_3$  concentrations of the Urucum samples against measured Re concentration (A) and Os concentration (B). Samples with high concentrations of Re and low amounts of  $\text{Al}_2\text{O}_3$  are proposed to represent a deep ocean water component. Samples with low concentrations of Re and variable amount  $\text{Al}_2\text{O}_3$  are proposed to represent the continental flux component. The average Re and Os concentrations of the upper continental crust (UCC) is depicted as a dark red line in both diagrams. Note that the line does not depict the average concentration of  $\text{Al}_2\text{O}_3$  in the UCC.  $\text{Al}_2\text{O}_3$  concentrations of the samples are taken from Viehmann et al. (2016) (see Appendix8-3 and 8-4). Re and Os concentrations of the UCC are taken from Peucker-Ehrenbrink and Jahn (2001).

The observations described can be explained by perceiving the Urucum samples as displaying different endmembers that compose the Urucum basin water. Samples with low  $\text{Al}_2\text{O}_3$  concentrations ( $>0.5$  wt%) and high concentrations of Re (above 1ppb Re) are proposed to represent the deep open seawater component. This component is most likely composed of low-temperature hydrothermal vent fluids, discharged and introduced into the basin from regional hydrothermal systems that were rich in the HSE and Fe (e.g., Huang et al. 2021). On the other hand, samples with lower concentrations of Re and Os and variable  $\text{Al}_2\text{O}_3$  contents are proposed to be representative of the continental flux, the mixture of riverine runoff, dissolved and suspended load, that was low in the HSE and high in  $\text{Al}_2\text{O}_3$ . They were most likely transported into the basin during periods of glacial retreat and mixed with the open seawater. The variable  $\text{Al}_2\text{O}_3$  concentrations are inherent to the amount of detritus in the sample and may even indicate which part of the flux was dissolved. Samples with low wt%  $\text{Al}_2\text{O}_3$  (UR51\_14, UR51\_15, UR51\_16, UR51\_26, UR51\_45, UR51\_51, UR51\_70 and UR62\_17) are more representative for the riverine waters while samples with high wt%  $\text{Al}_2\text{O}_3$  (UR51\_10, UR51\_35, UR51\_40, UR51\_47, UR51\_53, UR51\_55 and UR51\_56) representing clusters of continental aluminosilicates. Hence, samples UR51\_10, UR51\_35, UR51\_40 and UR51\_55, while being part of the linear regression line defined in the  $^{187}\text{Os}/^{188}\text{Os}$  vs  $^{187}\text{Re}/^{187}\text{Os}$  line, will not be considered in the further interpretation of the Os isotope chemistry of the Urucum basin water.

### **Post-depositional rock-fluid alteration**

To assess the effects of postdepositional fluid-rock interactions on our samples we plot our desired HSE parameters against the Sr content (Fig. 5.3A-B). Strontium is a large ion lithophile element and considered mobile during fluid transport. Paired with the good co-variation of Sr concentration and its radiogenic isotope composition in water, its characteristics make Sr an excellent tracer for fluid-rock interactions during diagenetic processes (e.g., Nebel 2016). Lowering Sr concentrations with the simultaneous increase of the contents of other elements, in this case Re and Os, would be seen as an indicator for abundant fluid-rock interactions. As a mobile element, Sr is leached from the rock during interaction with a fluid, while the fluid, in turn, provides additional elements that are incorporated into the rock chemistry.

Distribution patterns of Re and Os plotted against the Sr are similar to those when plotted against  $\text{Al}_2\text{O}_3$ . Rhenium concentrations of the Urucum samples again are highly diverse at Sr concentrations below 50 ppm, ranging from  $0.033 \pm 0.002$  ppb to  $3.45 \pm 0.073$  ppb. They become more uniform as the Sr content increases, ranging from  $0.109 \pm 0.002$  ppb to  $1.80 \pm 0.03$  ppb for samples with Sr concentrations higher than 50 ppm (Fig. 5.3A). Osmium

concentrations appear to be constant and remain within limited variability, ranging from  $0.026 \pm 0.001$  ppb to  $0.529 \pm 0.006$  ppb (samples UR51\_14 and UR62\_30 being the exception) at Sr concentrations below 50 ppm and ranging from  $0.030 \pm 0.009$  ppb to  $0.164 \pm 0.008$  ppb at higher Sr concentrations (Fig. 5.3B).

Samples with Sr concentrations < 50 ppm show either  $^{187}\text{Os}/^{188}\text{Os}$  ratios > 1.5 or < 0.5

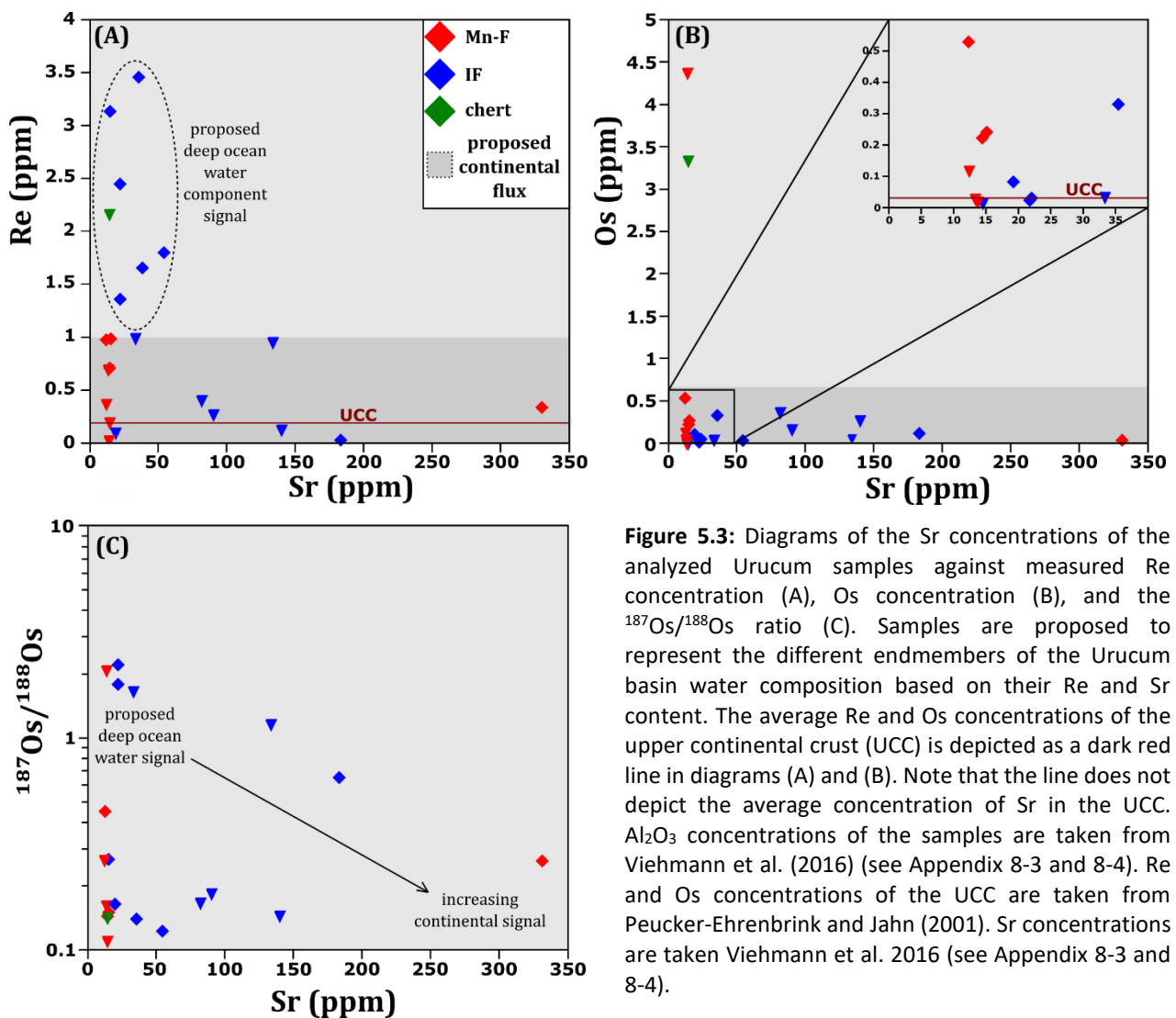


**Figure 5.3:** Diagrams of the Sr concentrations of the analyzed Urucum samples against measured Re concentration (A), Os concentration (B), and the  $^{187}\text{Os}/^{188}\text{Os}$  ratio (C). Samples are proposed to represent the different endmembers of the Urucum basin water composition based on their Re and Sr content. The average Re and Os concentrations of the upper continental crust (UCC) is depicted as a dark red line in diagrams (A) and (B). Note that the line does not depict the average concentration of Sr in the UCC.  $\text{Al}_2\text{O}_3$  concentrations of the samples are taken from Viehmann et al. (2016) (see Appendix 8-3 and 8-4). Re and Os concentrations of the UCC are taken from Peucker-Ehrenbrink and Jahn (2001). Sr concentrations are taken Viehmann et al. 2016 (see Appendix 8-3 and 8-4).

(Fig.5.3C). As the Sr concentrations increases, the ratios of the samples become less positive in a linear fashion, going from  $^{187}\text{Os}/^{188}\text{Os}$  ratios  $2.203 \pm 0.003$  at 22 ppm Sr to  $0.263 \pm 0.007$  at 331 ppm Sr (for samples with  $^{187}\text{Os}/^{188}\text{Os}$  ratios >1.5). Samples with less radiogenic  $^{187}\text{Os}/^{188}\text{Os}$  ratios ( $^{187}\text{Os}/^{188}\text{Os}$  ratios >0.5) reach a maximum  $^{187}\text{Os}/^{188}\text{Os}$  ratio of  $0.452 \pm 0.001$  at 12.3 ppm Sr, decreasing to  $^{187}\text{Os}/^{188}\text{Os}$  ratios of  $0.143 \pm 0.003$  at 140 ppm Sr (Fig. 5.3C). The provided data therefore would indicate a linear relation of Re and the  $^{187}\text{Os}/^{188}\text{Os}$  ratio with Sr, which would argue for higher levels of fluid/rock interaction. A significant influence of post-depositional alteration on the Re and Os budget of our Urucum samples could not be excluded,

making them an unsuitable starting point for geochemical reconstructions of the basement water. However, as already seen with the amount of  $\text{Al}_2\text{O}_3$  in our samples, samples with high as well as low Sr concentrations can show reasonable and similar initial  $^{187}\text{Os}/^{188}\text{Os}$  ratios (shown as reverse triangles in Fig. 5.3) For a sample to show high fluid-rock alteration and a  $^{187}\text{Os}/^{188}\text{Os}$  initial ratio similar to samples with little alteration, the alteration must have occurred simultaneous or shortly after deposition, as a later alteration would significantly affect the  $^{187}\text{Os}/^{188}\text{Os}$  ratio of a sample. Such processes, while not impossible, would be highly unlikely. This is further supported by the findings of Viehmann et al. (2016), who established only minor post-depositional alteration for the REE elements. Therefore, the observed relations between Re, Os and Sr are considered to not be an effect of altering fluid-rock interactions. Rather, a more plausible explanation can be drawn from the observations of syndepositional alteration. The selected Urucum samples are proposed to depict the different endmembers that compose the basin water of the Urucum basements. By having a continental flux that is rich in Al but low in HSE content, also providing high concentrations of Sr, trends between Re, Os and Sr as displayed in the present dataset can be achieved. Only samples with high concentrations of Re and Os are therefore considered in the interpretation of the Os isotopic composition of seawater. Four samples (UR51\_10, UR51\_35, UR51\_40, UR51\_70) with a “pristine”  $^{187}\text{Os}/^{188}\text{Os}$  initial ratio and high concentrations of Sr are therefore no longer considered in the further interpretation, as they reflect the influence of the continental flux. Samples UR51\_10, UR51\_35 and UR51\_40 already are no longer considered because they show high amounts of  $\text{Al}_2\text{O}_3$ , therefore, only UR51\_70 is affected.

To summarize, the dataset of the Urucum chemical sediments represents the Urucum basement water as a mixture of deep ocean water and a continental flux high in  $\text{Al}_2\text{O}_3$  and Sr. The ocean water component is characterized by variable but generally high concentrations of Re and Os, as well as low concentrations of  $\text{Al}_2\text{O}_3$  and Sr. The continental flux is characterized by low Re and Os concentrations and variable concentrations of  $\text{Al}_2\text{O}_3$  and Sr, depending on the amount of detritus within the sample. To better reflect the water component of the sample set, we therefore do not consider samples UR51\_10, UR51\_35, UR51\_40, UR51\_55 and UR51\_70 in our final linear regression line, as they show high  $\text{Al}_2\text{O}_3$  and/or high Sr concentrations.

## 5.2 Meteoritic component in the Urucum iron formation

HSE are common indicators for a meteoritic component because their concentrations are several orders of magnitudes higher in chondrites and iron meteorites than in terrestrial crustal rocks. Elevated abundances of the HSE in the Urucum samples relative to the composition of the upper continental crust (UCC) would, therefore, be an indicator for a meteoritic component

in the Urucum succession. Marine impact spherule layers have been identified in Paleo- and Neoproterozoic sedimentary successions (e.g., Lowe and Byerly 1986; Koeberl et al. 1993; Schulz et al. 2017), including some that are stratigraphically related to BIFs (Glikson and Hickmann 2014). They confirm the existence of massive (up to chondritic levels) HSE abundance peaks in marine Archean sediments, making BIFs useful archives in determining possible impact events prior or during their deposition.

The Cryogenian has been of special interest for impact-related research. Several authors reported elevated concentrations of HSE (in particular Ir and Os) in sedimentary successions related to the Sturtian and Marionan glaciations (e.g., Bodiselitsch et al. 2005; Peucker-Ehrenbrink and Hoffman 2006; see Waters et al. 2009, for an opposing view). Koeberl et al. (2007a, b) proposed that the reported HSE anomalies were the result of an impact event,

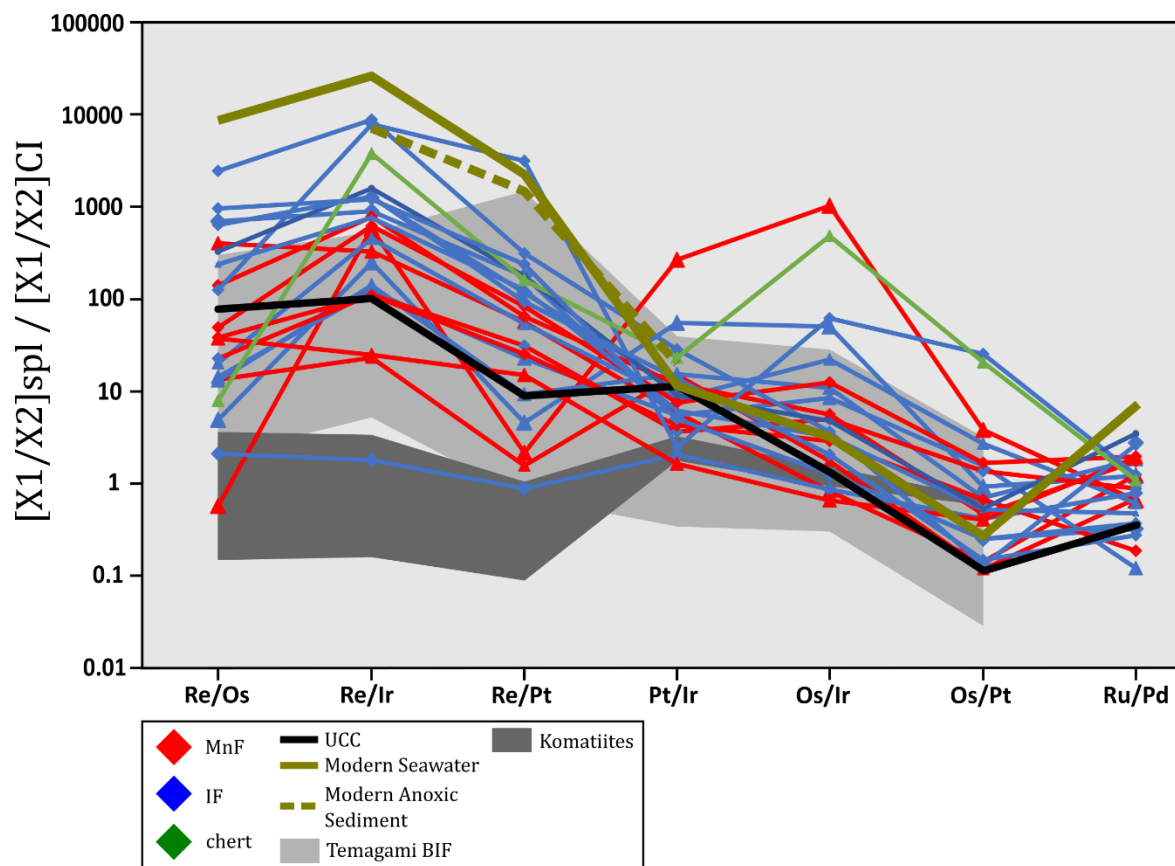


**Figure 5.4:** Comparison of CI-normalized highly siderophile interelement ratios for measured samples, nonmarine, and marine samples. Ratios of the UCC by Peucker-Ehrenbrink and Jahn (2001), the ratios modern seawater were derived from the studies reported in chapter (1.3.1.1.). Ratios of modern anoxic sediments by Ravizza (1991), of komatiites by Puchtel et al. (2014), and of the Temagami BIF by Schulz et al (2021).

triggering a deglaciation and an end to the Snowball (hard or soft) conditions. While an impact of an asteroid alone would not be enough to cause long term changes in the climate evolution of Earth, the resulting presence of a large water vapor plume could influence weather conditions on a global level (e.g., Koeberl and Ivanov 2019). Additionally, two late Neoproterozoic impact structures are currently known: the ~ 646 Ma old impact structure in

Strangways, Northern Australia (Spray et al. 1999) and the ~ 590 Ma old Acraman impact structure, South Australia (Williams and Schmidt 2020).

Urucum samples of this study show crustal to supracrustal concentrations of highly siderophile elements (Table 1). While their Os content can exceed that of the average UCC by up to two orders of magnitude (UR51\_14 and UR62\_30), the Urucum samples are practically devoid of Ir and Pt (UR51\_14 being an exception, with Pt concentrations of 2.17 ppb). While samples generally trend to unradiogenic, chondrite-like  $^{188}\text{Os}/^{187}\text{Os}$  ratios, the lack of enhanced concentrations of HSE in the Urucum BIF point to the lack of a significant meteoritic component. Instead, the unradiogenic values are more likely achieved by a significant contribution of mantle-derived sources, such as the input of hydrothermal vent systems. While the lack of a pronounced positive Eu anomaly would argue against the presence of hydrothermal fluids in the basin water, several authors have argued in favour of low-temperature (<150°C) hydrothermal vent fluids. They are particularly appealing as these fluids do not have to show an Eu enrichment (e.g., Michard et al. 1993; Alexander et al. 2008).

Chondrite-normalized HS interelemental ratios of the Urucum samples all show high fractionation, with Re/Os, Pt/Ir, and Os/Pt ratios being less fractionated compared to the Re/Ir, Re/Pt and Os/Ir ratios (Fig. 5.4). They are significantly higher than comparable ratios of komatiites (mantle-derived ultramafic volcanic rocks) and can even reach orders of magnitude that can be found in modern seawater. Additionally, ratios of several samples overlap with typical anoxic marine sediments (Fig. 5.4). As such anoxic sediments are a sink for Re, the overlap of several Urucum samples supports the interpretation of anoxic conditions in the Urucum basin during deposition. These observations are largely in agreement with the findings by Schulz et al. (2021). The Urucum samples largely overlap with ratios of the Temagami BIF; however, the Urucum BIF generally shows a higher fractionation and higher Re/Ir ratios. The present findings do not support the presence of a meteoritic component in the Urucum BIF.

### 5.3 The significance of the Re-Os isotope stratigraphy in the Urucum iron formation

If the measured Re-Os isotopic data are a genuine representation of the Neoproterozoic seawater composition, it should be possible to derive a precise isochron from them. As already established above, an isochron plot of all analysed samples yields an extremely unprecise age of  $254 \pm 4.682$  Ma and a highly unradiogenic  $(^{187}\text{Os}/^{188}\text{Os})_{\text{initial}}$  ratio of  $0.225 \pm 0.153$  (Fig. 5.5A). This would make the Urucum IF significantly younger than previously thought. Back-calculating the  $(^{187}\text{Os}/^{188}\text{Os})_{\text{initial}}$  ratios of each individual sample shows that they are highly divergent, with many samples having negative ratios. Negative ratios are an indication that the system was not isotopically closed or has been affected by syn- and post-depositional disturbances in some way.

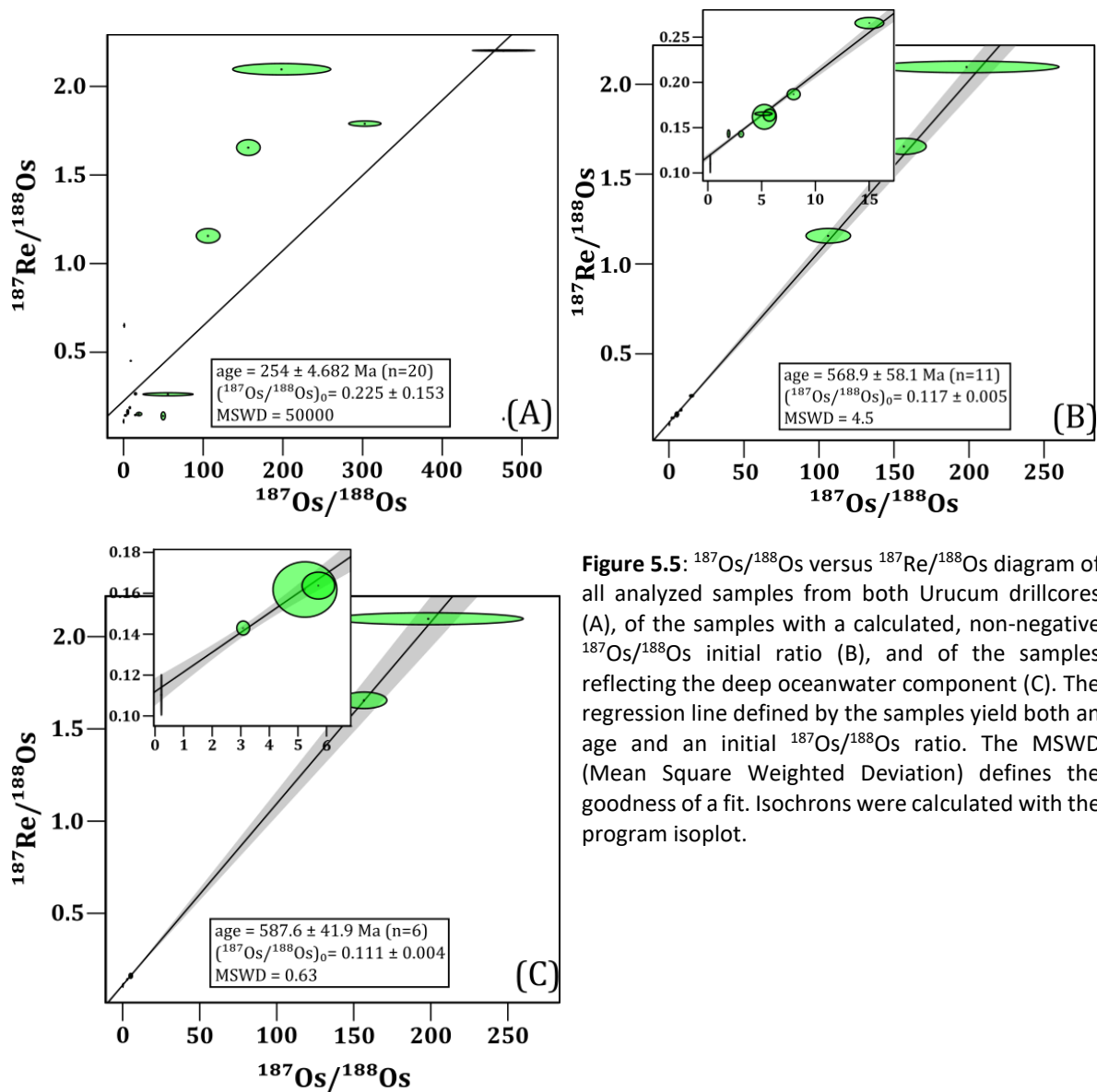


**Figure 5.5:**  $^{187}\text{Os}/^{188}\text{Os}$  versus  $^{187}\text{Re}/^{188}\text{Os}$  diagram of all analyzed samples from both Urucum drillcores (A), of the samples with a calculated, non-negative  $^{187}\text{Os}/^{188}\text{Os}$  initial ratio (B), and of the samples reflecting the deep oceanwater component (C). The regression line defined by the samples yield both an age and an initial  $^{187}\text{Os}/^{188}\text{Os}$  ratio. The MSWD (Mean Square Weighted Deviation) defines the goodness of a fit. Isochrons were calculated with the program isoplot.

11 samples (UR51\_10, UR51\_14, UR51\_15, UR51\_16, UR51\_26, UR51\_35, UR51\_40, UR51\_55, UR51\_70, UR62\_17 and UR62\_30) of our dataset show similar and reasonable initial  $^{187}\text{Os}/^{188}\text{Os}$  ratios, grouping around a ratio of  $(^{187}\text{Os}/^{188}\text{Os})_{\text{initial}} \approx 0.116$ . Using only these 11 samples we can define a more precise regression line that corresponds to an age of  $568.9 \pm 58.1$  Ma (MSWD = 4.5) and a  $(^{187}\text{Os}/^{188}\text{Os})_{\text{initial}}$  ratio of  $0.117 \pm 0.005$ . Samples UR51\_10, UR51\_35, UR51\_40, UR51\_55, and UR51\_70 are considered to reflect the clastic component of the continental flux (see Chapter 5.2). We therefore exclude these samples to refine our isochrone to better reflect the hydrogenous Os component. The final, best fit-isochron with the remaining 6 samples yields a regression line that corresponds to an age of  $587.6 \pm 41.9$  Ma (MSWD = 0.63) and an  $(^{187}\text{Os}/^{188}\text{Os})_{\text{initial}}$  ratio of  $0.111 \pm 0.004$ .

The age defined by the best-fit isochron of the Urucum IF and Mn-F samples is in good agreement with previously published results for the Santa Cruz deposit, particular the  $^{40}\text{Ar}/^{39}\text{Ar}$  ages reported by Piacentini et al. (2013). While their ages of  $587 \pm 7$  Ma and  $547 \pm 3$  Ma for

Mn-horizon1-minerals cryptomelane and braunite were interpreted as diagenetic age and recrystallization age, respectively, they argued for a deposition age older than 590 Ma. Our age of  $587.6 \pm 41.9$  Ma falls in a similar range, but the Jacadigo Group could still be related to the Gaskiers glaciation event, but it is far more likely that the Jacadigo Group is older than the Gaskiers glaciation. Piacentini et al. (2013) argued that the present mineralogy and isotopic composition do not reflect the depositional environment. Their samples were taken from the Mn-rich horizon Mn1, while samples from which the age presented in this work is derived were taken from iron-rich horizons and from Mn-rich horizon Mn2. If the presented samples do not represent depositional conditions, as claimed by Piacentini et al. (2013), the here represented isochrone age would reveal a minimum depositional age, still making the Jacadigo Group older than the Gaskiers glaciation. Recently, Williams and Schmidt (2020) dated the Acraman impact structure, South Australia, one of the largest known impact structures, to  $\sim 590$  Ma. This would put the deposition of the Urucum in the timeframe of a significant impact event in the Neoproterozoic. The effects of an impact as large as Acraman should be notable in the geological record. As discussed above, there is no indication for a meteoritic component in the Urucum BIF. The deposition of the Urucum IF must have preceded the impact event, as there are no elevated HSE concentrations in the Urucum samples. Hence, a relation of the Urucum deposition to the Marinoan glaciation is more likely than to the later Gaskiers glaciation.

### **Sources of highly siderophile elements for the Urucum IF**

The  $(^{187}\text{Os}/^{188}\text{Os})_{\text{initial}}$  ratio of  $0.111 \pm 0.004$  derived from the intercept of the regression line represents an estimate of the seawater composition during the deposition of the Urucum IF. This value is extremely unradiogenic and in the range of the  $^{187}\text{Os}/^{188}\text{Os}$  composition of chondrites ( $\sim 0.12$ ; Horan et al. 2003) and the primitive upper mantle ( $\sim 0.13$ ; Meisel et al. 2001). As discussed above, there is no indication for a meteoritic component in the Santa Cruz deposit. Because the input of cosmic dust is considered constant during time, the unradiogenic  $(^{187}\text{Os}/^{188}\text{Os})_{\text{initial}}$  ratio of the Urucum samples would support enhanced influence of mantle-derived sources on the Neoproterozoic seawater, while continental input was weakened. A strong mantle signature for the Urucum IF is supported by the findings of Huang et al. (2021), who concluded that over 50% of Fe in the Urucum BIF was sourced by upwelling, Fe(II)-rich bottom seawater, derived from low-temperature hydrothermal vent systems. Similar low initial  $^{187}\text{Os}/^{188}\text{Os}$  ratios have been reported on the Temagami BIF by Schulz et al. (2021), who postulated a  $^{187}\text{Os}/^{188}\text{Os}$  seawater signature between 0.11 and 0.22 for the Neoproterozoic Temagami BIF.

However, Viehmann et al. (2016) found no indication for a significant hydrothermal component in the REY budget of the ambient seawater. Additionally, the Os isotopic seawater curve shows

a prominent excursion to highly radiogenic  $^{187}\text{Os}/^{188}\text{Os}$  ratios in the late Neoproterozoic to Cambrian, indicating a strong influence of crustal sources (Fig.5.6). The derived age would put the deposition of the Urucum IF in the time frame of this excursion, showing a mantle-like signature. Therefore, one has to ask how such contradictory observations can exist simultaneously?

One possible explanation could be that the Urucum samples have an Os isotopic composition of an isolated basin rather than the Os isotopic composition of global seawater. Deposition of IFs require the presence of anoxic conditions in the water, popular deposition models for the Urucum IF therefore generally depict the deposition basin as relatively small and partially or fully isolated from the larger oceans (e.g., Urban et al. 1992; Angerer et al. 2016; Viehmann et al. 2016; Huang et al. 2021). The chemical composition of the basin water would therefore differ from the global oceans, as the smaller water body would be more prone to local influences. One such influence would have low-temperature (<150°C) hydrothermal vent fluids, which were introduced to the basin due to the active graben tectonics (e.g., Walde and Hagemann 2007). The influence of such vent fluids on the deposition of BIFs has already seen support in previous publications (e.g., Basta et al. 2011; Angerer et al. 2016), and it would further highlight the significance of hydrothermal activity as prerequisite for the deposition of banded iron formations. Based on the previous findings concerning the Urucum BIF this seems to be the most plausible explanation.

Another possibility for the observed discrepancies in initial  $^{187}\text{Os}/^{188}\text{Os}$  values is that the Urucum samples and the previous published data simply show different aspects of the Os isotopic seawater composition. The established Os isotopic seawater curve for the Neoproterozoic is based almost exclusively on data from organic rich mudrocks (ORM). It is assumed that these rocks derive the main volume of their Os budget from seawater and are, therefore, of particular interest for geochemical archives for the Os isotopic seawater curve through time (e.g., Peucker-Ehrenbrink and Ravizza 2020). However, concerns have been raised that the measured  $^{187}\text{Os}/^{188}\text{Os}$  ratios of ORM are the result from admixture of seawater-derived Os and detrital-derived Os (e.g., Cohen et al. 1999; Roney et al. 2011). It is, therefore, possible that ORMs, like BIFs, do not reflect global but rather local water conditions from which they precipitated. While the Os concentrations and isotopic composition of riverine runoff depend on the terrain which they drain, the residence time of Os in the oceans should be long enough that it is well mixed and its isotopic composition stable. While not impossible, this explanation is less likely.

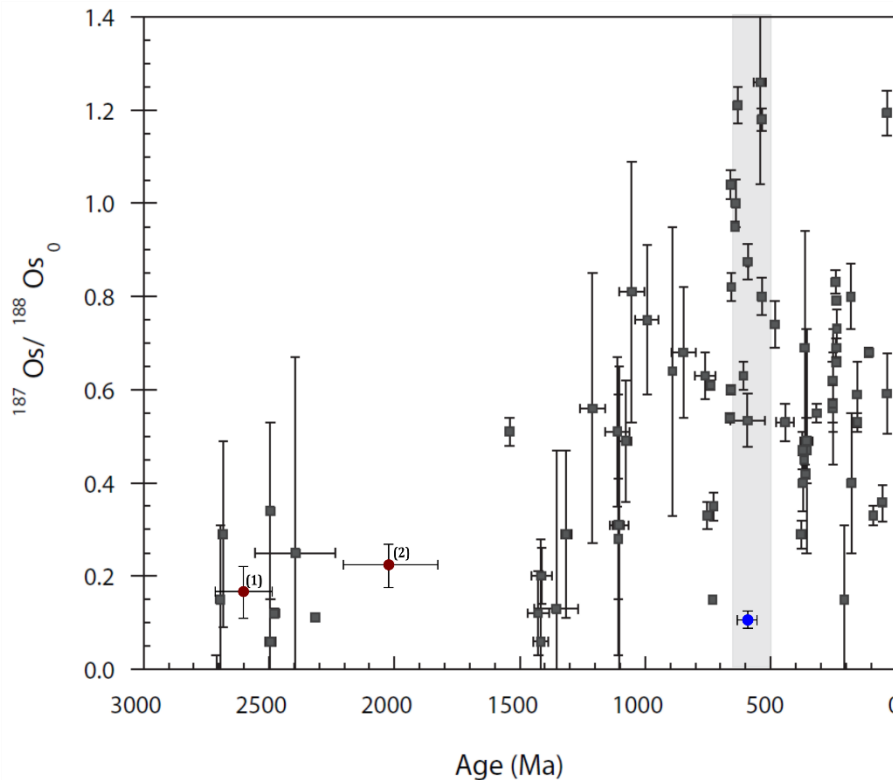


**Figure 5.6:** Initial  $^{187}\text{Os}/^{188}\text{Os}$  data and Re-Os isochron ages as seen in chapter (1.3.2.1), with the best-fit isochron age of the Urucum BIF added in blue. Note that the unradiogenic initial  $^{187}\text{Os}/^{188}\text{Os}$  ratio of the Urucum BIF falls into the proposed interval of radiogenic  $^{187}\text{Os}/^{188}\text{Os}$  ratios at the end of the Neoproterozoic.

Lastly, it is possible that the prominent excursion to highly radiogenic  $^{187}\text{Os}/^{188}\text{Os}$  values is not a singular event. The hypotheses of the radiogenic  $^{187}\text{Os}/^{188}\text{Os}$  interval is based on a handful of datasets with an age spacing larger than the average marine residence time of Os (Peucker-Ehrenbrink and Ravizza 2020). The available data are too sparse to make satisfying statements about long-term trends in the pre-Phanerozoic marine Os isotope record. The postulated excursion may, therefore, be a cluster of high frequency  $^{187}\text{Os}/^{188}\text{Os}$  variations, caused by the repeated glaciation and deglaciation phases during the major glaciation events. While the presented Urucum dataset is not enough to resolve this issue, it further highlights the need for more high-resolution datasets in the Precambrian record to make meaningful statements on long term trend in the marine  $^{187}\text{Os}/^{188}\text{Os}$  isotopic record through time.

To summarize, the final isochrone plot gives a precise age of  $587.6 \pm 41.9$  Ma and an initial  $^{187}\text{Os}/^{188}\text{Os}$  ratio of  $0.111 \pm 0.004$ . This age is in good agreement with previous published radiogenic ages, particularly the Ar/Ar ages of Piacentini et al. (2013). While age uncertainties could place the deposition of the Urucum IF into the timeframe of the Gaskiers glaciation (~580 Ma), combined evidence of this study with previous publications makes a relation of the Urucum IF with the Marinoan glaciation (~650-635 Ma) more likely. This is based on a deposition age older than 590 Ma (e.g., see Piacentini et al. 2013) and on a deposition model

in a glaciogenic setting. Further, the presented initial  $^{187}\text{Os}/^{188}\text{Os}$  ratio of  $0.111 \pm 0.004$  is extremely unradiogenic and near the  $^{187}\text{Os}/^{188}\text{Os}$  mantle evolution curve. Such an unradiogenic value indicates a strong influence of mantle-derived sources on the Neoproterozoic seawater geochemistry, one possibility being low-temperature (<150°C) hydrothermal vent fluids (e.g., Angerer et al. 2016; Huang et al. 2021). While previous studies on the Urucum IF support a strong influence of mantle-derived sources, the established Os isotopic seawater evolution curve for the Neoproterozoic, derived from data of ORM, shows a prominent excursion to high  $^{187}\text{Os}/^{188}\text{Os}$  values (up to 1.4). While it is possible the ORM and IF samples show different fractions of the seawater geochemistry, it is considered more likely that the initial  $^{187}\text{Os}/^{188}\text{Os}$  ratio of the Urucum samples depicts the Os isotopic composition of the semi- to fully closed Urucum deposition basin. Again, this is in good agreement with previous studies on the depositional environment of the Urucum IF.

## 6 Conclusions

Based on the highly siderophile elements and Re-Os isotope data, the following conclusions are drawn for the Urucum IF and Mn-F formation.

1. Urucum samples show crustal to supracrustal concentrations of highly siderophile elements. The abundance of HSE (Re, Os, Ir and Pt) and the  $^{187}\text{Os}/^{188}\text{Os}$  ratios show no systematic variation between the IF and Mn-F samples. Concentrations are highly variable within the stratigraphy of the drill cores and can cover three orders of magnitude. Stratigraphically adjacent samples can show extremely diverse concentrations and ratios.
2. Interelemental ratios cover average values from crustal rocks, mantle rocks and chondrites. Ratios seem to follow a systematic trend, with Ir concentrations and Re/Os ratios becoming more variable with increasing Pt concentration. The ratios are significantly higher than those of komatiites and orders similar to those found in modern seawater. Additionally, ratios of several samples overlap with typical anoxic marine sediments, supporting the interpretation of anoxic conditions in the Urucum basin. We found no indication for a meteoritic component in the Urucum IF.
3. Urucum samples are proposed to display a mixture of components of the Urucum basin water. Samples with high concentrations of Re and Os have low concentrations of  $\text{Al}_2\text{O}_3$  and Sr. These samples represent an open ocean deep water component that provided the basin with HSE and Fe. Samples with lower

concentrations of Re and Os show variable contents of Al<sub>2</sub>O<sub>3</sub> and Sr. These samples are representative of a continental flux, a mixture of basin induced riverwater and continental aluminosilicate. Samples with low concentrations of Al<sub>2</sub>O<sub>3</sub> and Sr are interpreted to represent the riverwater component of the flux, while samples with high amounts of Al<sub>2</sub>O<sub>3</sub> and Sr these elements reflect the detrital component, for example aluminosilicate concretion. the riverwater component.

4. A regression line defined by the open ocean deep water samples in the <sup>187</sup>Os/<sup>188</sup>Os vs <sup>187</sup>Re/<sup>188</sup>Os plot yield an age of 587.6 ± 41.9 Ma (MSWD = 0.63). It is in good agreement with previously published results of Piacentini et al. (2013). While a relation of the deposition of the Urucum IF with the Gaskier glaciation cannot be excluded, we perceive a relation to the Marinoan glaciation as more likely.
5. The (<sup>187</sup>Os/<sup>188</sup>Os)<sub>initial</sub> ratio of 0.111 ± 0.004 provided by the <sup>187</sup>Os/<sup>188</sup>Os vs <sup>187</sup>Re/<sup>188</sup>Os plot is extremely unradiogenic. This ratio indicated enhanced input of mantle-derived sources while continental input was weakened. These findings are in agreement with the Urucum IF data of Huang et al. (2021) and the Temagami BIF data of Schulz et al (2021). However, the established Os isotopic seawater evolution curve for the Neoproterozoic, shows a prominent excursion to high <sup>187</sup>Os/<sup>188</sup>Os values (up to 1.4). We consider these discrepancies due to the initial <sup>187</sup>Os/<sup>188</sup>Os ratio of the Urucum samples depicting the Os isotopic composition of the semi to fully closed Urucum deposition basin, not an open ocean. Again, this is in agreement with previous studies on the deposition environment of the Urucum IF.

## 7 References

- Albut G, Babechuk MG, Kleinhanns IC, Bengler M, Beukes NJ, Steinhilber B, Smith AJB, Kruger SJ, and Schoenberg R (2018).** Modern rather than Mesoarchaeon oxidative weathering responsible for the heavy stable Cr isotopic signatures of the 2.95 Ga old Ijzermijn iron formation (South Africa). *Geochimica et Cosmochimica Acta* 228, pp. 157–189.
- Alexander BW, Bau M, Andersson P, and Dulski P (2008).** Continentally-derived solutes in shallow Archean seawater: Rare earth element and Nd isotope evidence in iron formation from the 2.9Ga Pongola Supergroup, South Africa. *Geochimica et Cosmochimica Acta* 72 (2), pp. 378-394. ISSN 0016-7037, doi: <https://doi.org/10.1016/j.gca.2007.10.028>
- Alkmim FF and Martins-Neto MA (2012).** Proterozoic first-order sedimentary sequences of the São Francisco craton, eastern Brazil. *Marine and Petroleum Geology* 33, pp. 127–139.
- Allen PA and Etienne JA (2008).** Sedimentary challenge to Snowball Earth. *Nature Geoscience* 1, pp. 817-825. doi: <https://doi.org/10.1038/ngeo355>
- Alvarenga CJS de, and Trompette R (1993).** Brasiliano tectonic of the Paraguay Belt: the structural development of the Cuiabá Region. *Revista Brasileira de Geociências* 23, pp. 18–30.
- Alvarenga, CJS de, Boggiani PC, Babinski M, Dardenne MA, Figueiredo MF, Dantas EL, Uhlein A, Santos RV, Sila AN, and Trompette R (2011).** Chapter 45: Glacially influenced sedimentation of the Puga Formation, Cuiabá Group and Jacadigo Group, and associated carbonates of the Araras and Corumbá groups,

- Paraguay belt, central Brazil. In: Arnaud E, Halverson GP, and Shields-Zhou G (eds.). *The Geological Record of Neoproterozoic Glaciations*. Geological Society, London, Memoirs 36, pp. 487–497. doi: <http://dx.doi.org/10.1144/M36.45>
- Anbar AD, Creaser RA, Papanastassiou DA, and Wasserburg GJ (1992)**. Rhenium in seawater: Confirmation of generally conservative behavior, *Geochimica et Cosmochimica Acta* 56 (11), pp. 4099–4103, ISSN 0016-7037, [https://doi.org/10.1016/0016-7037\(92\)90021-A](https://doi.org/10.1016/0016-7037(92)90021-A)
- Andersen MB, Romaniello S, Vance D, Little SH, Herdman R, and Lyons TW (2014)**. A modern framework for the interpretation of <sup>238</sup>U/<sup>235</sup>U in studies of ancient ocean redox. *Earth and Planetary Science Letters* 400, pp. 184–194.
- Angerer T, Hagemann SG, and Walde DHG (2021)**. Diagenetic and supergene ore forming processes in the iron formation of the Neoproterozoic Jacadigo Group, Corumbá, Brazil. *Journal of South American Earth Sciences* 105, 102902. ISSN 0895-9811, doi: <https://doi.org/10.1016/j.jsames.2020.102902>
- Angerer T, Hagemann SG, Walde DH, Halverson GP, and Boyce AJ (2016)**. Multiplemetal sources in the glaciomarine facies of the Neoproterozoic Jacadigo iron formation in the “Santa Cruz deposit”, Corumbá, Brazil. *Precambrian Research* 275, 369–393. doi: <https://doi.org/10.1016/j.precamres.2016.01.002>
- Araújo HJT, Santos Neto A, Trindade CAH, Pinto JCA, Montalvão RMG, Dourado TDC, Palmeira RCB, and Tassinari CCG (1982)**. Folha SF.21—Campo Grande: geologia, geomorfologia, pedologia, vegetação e uso potencial da terra. In: *Levantamento de Recursos Naturais: Rio de Janeiro, DNPM, Projeto Radam Brasil* 28, p. 416.
- Babinski M, Boggiani PC, Fanning CM, Fairchild TR, Simon CM, and Sial AN (2008)**. U–PB SHRIMP geochronology and isotope chemostratigraphy (C, O, Sr) of the Tamengo Formation, Southern Paraguay Belt, Brazil. VI. *South American Symposium on Isotope Geology, Book of Abstracts, San Carlos de Bariloche*, p.160.
- Babinski M, Boggiani PC, Trindade RIF, and Fanning CM (2013)**. Detrital zircon ages and geochronological constraints on the Neoproterozoic Puga diamictites and associated BIFs in the southern Paraguay Belt, Brazil. *Gondwana Research* 23 (3), pp. 988–997. ISSN 1342-937X, doi: <https://doi.org/10.1016/j.gr.2012.06.011>
- Baldwin GJ, Turner EC, and Kamber BS (2012)**. A new depositional model for glaciogenic Neoproterozoic iron formation: insights from the chemostratigraphy and basin configuration of the Rapitan iron formation. *Canadian Journal of Earth Sciences* 49 (2), pp. 455–476. doi: <https://doi.org/10.1139/e11-066>
- Barghoorn ES, and Tyler SA (1965)**. Microorganisms from Gunflint Chert. *Science* 147: 563–577. doi: 10.1126/science.147.3658.563
- Barley ME, Bekker A, and Krapez B (2005)**. Late Archean to early Paleoproterozoic global tectonics, environmental change and the rise of atmospheric oxygen. *Earth and Planetary Science Letters* 238, pp. 156–171. doi: 10.1016/j.epsl.2005.06.062
- Barling J, and Anbar AD (2004)**. Molybdenum isotope fractionation during adsorption by manganese oxides. *Earth and Planetary Science Letters* 217 (3–4), pp. 315–329.
- Barrett TJ, Wares RP, and Fox JS (1988)**. Two-stage hydrothermal formation of a Lower Proterozoic sediment-hosted massive sulfide deposit, northern Labrador Trough, Quebec. *Canadian Mineralogist* 26, pp. 871–888.
- Basta FF, Maurice AE, Fontboté L, and Favarger P-Y (2011)**. Petrology and geochemistry of the banded iron formation (BIF) of Wadi Karim and Um Anab, Eastern Desert, Egypt: Implications for the origin of Neoproterozoic BIF. *Precambrian Research* 187, pp. 277–292.
- Bau M (1993)**. Effects of syn- and post-depositional processes on the rare-earth element distribution in Precambrian iron-formations. *European Journal of Mineralogy* 5 (2), pp. 257–267.
- Bau M (1996)**. Controls on the fractionation of isovalent trace elements in magmatic and aqueous systems: evidence from Y/Ho, Zr/Hf, and lanthanide tetrad effect. *Contributions to Mineralogy and Petrology*. 123, pp. 323–333.
- Bau M and Dulski P (1999)**. Comparing yttrium and rare earths in hydrothermal fluids from the Mid-Atlantic Ridge: implications for Y and REE behavior during near-vent mixing and for the Y/Ho ratio of Proterozoic seawater. *Chemical Geology* 155, pp. 77–90. doi: [https://doi.org/10.1016/S0009-2541\(98\)00142-9](https://doi.org/10.1016/S0009-2541(98)00142-9)
- Bau M, and Dulski P (1996)**. Distribution of yttrium and rare-earth elements in the Penge and Kuruman iron-formations, Transvaal Supergroup, South Africa. *Precambrian Research* 79, pp.37–55.
- Bau M, and Koschinsky A (2009)**. Oxidative scavenging of cerium on hydrous Fe oxide: Evidence from the distribution of rare earth elements and yttrium between Fe oxides and Mn oxides in hydrogenetic ferromanganese crusts. *Geochemical Journal* 43 (1), pp. 37–47. Doi:10.2343/geochemj.1.0005.

- Bau M, Frei R, Garbe-Schönberg D, and Viehmann S (2022).** High-resolution Ge-Si-Fe, Cr isotope and Th-U data for the Neoproterozoic Temagami BIF, Canada, suggest primary origin of BIF bands and oxidative terrestrial weathering 2.7 Ga ago. *Earth and Planetary Science Letters* 589, 117579. ISSN 0012-821X, doi: <https://doi.org/10.1016/j.epsl.2022.117579>.
- Beal EJ, House CH, and Orphan VJ (2009).** Manganese- and iron-dependent marine methane oxidation. *Science* 325, pp. 184–187.
- Becker H, Horan MF, Walker RJ, S. Gao S, Lorand J-P, and Rudnick RL (2006).** Highly siderophile element composition of the Earth's primitive upper mantle: Constraints from new data on peridotite massifs and xenoliths. *Geochimica et Cosmochimica Acta* 70 (17), pp. 4528-4550. ISSN 0016-7037, doi: <https://doi.org/10.1016/j.gca.2006.06.004>.
- Bekker A (2011).** Huronian glaciation. In: Gargaud M (ed.) *Encyclopedia of Astrobiology*, pp. 768–772. Berlin: Springer.
- Bekker A, and Kaufman AJ (2007).** Oxidative forcing of global climate change: A biogeochemical record across the oldest Paleoproterozoic ice age in North America. *Earth and Planetary Science Letters* 258(3–4), pp. 486–499.
- Bekker A, and Kovalick A. (2021).** Ironstones and iron formations. In: Alderton D and Elias SA (eds.) *Encyclopedia of Geology* (2nd ed.), pp. 914–921, Oxford: Academic Press.
- Bekker A, Hollan H, Wang PL, Rumble D 3<sup>rd</sup>, Stein HJ, Hannah JL, Coetzee LL, and Beukes NJ (2004).** Dating the rise of atmospheric oxygen. *Nature* 427, pp. 117–120, doi: <https://doi.org/10.1038/nature02260>
- Bekker A, Planavsky N, Rasmussen B, Krapez B, Hofmann A, Slack J, Rouxel O, and Konhauser KO (2014).** Iron Formations: Their Origins and Implications for Ancient Seawater Chemistry. In: Holland H and Turekian K (ed), *Treatise on Geochemistry*, Vol. 9, Elsevier, Netherlands, pp. 561-628, ISBN: 978-0-08-098300-4, doi: 10.1016/B978-0-08-095975-7.00719-1.
- Bekker A, Slack JF, Planavsky N, Krapez B, Hofmann A, Konhauser K, and Rouxel O (2010).** Iron Formation: The Sedimentary Product of a Complex Interplay among Mantle, Tectonic, Oceanic, and Biospheric Processes, *Economic Geology* 105, pp. 467-508, doi: <http://dx.doi.org/10.2113/gsecongeo.105.3.467>.
- Beukes NJ, and Gutzmer J (2008).** Origin and paleoenvironmental significance of major iron formations at the Archean-Paleoproterozoic boundary. *Reviews in Economic Geology* 15, pp. 5–47. doi: <https://doi.org/10.5382/Rev.15.01>
- Biondi JC, and Lopez M (2017).** Urucum Neoproterozoic–Cambrian manganese deposits (MS, Brazil): Biogenic participation in the ore genesis, geology, geochemistry, and depositional environment, *Ore Geology Reviews* 91, pp. 335-386. ISSN 0169-1368, doi: <https://doi.org/10.1016/j.oregeorev.2017.09.018>
- Biondi JC, Polgári M, Gyollai I, Fintor K, Kovács I, Fekete J, and Mojszsis SJ (2020).** Biogenesis of the Neoproterozoic kromyidilite manganese ores from Urucum (Brazil) – A new manganese ore type. *Precambrian Research* 340, 105624. ISSN 0301-9268, doi: <https://doi.org/10.1016/j.precamres.2020.105624>
- Birck JL, Barman MR, and Capmas F (1997).** Re-Os Isotopic Measurements at the Femtomole Level in Natural Samples. *Geostandards Newsletter* 21, pp. 19-27. doi: <https://doi.org/10.1111/j.1751-908X.1997.tb00528.x>
- Bjerrum CJ, and Canfield DE (2002).** Ocean productivity before about 1.9 Ga ago limited by phosphorus adsorption onto iron oxides. *Nature* 417, pp.159–162.
- Blanco G, Rajesh HM, Gaucher C, Germs GJB, and Chemale Jr. F (2009),** Provenance of the Arroyo del Soldado Group (Ediacaran to Cambrian, Uruguay): Implications for the paleogeographic evolution of southwestern Gondwana. *Precambrian Research* 171, pp. 57–73.
- Bodisieltsch B, Koeberl C, Master S, and Reimold WU (2005).** Estimating duration and intensity of Neoproterozoic Snowball glaciations from iridium anomaly. *Science* 308, pp. 239-242
- Boggiani PC, Gaucher C, Sial AN, Babinski M, Simon CM, Riccomini C, Ferreira VP, and Fairchild TR (2010).** Chemostratigraphy of the Tamengo Formation (Corumbá Group, Brazil): A contribution to the calibration of the Ediacaran carbon-isotope curve. *Precambrian Research* 182 (4), pp. 382-401. ISSN 0301-9268, doi: <https://doi.org/10.1016/j.precamres.2010.06.003>
- Bolhar R, Kamber BS, Moorbath S, Fedo CM, and Whitehouse MJ (2004).** Characterisation of early Archaean chemical sediments by trace element signatures. *Earth and Planetary Science Letters* 222, pp. 43–60. doi: <https://doi.org/10.1016/j.epsl.2004.02.016>
- Brandon AD, Humayun M, Puchtel IS, Leya I, and Zolensky M (2005)** Geochemistry: osmium isotope evidence for an s-process carrier in primitive chondrites. *Science* 309, pp.1233–1236.
- Brenan JM, Bennett NR, and Zajacz Z (2016).** Experimental results on fractionation of the highly siderophile elements (HSE) at variable pressures and temperatures during planetary and magmatic differentiation. *Reviews in Mineralogy and Geochemistry* 81, pp. 1–87

- Brocks JJ (2011).** Millimeter-scale concentration gradients of hydrocarbons in Archean shales: Live-oil escape or fingerprint of contamination? *Geochimica et Cosmochimica Acta* 75 (11), pp. 3196-3213, ISSN 0016-7037. doi: <https://doi.org/10.1016/j.gca.2011.03.014>
- Burkhalter RM (1995).** Ooidal ironstones and ferruginous microbialites: Origin and relation to sequence stratigraphy (Aalenian and Bajocian, Swiss Jura Mountains). *Sedimentology* 42, pp. 57–74.
- Cairns-Smith AG (1978).** Precambrian solution photochemistry, inverse segregation, and banded iron formations. *Nature* 276, pp. 807–808.
- Canfield DE, Poulton SW, Knoll AH, Narbonne GM, Goldberg GRT, and Strauss H (2008).** Ferruginous conditions dominated later Neoproterozoic deepwater chemistry. *Science* 321 (5891), pp949–952.
- Cannon WF, LaBerge GL, Klasner JS, and Schulz KJ (2008).** The Gogebic Iron Range – a sample of the northern margin of the Penokean fold and thrust belt. U.S. *Geological Survey Professional Paper* 1730, pp. 1–44.
- Cannon WF, Schulz KJ, Horton Jr. JW, and Kring DA (2010).** The Sudbury impact layer in the Paleoproterozoic iron ranges of northern Michigan, USA. *Geological Society of America Bulletin* 122, pp. 50–75.
- Casquet C, Rapela CW, Pankhurst RJ, Baldo EG, Galindo C, Fanning CM, Dahlquist JA, and Saavedra J (2012).** A history of Proterozoic terranes in southern South America: From Rodinia to Gondwana. *Geoscience Frontiers* 3 (2), pp. 137-145. ISSN 1674-9871, doi: <https://doi.org/10.1016/j.gsf.2011.11.004>
- Chen K, Walker RJ, Rudnick RL, Gao S, Gaschnig RM, Puchtel IS, Ming Tang M, and Hu Z-C (2016).** Platinum-group element abundances and Re–Os isotopic systematics of the upper continental crust through time: Evidence from glacial diamictites. *Geochimica et Cosmochimica Acta* 191, pp. 1-16. ISSN 0016-7037, doi: <https://doi.org/10.1016/j.gca.2016.07.004>.
- Chou C-L (1978).** Fractionation of siderophile elements in the Earth's upper mantle. *Proceedings of the 9<sup>th</sup> Lunar and Planetary Science Conference*, pp. 219–230
- Cloud PE (1965).** Significance of Gunflint (Precambrian) microflora. *Science* 148, pp. 27–35. doi: 10.1126/science.148.3666.27
- Cloud PE (1973).** Paleocological Significance of the Banded Iron-Formation. *Economic Geology* 68 (7), pp. 1135–1143. doi: <https://doi.org/10.2113/gsecongeo.68.7.1135>
- Cohen AS and Waters FG (1996).** Separation of osmium from geological materials by solvent extraction for analysis by thermal ionisation mass spectrometry. *Analytica Chimica Acta* 332 (2-3), pp. 269–275.
- Cohen AS, Coe AL, Bartlett JM, and Hawkesworth CJ (1999).** Precise Re–Os ages of organic-rich mudrocks and the Os isotope composition of Jurassic seawater, *Earth and Planetary Science Letters* 167 (3–4), pp. 159–173, ISSN 0012-821X. doi: [https://doi.org/10.1016/S0012-821X\(99\)00026-6](https://doi.org/10.1016/S0012-821X(99)00026-6)
- Colodner D, Sachs J, Ravizza G, Turekian KK, Edmond J, and Boyle E (1993).** The geochemical cycle of rhenium: a reconnaissance. *Earth and Planetary Science Letters* 117 (1–2), pp. 205-221, ISSN 0012-821X, doi: [https://doi.org/10.1016/0012-821X\(93\)90127-U](https://doi.org/10.1016/0012-821X(93)90127-U).
- Cordani UG, Pimentel MM, Araújo CEG, and Fuck RA (2013).** The significance of the Transbrasiliano-Kandi tectonic corridor for the amalgamation of West Gondwana. *Brazilian Journal of Geology* 43 (3), pp. 583–597. doi: <http://dx.doi.org/10.5327/Z2317-48892013000300012>
- Cordani UG, Sato K, Teixeira W, Tassinari CCG, and Basei MAS (2000).** Crustal evolution of the South American platform. In: Cordani UG, Milani EJ, Thomaz-Filho A, and Campos DA (eds.). *Tectonic evolution of South America: Rio de Janeiro, Brazil, 31st International Geological Congress*, p. 19–40.
- Cordani UG, Teixeira W, D'Agrella-Filho MS, and Trindade RI (2009).** The position of the Amazonian Craton in supercontinents. *Gondwana Research* 15 (3–4), pp. 396-407. ISSN 1342-937X, doi: <https://doi.org/10.1016/j.gr.2008.12.005>
- Cordani UG, Teixeira W, Tassinari CCG, Coutinho JMV, and Ruiz AS (2010).** The Rio Apa Craton in Mato Grosso do Sul (Brazil) and northern Paraguay: Geochronological evolution, correlations and tectonic implications for Rodinia and Gondwana. *American Journal of Science* 310 (9) pp. 981-1023. doi: <https://doi.org/10.2475/09.2010.09>
- Cordeiro PF de O, Oliveira CG, Della Giustina MES, Dantas EL, and Santos RV (2014).** The Paleoproterozoic Campinorte Arc: tectonic evolution of a Central Brazil pre-Columbia orogeny. *Precambrian Research* 251, 49–61. doi: <http://dx.doi.org/10.1016/j.precamres.2014.06.002>
- Costa ML, Fernandez OJC, Ribeiro PA, Silva NC, and Poellmann H (2005).** Contribuições mineralógicas e geoquímicas sobre a origem do minério de manganês do Morro do Urucum (Corumbá, Brasil): *Simpósio Brasileiro de Metalogenia, 1<sup>th</sup>, Gramado (RS, Brasil), Abstracts, CD-ROM*.
- Cox GM, Halverson GP, Minarik WG, Heron DP, Macdonald FA, Bellefroid EJ, and Strauss JV (2013).** Neoproterozoic iron formation: An evaluation of its temporal, environmental and tectonic significance, *Chemical Geology* 362, pp. 232-249, ISSN 0009-2541. doi: <https://doi.org/10.1016/j.chemgeo.2013.08.002>

- Cox GM, Halverson GP, Poirier A, Le Heron D, Strauss JV, and Stevenson R (2016).** A model for Cryogenian iron formation. *Earth and Planetary Science Letters* 433, pp.280-292. ISSN 0012-821X, doi: <https://doi.org/10.1016/j.epsl.2015.11.003>
- Creaser RA, Papanastassiou DA, and Wasserburg GJ (1991).** Negative thermal ion mass spectrometry of osmium, rhenium and iridium. *Geochimica et Cosmochimica Acta* 55 (1), pp.397-401. ISSN 0016-7037, doi: [https://doi.org/10.1016/0016-7037\(91\)90427-7](https://doi.org/10.1016/0016-7037(91)90427-7).
- Crowe SA, Døssing LN, Beukes NJ, Bau M, Kruger SJ, Frei R, and Canfield DE (2013).** Atmospheric oxygenation three billion years ago. *Nature* 501(7468), pp. 535–538.
- Crowe SA, Katsev S, Leslie K, Sturm A, Magen C, Nomosatryo S, Pack MA, Kessler JD, Reeburgh WS, Roberts JA, González L, Douglas Haffner G, Mucci A, Sundby B, and Fowle DA (2011).** The methane cycle in ferruginous Lake Matano. *Geobiology* 9, pp. 61–78.
- Danielson A, Möller P, and Dulski P(1992).** The europium anomalies in banded iron formations and the thermal history of the oceanic crust. *Chemical Geology* 97 (1–2), pp. 89-100. ISSN 0009-2541, doi: [https://doi.org/10.1016/0009-2541\(92\)90137-T](https://doi.org/10.1016/0009-2541(92)90137-T).
- Dauphas N, John SG, and Rouxel O (2017).** Iron isotope systematics. *Reviews in Mineralogy and Geochemistry* 82(1), pp. 415–510.
- Day JMD (2013).** Hotspot volcanism and highly siderophile elements. *Chemical Geology* 341, pp. 50-74. ISSN 0009-2541, doi: <https://doi.org/10.1016/j.chemgeo.2012.12.010>
- Day JMD, Brandon AD, and Walker RJ (2016).** Highly Siderophile Elements in Earth, Mars, the Moon, and Asteroids. *Reviews in Mineralogy and Geochemistry* 81 (1), pp. 161–238. doi: <https://doi.org/10.2138/rmg.2016.81.04>
- de Almeida FFM (1945).** Boletim da Divisão de Geologia e Mineralogia, Departamento Nacional de Produção Mineral, DNPM. *Geologia do sudoeste mato-grossense* 116, pp. 1–118.
- de Almeida FFM (1946).** Origem dos minérios de ferro e manganês de Urucum (Corumbá, Estado do Mato Grosso): Boletim da Divisão de Geologia e Mineralogia do Departamento Nacional da Produção. *Mineral (DNPM, Rio de Janeiro)* 119, p. 58.
- de Baar HJW, and de Jong JTM (2001).** Distributions, sources and sinks of iron in seawater. In: Turner, D., Hunter, K.A. (Eds.), *The Biogeochemistry of Iron in Seawater*, pp. 123–253. John Wiley & Sons, New York.
- de Souza FR, Nalini HA, and de Abreu AT (2019).** In-situ LA-ICP-MS and EMP trace element analyses of hematite: Insight into the geochemical signature of the Neoproterozoic Urucum iron formation, Brazil. *Journal of South American Earth Sciences* 96, 102313, ISSN 0895-9811, doi: <https://doi.org/10.1016/j.jsames.2019.102313>
- D'el-Rey Silva LJH, Oliveira IL.de, Pohren CB, Tanizaki MLN, Carneiro RC, Fernandes GL de F, and Aragão PE (2011).** Coeval perpendicular shortenings in the Brasília belt: collision of irregular plate margins leading to oroclinal bending in the Neoproterozoic of central Brazil. *Journal of South American Earth Science* 32 (1), pp. 1–13. doi: <http://dx.doi.org/10.1016/j.jsames.2011.02.013>
- D'el-Rey Silva LJM, Walde DHG, and Saldanha DO (2016).** The Neoproterozoic–Cambrian Paraguay Belt, central Brazil: Part I — New structural data and a new approach on the regional implications. *Tectonophysics* 676, pp. 20-41. ISSN 0040-1951, doi: <https://doi.org/10.1016/j.tecto.2016.03.019>
- Dorr JVN 2<sup>nd</sup> (1945).** Manganese and iron deposits of Morro do Urucum, Mato Grosso Brazil. *U.S. Geological Survey Bulletin* 946A, pp. 1–47.
- Dorr JVN 2<sup>nd</sup> (1973).** Iron-formation in South America. *Economic Geology* 68, pp. 1005–1022.
- Døssing LN, Dideriksen K, Stipp SLS, and Frei R. (2011).** Reduction of hexavalent chromium by ferrous iron: A process of chromium isotope fractionation and its relevance to natural environments. *Chemical Geology* 285 (1), pp. 157–166.
- Douville E, Charlou JL, Oelkers EH, Bienvenu P, Jove Colon CF, Donval JP, Fouquet Y, Prieur D, and Appriou P (2002).** The rainbow vent fluids (36\_140N, MAR): the influence of ultramafic rocks and phase separation on trace metal content in Mid-Atlantic Ridge hydrothermal fluids. *Chemical Geology* 184, pp. 37–48.
- Dymek RF, and Klein C (1988).** Chemistry, petrology and origin of banded iron-formation lithologies from the 3800 MA isua supracrustal belt, West Greenland. *Precambrian Research* 39 (4), pp. 247-302. ISSN 0301-9268, doi: [https://doi.org/10.1016/0301-9268\(88\)90022-8](https://doi.org/10.1016/0301-9268(88)90022-8).
- Edmonds HN, and German CR (2004).** Particle geochemistry in the Rainbow hydrothermal plume, Mid-Atlantic Ridge. *Geochimica et Cosmochimica Acta* 68, pp.759–772.
- Edwards KJ, Rogers DR, Wirsén CO, and McCollom TM (2003).** Isolation and characterization of novel psychrophilic, neutrophilic, Fe-oxidizing, chemolithoautotrophic  $\alpha$ - and  $\gamma$ -Proteobacteria from the deep sea. *Applied and Environmental Microbiology* 69, pp. 2906–2913.
- Ehrenreich A, and Widdel F (1994).** Anaerobic oxidation of ferrous iron by purple bacteria, a new type of phototrophic metabolism. *Applied and Environmental Microbiology* 60, pp. 4517–4526.

- Engler A (2011).** *Geology Volume IV – The Geology of South America. In: Encyclopedia of Life Support Systems (EOLSS), Developed under the Auspices of the UNESCO, Eolss Publishers, Paris, France, [https://www.eolss.net]*
- Evans R (1894).** The geology of Mato Grosso, particularly the region drained by upper Paraguay. *Geological Society of London Quarterly Journal* 50, pp. 85-104.
- Fanning CM, and Link PK (2008).** Age constraints for the sturtian glaciation: data from the Adelaide Geosyncline, south Australia and Pocatello formation, Idaho, USA. In: Gallagher, S.J., Wallace, M.W. (Eds.), *Neoproterozoic Extreme Climates and the Origin of Early Life, Selwyn Symposium of the GSA Victoria Division Geological Society of Australia Extended Abstracts* 91, pp. 57–62.
- Farquhar J, Zerkle AL, and Bekker A (2011).** Geological constraints on the origin of oxygenic photosynthesis. *Photosynthesis Research* 107(1), pp. 11–36.
- Farquhar J, Zerkle AL, and Bekker A (2014).** 6.4 - Geologic and Geochemical Constraints on Earth's Early Atmosphere, In: Holland HD and Turekian KK (eds.), *Treatise on Geochemistry (Second Edition)*, pp. 91-138. Elsevier, ISBN 9780080983004, doi: <https://doi.org/10.1016/B978-0-08-095975-7.01304-8>
- Feely RA, Trefry JH, Lebon GT, and German CR (1998).** The relationship between P/Fe and V/Fe ratios in hydrothermal precipitates and dissolved phosphate in seawater. *Geophysical Research Letters* 25, pp. 2253–2256.
- Fralick P, Davis DW, and Kissin SA (2002).** The age of the Gunflint Formation, Ontario, Canada: single zircon U-Pb age determinations from reworked volcanic ash. *Canadian Journal of Earth Science* 39, pp. 1085–1091.
- Frei R, Dahl PS, Duke EF, Frei KM, Hansen TR, Frandsen MM, and Jensen LA (2008).** Trace element and isotopic characterization of Neoproterozoic and Paleoproterozoic iron formations in the Black Hills (South Dakota, USA): assessment of chemical change during 2.9-1.9 Ga deposition bracketing the 2.4-2.2 Ga first rise of atmospheric oxygen. *Precambrian Research* 162, pp. 441–474.
- Frei R, Døssing LN, Gaucher C, Boggiani PC, Frei KM, Bech Ártung T, Crowe SA, and Freitas BT (2017).** Extensive oxidative weathering in the aftermath of a late Neoproterozoic glaciation – Evidence from trace element and chromium isotope records in the Urucum district (Jacadigo Group) and Puga iron formations (Mato Grosso do Sul, Brazil). *Gondwana Research* 49, pp. 1-20. ISSN 1342-937X, doi: <https://doi.org/10.1016/j.gr.2017.05.003>
- Frei R, Gaucher C, Poulton SW, and Canfield DE (2009).** Fluctuations in Precambrian atmospheric oxygenation recorded by chromium isotopes. *Nature* 461, pp.225–250.
- Freitas BT, Warren LV, Boggiani PC, De Almeida RP, and Piacentini T. (2011).** Tectono-sedimentary evolution of the Neoproterozoic BIF-bearing Jacadigo Group, SW-Brazil, *Sedimentary Geology* 238, (Issues 1–2), pp. 48-70. ISSN 0037-0738, doi: <https://doi.org/10.1016/j.sedgeo.2011.04.001>
- Frost CD, von Blanckenburg F, Schoenberg R, Frost BR, and Swapp S (2007).** Preservation of Fe isotope heterogeneities during diagenesis and metamorphism of banded iron formation. *Contributions to Mineralogy and Petrology* 153 (2), pp. 211 - 235. doi: <https://doi.org/10.1007/s00410-006-0141-0>
- Fuck RA, Pimentel MM, Soares JEP, and Dantas EL (2006).** Faixa Brasília: Uma revisão. *XLIII Congresso Brasileiro de Geologia, Aracaju, Anais SBG, SO4:AO-073*, p. 27.
- Gaucher C, and Poiré D (2009).** Biostratigraphy. Neoproterozoic-Cambrian evolution of the Río de la Plata Palaeocontinent. In: Gaucher, C., Sial, A.N., Halverson, G.P., Frimmel, H.E. (Eds.), *Neoproterozoic-cambrian Tectonics, Global Change and Evolution: A Focus on Southwestern Gondwana. Developments in Precambrian Geology* 16. Elsevier, pp. 103–114.
- Gaucher C, Boggiani PC, Sprechmann P, Sial AN, and Fairchild TR (2003).** Integrated correlation of the Vendian to Cambrian Arroyo del Soldado and Corumbá Groups (Uruguay and Brazil): palaeogeographic, palaeoclimatic and palaeobiologic implications. *Precambrian Research* 120 (3–4), pp. 241-278. ISSN 0301-9268, doi: [https://doi.org/10.1016/S0301-9268\(02\)00140-7](https://doi.org/10.1016/S0301-9268(02)00140-7)
- Gaucher C, Sial AN, and Frei R (2015).** Chapter 17 - Chemostratigraphy of Neoproterozoic Banded Iron Formation (BIF): Types, Age and Origin. In: Ramkumar Mu (ed), *Chemostratigraphy: Concepts, Techniques and Applications*, pp.433-449. United States, Elsevier, ISBN: 9780124199682, doi: <https://doi.org/10.1016/B978-0-12-419968-2.00017-0>
- Georg R, West A, Vance D, Newman K, and Halliday A (2013).** Is the marine osmium isotope record a probe for CO<sub>2</sub> release from sedimentary rocks? *Earth and Planetary Science Letters* 367, pp. 28–38.
- Geraldes MC, Tassinari CCG, Babinski M, Martinelli CD, Iyer SS, Barboza ES, Pinho FEC, and Onoe AT (2008).** Isotopic Evidence for the Late Brasiliano (500–550 Ma) Ore-Forming Mineralization of the Araés Gold Deposit, Brazil. *International Geology Review* 50, p. 177–190. doi: 10.2747/0020-6814.50.2.177

- German CR, Holliday BP, and Elderfield H (1991).** Redox cycling of rare earth elements in the suboxic zone of the Black Sea. *Geochimica et Cosmochimica Acta* 55, pp.3553–3558.
- Glikson AY and Hickman AH (2014).** Coupled asteroid impacts and banded iron-formations, Fortescue and Hamersley Groups, Pilbara, Western Australia. *Australian Journal of Earth Science* 61, pp.689–701.
- Godoi HO, Martins EG, and Mello JCR (2001).** Programa Levantamentos Geológicos do Brasil — PLGB. Corumbá — Folha SE.21-Y-D, Aldeia Tomázia — Folha SF.21-V-B, Porto Murinho — Folha SF.21-V-D, Estado de Mato Grosso do Sul. Escala 1:250.000. *Brasília: CPRM/DIEDIG/DEPAT. 65 p., ilustrações e mapas. 1 CD-ROM.* (available at <http://www.cprm.gov.br>).
- Gole MJ, and Klein C (1981).** Banded iron-formation through much of Precambrian time. *Journal of Geology* 89, pp. 169–183. doi: 10.1086/628578
- Goto KT, Sekine Y, Shimoda G, Hein JR, Aoki S, Ishikawa A, Suzuki K, Gordon GW, and Anbar AD (2020).** A framework for understanding Mo isotope records of Archean and Paleoproterozoic Fe- and Mn-rich sedimentary rocks: Insights from modern marine hydrothermal Fe-Mn oxides. *Geochimica et Cosmochimica Acta* 280, pp. 221–236.
- Gourcerol B, Thurston PC, Kontak DJ, Côté-Mantha O, and Biczok J (2016).** Depositional setting of Algoma-type banded iron formation. *Precambrian Research* 281, pp. 47–79.
- Graf JL, O'Connor EA, and van Leeuwen P (1994).** Rare earth element evidence of origin and depositional environment of Late Proterozoic ironstone beds and manganese-oxide deposits, SW Brazil and SE Bolivia. *Journal of South American Earth Sciences* 7 (2), pp. 115-133. ISSN 0895-9811, doi: [https://doi.org/10.1016/0895-9811\(94\)90003-5](https://doi.org/10.1016/0895-9811(94)90003-5)
- Gross G (1983).** Tectonic systems and the deposition of iron-formation. *Precambrian Research* 20, pp. 171–187.
- Gross GA (1980).** A classification of iron-formation based on depositional environments. *Canadian Mineralogist* 18, pp. 215–222.
- Halevy I, Alesker M, Schuster EM, Popovitz-Biro R, and Feldman Y (2017).** A key role for green rust in the Precambrian oceans and the genesis of iron formations. *Nature Geoscience* 10 (2), pp. 135–139.
- Hamilton MA, Buchan KL, Ernst RE, and Stott GM (2009).** Widespread and short-lived 1870 Ma mafic magmatism along the northern Superior craton margin. *Eos Transactions, American Geophysical Union* 90 (22), Joint Assembly Supplement: Abstract GA11A-01.
- Han TM and Runnegar B (1992).** Megascopic eukaryotic algae from the 2.1-billion-year old Negaunee Iron-Formation, Michigan. *Science* 257, pp. 232–235.
- Hannah JL and Stein HJ (2012).** Re–Os geochemistry. In: Melezhik, V. A., Kump, L. R., Fallick, A. E., Strauss, H., Hanski, E. J., Prave, A. R., and Lepland, A. (eds.). *Reading the Archive of Earth's Oxygenation, volume 3: Global Events and the Fennoscandian Arctic Russia – Drilling Early Earth Project.* Berlin/Heidelberg: Springer, pp. 1506–1514.
- Hannah JL, Bekker A, Stein HJ, Markey RJ, and Holland HD (2004).** Primitive Os and 2316 Ma age for marine shale: implications for paleoproterozoic glacial events and the rise of atmospheric oxygen. *Earth and Planetary Science Letters* 225, pp. 43–52.
- Haralyi NLE (1972).** Novos dados sobre a geologia da região de Corumbá (MT). *Congresso da Sociedade Brasileira de Geociências, 26th, Rio de Janeiro, Abstracts*, p.101.
- Haralyi NLE, and Walde DHG (1986).** Os minerais de ferro e manganês da região de Urucum, Mato Grosso do Sul. In: Schobenhau C, Coelho CES (eds.), *Principais Depósitos Minerais do Brasil. Depart. Nacil. Produção Mineral (Brasília, Brazil)* 2, pp. 127–144.
- Hasui Y, and de Almeida FFM (1970).** Geocronologia do centro-oeste brasileiro. *Boletim da Sociedade Brasileira de Geologia* 19, pp. 5–26.
- Haugaard R, Pecoits E, Lalonde S, Rouxel O, and Konhauser K (2016).** The Joffre banded iron formation, Hamersley Group, Western Australia: Assessing the palaeoenvironment through detailed petrology and chemostratigraphy. *Precambrian Research* 273, pp. 12–37.
- Heaman LM (1997).** Global mafic volcanism at 2.45 Ga: Remnants of an ancient large igneous province? *Geology* 25, pp. 299–302.
- Heaman LM, Peck D, and Toope K, (2009).** Timing and geochemistry of 1.88 Ga Molson igneous events, Manitoba: insights into the formation of a craton-scale magmatic and metallogenic province. *Precambrian Research* 172, pp. 143–162.
- Heard AW, Aarons SM, Hofmann A, He X, Ireland T, Bekker A, Qin L, and Dauphas N (2021).** Anoxic continental surface weathering recorded by the 2.95 Ga Denny Dalton Paleosol (Pongola Supergroup, South Africa). *Geochimica et Cosmochimica Acta* 295, pp. 1–23.
- Heard AW, Dauphas N, Guilbaud R, Rouxel O, Butler IB, Nie NX, and Bekker A (2020).** Triple iron isotope constraints on the role of ocean iron sinks in early atmospheric oxygenation. *Science* 370, pp. 446–449.

- Heilbron M, Cordani UG, and Alkmim FF (2017).** The São Francisco Craton and Its Margins. In: Heilbron M, Cordani U, Alkmim F (eds.). *São Francisco Craton, Eastern Brazil. Regional Geology Reviews* pp. 3-13. Springer, Cham. doi: [https://doi.org/10.1007/978-3-319-01715-0\\_1](https://doi.org/10.1007/978-3-319-01715-0_1)
- Heimann A, Johnson C, Beard B, Valley JW, Roden E, Spicuzza M, and Beukes NJ (2010).** Fe, C, and O isotope compositions of banded iron formation carbonates demonstrate a major role for dissimilatory iron reduction in 2.5 Ga marine environments. *Earth and Planetary Science Letters* 294, pp. 8–18.
- Hoffman PF, Abbot DS, Ashkenazy Y, Benn DI, Brocks JJ, Cohen PA, Cox GM, Creveling JR, Donnadieu Y, Erwin DH, Fairchild IJ, Ferreira D, Goodman JC, Halverson GP, Jansen MF, Le Hir G, Love GD, Macdonald FA, Maloof AC, Partin CA, Ramstein G, Rose BEJ, Rose CV, Sadler PM, Tziperman E, Voigt A, and Warren SG (2017).** Snowball Earth climate dynamics and Cryogenian geology-geobiology. *Science Advances* 3 (11): e160098. doi: 10.1126/sciadv.1600983
- Hoffman PF, Kaufman AJ, Halverson GP, and Schrag DP (1998).** A Neoproterozoic snowball Earth. *Science* 281, pp. 1342–1346.
- Hoffman PF, Macdonald FA, and Halverson GP (2011).** Chapter 5 Chemical sediments associated with Neoproterozoic glaciation: iron formation, cap carbonate, barite and phosphorite. In: Arnaud E, Halverson GP, and Shields-Zhou G (eds.). *The Geological Record of Neoproterozoic Glaciations*. Geological Society, London, Memoirs 36 (1), pp. 67–80.
- Hoffmann KH, Condon DJ, Bowring SA, and Crowley JL (2004).** U–Pb zircon date from the Neoproterozoic Ghaub Formation, Namibia: constraints on Marinoan glaciation. *Geology* 32, pp. 817–820.
- Holland HD (1973).** The oceans: A possible source of iron in iron-formations. *Economic Geology* 68(7), pp. 1169–1172.
- Holland HD (1984).** The Chemical Evolution of the Atmosphere and Oceans. *Princeton Series in Geochemistry*. Princeton, NJ: Princeton University Press.
- Holland HD (2002).** Volcanic gases, black smokers, and the Great Oxidation Event. *Geochimica et Cosmochimica Acta* 66, pp. 3811–3826.
- Hoppe A, Schobbenhaus C, and Walde DHG (1987).** Precambrian iron formations in Brazil. In: Uitterdijk PW and LaBerge GL (eds.). *Precambrian Iron Formations*. Theophrastus Publications, Athens, Greece, pp. 347–390.
- Horan MF, Walker RJ, Gao S, Lorand J-P, and Rudnick RL (2006).** Highly siderophile element composition of the Earth's primitive upper mantle: Constraints from new data on peridotite massifs and xenoliths. *Geochimica et Cosmochimica Acta* 70, pp. 4528–4550
- Horan MF, Walker RJ, Morgan JW, Grossman JN, and Ruben AE (2003).** Highly siderophile elements in chondrites. *Chemical Geology* 196 (1–4), pp. 27-42 ISSN 0009-2541, doi: [https://doi.org/10.1016/S0009-2541\(02\)00405-9](https://doi.org/10.1016/S0009-2541(02)00405-9)
- Hu Y and Teng F-Z (2021).** Non-Traditional Stable Isotope Geochemistry. In: David Alderton, Scott A. Elias (eds.) *Encyclopedia of Geology (Second Edition)*, Academic Press, pp. 114-124. ISBN 9780081029091, doi: <https://doi.org/10.1016/B978-0-08-102908-4.00148-X>
- Huang Q, Viehmann S, Walde DHG, and Li W (2021).** Iron isotope constraints on the metal source and depositional environment of the Neoproterozoic banded iron- and manganese deposits in Urucum, Brazil. *Geochemistry* 81 (3), 125771, ISSN 0009-2819, doi: <https://doi.org/10.1016/j.chemer.2021.125771>
- Isley AE (1995).** Hydrothermal plumes and the delivery of iron to banded iron formation. *Journal of Geology* 103, pp. 169–185. doi: <https://doi.org/10.1086/629734>
- Isley AE, and Abbott DH (1999).** Plume-related mafic volcanism and the deposition of banded iron formation. *Journal of Geophysical Research* 104, pp. 15461–15477. doi: 10.1029/1999JB900066
- James HL (1954).** Sedimentary facies of iron-formation. *Economic Geology* 49, pp. 235–293. doi: <https://doi.org/10.2113/gsecongeo.49.3.235>
- James HL (1983).** Distribution of banded iron-formation in space and time. In: Trendall AF and Morris RC (eds.) *Iron-Formation Facts and Problems*, pp. 471–490. Amsterdam: Elsevier. doi: [https://doi.org/10.1016/S0166-2635\(08\)70053-7](https://doi.org/10.1016/S0166-2635(08)70053-7)
- James HL, Dutton CE, Pettijohn FJ, and Wier KL (1968).** Geology and ore deposits of the Iron River-Crystal Falls district, Iron County, Michigan. U. S. *Geological Survey Professional Paper* 570, pp. 1–134. doi: <https://doi.org/10.3133/pp570>
- Javaux EJ (2011).** Early eukaryotes in Precambrian oceans. In: Gargaud M, Lo´pez- Garcia P, and Martin H (eds.) *Origins and Evolution of Life: An Astrobiological Perspective*, pp. 414–449. Cambridge: Cambridge University Press.
- Johnson CM, Beard BL, Klein C, Beukes NJ, and Roden EE (2008).** Iron isotopes constrain biologic and abiologic processes in banded iron formation genesis. *Geochimica et Cosmochimica Acta* 72, pp. 151–169.

- Kamber BS, Bolhar R, and Webb GE (2004).** Geochemistry of late Archaean stromatolites from Zimbabwe: evidence for microbial life in restricted epicontinental seas. *Precambrian Research* 132, pp.379–399. doi: <http://dx.doi.org/10.1016/j.precamres.2004.03.006>.
- Kappler A, Pasquero C, Konhauser KO, and Newman DK (2005).** Deposition of banded iron formations by anoxygenic phototrophic Fe(II)-oxidizing bacteria. *Geology* 33, pp. 865–868.
- Kashiwabara T, Kubo S, Tanaka M, Senda R, Iizuka T, Tanimizu M, and Takahashi Y(2017).** Stable isotope fractionation of tungsten during adsorption on Fe and Mn (oxyhydr)oxides. *Geochimica et Cosmochimica Acta* 204, pp. 52–67. ISSN 0016-7037, doi: <https://doi.org/10.1016/j.gca.2017.01.031>
- Kendall B (2014).** An osmium-based method for assessing the source of dissolved rhenium and molybdenum to Archean seawater. *Chemical Geology* 385, pp. 92–103, doi: <https://doi.org/10.1016/j.chemgeo.2014.07.021>
- Kendall B, Creaser RA, Reinhard CT, Lyons TW, and Anbar AD (2015).** Transient episodes of mild environmental oxygenation and oxidative continental weathering during the late Archean. *Science Advances* 1 (10), article #e1500777, pp. 6. doi: <https://doi.org/10.1126/sciadv.1500777>
- Kirschvink JL (1992).** Late Proterozoic Low-Latitude Global Glaciation: the Snowball Earth. In: Schopf JW, Klein C (eds.). *The Proterozoic Biosphere: a Multidisciplinary Study*, Cambridge University Press, New York, pp. 51–52.
- Klein C (2005).** Some Precambrian banded iron-formations (BIFs) from around the world: their age, geologic setting, mineralogy, metamorphism, geochemistry, and origin. *American Mineralogist* 90, pp. 1473–1499.
- Klein C and Beukes NJ (1992).** Time Distribution, Stratigraphy and Sedimentologic Setting and Geochemistry of Precambrian Iron Formation. In: Schopf JW, Klein C (eds.), *The Proterozoic Biosphere: A Multidisciplinary Study*, Cambridge University Press, New York, pp.139–146.
- Klein C and Beukes NJ (1993).** Sedimentology and Geochemistry of the Glaciogenic Late Proterozoic Rapitan Iron-Formation in Canada. *Economy Geology* 88, pp. 542–565. doi: <https://doi.org/10.2113/gsecongeo.88.3.542>
- Klein C and Ladeira EA (2004).** Geochemistry and mineralogy of Neoproterozoic banded iron-formations and some selected, siliceous manganese formations from the Urucum District, Mato Grosso Do Sul, Brazil. *Economy Geology* 99 (6), pp. 1233–1244.
- Kleine T and Walker RJ (2017).** Tungsten Isotopes in Planets. *Annual review of earth and planetary sciences*, 45, pp. 389–417. doi: <https://doi.org/10.1146/annurev-earth-063016-020037>
- Knauth LP, and Lowe DR (2003).** High Archean climatic temperature inferred from oxygen isotope geochemistry of cherts in the 3.5 Ga Swaziland Supergroup, South Africa. *Geological Society of America Bulletin* 115, pp. 566–580.
- Knight KB, Renne PR, Halkett A, and White N (2003).** <sup>40</sup>Ar/<sup>39</sup>Ar dating of the Rajahmundry Traps, Eastern India and their relationship to the Deccan Traps. *Earth and Planetary Science Letters* 208 (1–2), pp. 85–99. doi: [https://doi.org/10.1016/S0012-821X\(02\)01154-8](https://doi.org/10.1016/S0012-821X(02)01154-8)
- Knoll AH, Javaux EJ, Hewitt D, and Cohen P (2006).** Eukaryotic organisms in Proterozoic oceans. *Philosophical Transactions of the Royal Society Series B* 361, pp. 1023–1038.
- Koeberl C (2001).** The sedimentary record of impact events. In: Peucker-Ehrenbrink B, Schmitz B (eds.). *Accretion of Extraterrestrial Matter Throughout Earth's History*, pp. 333–378. Kluwer Academic Plenum, New York.
- Koeberl C (2006).** Impact Processes on the Early Earth. *Elements*. 2, pp. 211–216. doi: [10.2113/gselements.2.4.211](https://doi.org/10.2113/gselements.2.4.211).
- Koeberl C (2014).** 2.5 - The Geochemistry and Cosmochemistry of Impacts. In: Holland HD, Turekian KK (eds.). *Treatise on Geochemistry (Second Edition)*, Elsevier, pp. 73–118. ISBN 9780080983004, doi: <https://doi.org/10.1016/B978-0-08-095975-7.00130-3>.
- Koeberl C, Ivanov BA, and Goodman BA (2007a).** Impact triggering of the Snowball Earth deglaciation? Bridging the Gap II: Effect of Target Properties on the Impact Cratering Process. *Abstracts of the conference held September 22-26, 2007, in Saint-Hubert, Canada. Lunar and Planetary Institute*
- Koeberl C, Ivanov, BA, and Goodman J (2007b).** Impact-induced deglaciation of the Snowball Earth? *EOS Transactions American Geophysical Union* 88 (52), *Fall Meeting Supplement*, Abstract U22A-08.
- Koeberl C, Reimold WU, and Boer RH (1993).** Geochemistry and mineralogy of Early Archean spherule beds, Barberton Mountain Land, South Africa: evidence for origin by impact doubtful. *Earth and Planetary Science Letters* 119, pp.441–452.
- Koeberl, C. and Ivanov, B.A. (2019).** Asteroid impact effects on Snowball Earth. *Meteoritics & Planetary Science* 54 (10), pp.2273–2285. doi: <https://doi.org/10.1111/maps.13294>
- Koeberl, C., Reimold, W.U., McDonald, I., and Rosing, M. (2000).** Search for petrographical and geochemical evidence for the late heavy bombardment on Earth in Early Archean rocks from Isua, Greenland. In:

- Gilmour I, Koeberl C (eds.). *Impacts and the Early Earth. Lecture Notes in Earth Sciences 91*, Springer Verlag, Heidelberg, pp. 73-97
- Koide M, Goldberg ED, Niemeyer S, Gerlach D, Hodge V, Bertine KK, and Padova A (1991)**. Osmium in marine sediment. *Geochimica et Cosmochimica Acta* 55, pp. 1641–1648.
- Koide M, Hodge V, Yang JS, and Goldberg ED (1987)**. Determination of rhenium in marine waters and sediments by graphite furnace atomic absorption spectrometry. *Analytical Chemistry* 59, pp. 1802-1805.
- Konhauser KO, Amskold L, Lalonde SV, Posth NR, Kappler A, and Anbar A (2007)**. Decoupling photochemical Fe(II) oxidation from shallow-water BIF deposition. *Earth and Planetary Science Letters* 258, pp. 87–100.
- Konhauser KO, Hamade T, Raiswell R, Morris RC, Ferris FG, Southam G, and Canfield DE (2002)**. Could bacteria have formed the Precambrian banded iron formations? *Geology* 30, pp. 1079–1082.
- Konhauser KO, Kappler A, and Roden E (2011a)**. Iron in Microbial Metabolisms. *Elements* 7 (2), pp. 89-93. doi: 10.2113/gselements.7.2.89.
- Konhauser KO, Lalonde S, Planavsky NJ, Pecoits E, Lyons TW, Mojzsis SJ, Rouxel O, Barley ME, Rosiere C, Fralick PW, Kump LE, and Bekker A (2011b)**. Aerobic bacterial pyrite oxidation and acid rock drainage during the Great Oxidation Event. *Nature* 478, pp.369–373.
- Konhauser KO, Lalonde SV, Amskold L, and Holland HD (2007)**. Was there really an Archean phosphate crisis? *Science* 315 (5816), 1234. doi: 10.1126/science.1136328
- Konhauser KO, Newman DK, and Kappler A (2005)**. The potential significance of microbial Fe(III) reduction during deposition of Precambrian banded iron formations. *Geobiology* 3, pp. 167-177. doi: <https://doi.org/10.1111/j.1472-4669.2005.00055.x>
- Konhauser KO, Pecoits E, Lalonde SV, Papineu D, Nisbet EG, Barley ME, Arndt NT, Zahnle K and Kamber BS (2009)**. Oceanic nickel depletion and a methanogen famine before the Great Oxidation Event. *Nature* 458, pp.750–753.
- Konhauser KO, Planavsky NJ, Hardisty DS, Robbins LJ, Warchola TJ, Haugaard R, Lalonde SV, Partin CA, Oonk PBH, Tsikos H, Lyons TW, Bekker A, and Johnson CM (2017)**. Iron formations: A global record of Neoproterozoic to Palaeoproterozoic environmental history. *Earth-Science Reviews* 172, pp. 140-177, ISSN 0012-8252, doi: <https://doi.org/10.1016/j.earscirev.2017.06.012>
- Kopp RE, Kirschvink JL, Hilburn IA, and Nash CZ (2005)**. The Paleoproterozoic snowball Earth: A climate disaster triggered by the evolution of oxygenic photosynthesis. *Proceedings of the National Academy of Sciences* 102 (32), pp. 11131-11136. doi: 10.1073/pnas.0504878102
- Kump LR and Seyfried WE (2005)**. Hydrothermal Fe fluxes during the Precambrian: effect of low oceanic sulfate concentrations and low hydrostatic pressure on the composition of black smokers. *Earth and Planetary Science Letters* 235, pp. 654–662.
- Laajoki K and Saikkonen R (1977)**. On the geology and geochemistry of the Precambrian iron formations in Väyrylänkylä, South Puolanka area, Finland. *Geological Survey of Finland Bulletin* 292, pp. 1–137.
- Lacerda-Filho JV, Brito RSC de, Silva MG, Oliveira CC de, Moreton LC, Martins EG, Lopes RC, Lima TM, Larizatti JH, and Valente CR (2006)**. Geologia e Recursos Minerais do Estado de Mato Grosso do Sul, Programa Integração, Atualização e Difusão de Dados da Geologia do Brasil: *Convênio CPRM/SEPROTUR/MS, Campo Grande*, 121, escala 1:1.000.000.
- Lau, K, Romaniello S, and Zhang F (2019)**. The Uranium Isotope Paleoredox Proxy. *Elements in Geochemical Tracers in Earth System Science*. Cambridge: Cambridge University Press. doi:10.1017/9781108584142.
- Lee D (1983)**. Palladium and nickel in north-east Pacific waters. *Nature* 305, pp. 47–48. doi: <https://doi.org/10.1038/305047a0>
- Lehours AC, Evans P, Bardot C, Joblin K, and Gerard F (2007)**. Phylogenetic diversity of archaea and bacteria in the anoxic zone of a meromictic lake (Lake Pavin, France). *Applied and Environmental Microbiology* 73, pp. 2016–2019.
- Leonardos OH, and Walde DHG (1982)**. Sobre a estratigrafia e a gênese dos depósitos de manganês a luz do vulcanismo Jacadigo. *Congresso da Sociedade Brasileira de Geociências, 27th. Abstracts, Salvador*, p. 203.
- Lepp H, and Goldich SS (1964)**. Origin of Precambrian iron formations. *Economic Geology* 59, pp. 1025–1060.
- Li S, Chai Z, and Mao X (2007)**. Iridium in the Bering Sea and Arctic Ocean studied by neutron activation analysis. *Journal of Radioanalytical and Nuclear Chemistry* 271, pp. 125–128. doi: <https://doi.org/10.1007/s10967-007-0117-1>
- Lowe DR and Byerly GR (1986)**. Early Archean silicate spherules of probable impact origin, South Africa and Western Australia. *Geology* 14, pp. 83–86.
- Lu X, Kendall B, Stein HJ, and Hannah JL (2017)**. Temporal record of osmium concentrations and 187Os/188Os in organic-rich mudrocks: implications for the osmium geochemical cycle and the use of osmium as a

- paleoceanographic tracer. *Geochimica et Cosmochimica Acta* 216, pp. 221-241, doi: <https://doi.org/10.1016/j.gca.2017.06.046>
- Luguet A, Behrens M, Pearson DG, König S, and Herwartz D (2015).** Significance of the whole rock Re–Os ages in cryptically and modally metasomatised cratonic peridotites: Constraints from HSE–Se–Te systematics. *Geochimica et Cosmochimica Acta* 164, pp. 441-463, ISSN 0016-7037, doi: <https://doi.org/10.1016/j.gca.2015.06.016>.
- Luguet A, Nowell GM, and Pearson DG (2008).** 184Os/188Os and 186Os/188Os measurements by Negative Thermal Ionisation Mass Spectrometry (N-TIMS): effects of interfering element and mass fractionation corrections on data accuracy and precision. *Chemical Geology* 248 (3-4), pp. 342–362.
- Lyons TW, Reinhard CT, and Planavsky NJ (2014).** The rise of oxygen in Earth's early ocean and atmosphere. *Nature* 506, pp. 307–315.
- Macdonald FA, Schmitz MD, Crowley JL, Roots CF, Jones DS, Maloof AC, Strauss JV, Cohen PA, Johnston DT, and Schrag DP (2010).** Calibrating the Cryogenian. *Science* 327, pp. 1241–1243.
- Maier WD, Peltonen P, McDonald I, Barnes SJ, Barnes S-J, Hatton C, and Viljoen F (2012).** The concentration of platinum-group elements and gold in southern African and Karelian kimberlite-hosted mantle xenoliths: Implications for the noble metal content of the Earth's mantle. *Chemical Geology* 302–303, pp. 119-135, ISSN 0009-2541, doi: <https://doi.org/10.1016/j.chemgeo.2011.06.014>.
- Maliva RG, Knoll AH, and Simonson BM (2005).** Secular change in the Precambrian silica cycle: insights from chert petrology. *Geological Society of America Bulletin* 117, pp. 835–845.
- Mänd K, Robbins L, Planavsky N, Bekker A, and Konhauser KO (2022).** Iron Formations as Palaeoenvironmental Archives (*Elements in Geochemical Tracers in Earth System Science*). Cambridge: Cambridge University Press. doi:10.1017/9781108993791
- Markey RJ, Hannah JL, Morgan JW, and Stein HJ (2003).** A double spike for osmium analysis of highly radiogenic samples. *Chemical Geology* 200, pp. 395–406.
- Mashio AS, Obata H, and Gamo T (2017).** Dissolved platinum concentrations in coastal seawater: Boso to Sanriku areas, Japan. *Archives of Environmental Contamination and Toxicology* 73, pp. 240-246.
- McArthur JM, Donovan DT, Thirlwall MF, Fouke BW, and Matthey D (2000).** Strontium isotope profile of the early Toarcian (Jurassic) anoxic event, the duration of ammonite biozones, and belemnite palaeotemperatures. *Earth and Planetary Science Letters* 179, pp. 269–285.
- McLennan SM (1989).** Rare earth elements in sedimentary rocks: influence of provenance and sedimentary processes. In: Lipin, B.R., McKay, G.A. (eds.). *Geochemistry and Mineralogy of Rare Earth Elements. Reviews in Mineralogy* 21, pp. 169–200. doi: <https://doi.org/10.1515/9781501509032-010>
- Meisel T, Burnham OM, Kriete C, and Schulz T (2013).** Osmium isotope and PGE reference materials OKUM and MUH-1. *Mineralogical Magazine* 77, p.1734.
- Meisel T, Walker RJ, Irving AJ, and Lorand J-P (2001).** Osmium isotopic compositions of mantle xenoliths: a global perspective. *Geochim Cosmochim Acta* 65, pp.1311–1323.
- Miller R and O'Nions R (1985).** Source of Precambrian chemical and clastic sediments. *Nature* 314, pp. 325–330. doi: <https://doi.org/10.1038/314325a0>
- Mloszewska AM, Pecoits E, Cates NL, Mojzsis SJ, O'Neil J, Robbins LJ, and Konhauser KO (2012).** The composition of Earth's oldest iron formations: The Nuvvuagittuq Supracrustal Belt (Québec, Canada). *Earth and Planetary Science Letters* 317–318, pp. 331–342.
- Morgan JW, Walker RJ, Brandon AD, and Horan MF (2001).** Siderophile elements in Earth's upper mantle and lunar breccias: Data synthesis suggests manifestations of the same late influx. *Meteoritic & Planetary Science* 36 (9), pp. 1257–1275
- Muhling JR and Rasmussen B (2020).** Widespread deposition of greenalite to form banded iron formations before the Great Oxidation Event. *Precambrian Research* 339, 105619.
- Mukhopadhyay J, Beukes NJ, Armstrong RA, Zimmermann U, Ghosh G, and Medda RA (2008).** Dating the Oldest Greenstone in India: A 3.51-Ga Precise U-Pb SHRIMP Zircon Age for Dacitic Lava of the Southern Iron Ore Group, Singhbhum Craton. *The Journal of Geology* 116 (5), pp. 449-461. doi: <https://doi.org/10.1086/590133>
- Mundi-Petermeier A, Viehmann S, Tusch J, Bau M, Kurzweil F, and Münker C (2022).** Earth's geodynamic evolution constrained by <sup>182</sup>W in Archean seawater. *Nature Communications* 13, 2701. doi: <https://doi.org/10.1038/s41467-022-30423-3>
- Nance WB and Taylor SR (1976).** Rare earth element patterns and crustal evolution—I. Australian post-Archean sedimentary rocks. *Geochimica et Cosmochimica Acta* 40 (12), pp. 1539-1551. ISSN 0016-7037, doi: [https://doi.org/10.1016/0016-7037\(76\)90093-4](https://doi.org/10.1016/0016-7037(76)90093-4)
- Nebel O (2016).** Strontium. In: White, W. (eds) *Encyclopedia of Geochemistry. Encyclopedia of Earth Sciences Series*. Springer, Cham., pp. 1377-1378. doi: [https://doi.org/10.1007/978-3-319-39193-9\\_138-1](https://doi.org/10.1007/978-3-319-39193-9_138-1)

- Nozaki Y, Zhang J, and Amakawa H (1997).** The fractionation between Y and Ho in the marine environment. *Earth and Planetary Science Letters* 148 (1–2), pp. 329–340. ISSN 0012-821X, doi: [https://doi.org/10.1016/S0012-821X\(97\)00034-4](https://doi.org/10.1016/S0012-821X(97)00034-4).
- Nutman AP, Bennett VC, and Friend CRL (2017).** Seeing through the magnetite: Reassessing Eoarchean atmosphere composition from Isua (Greenland)  $\geq 3.7$  Ga banded iron formations, *Geoscience Frontiers* 8 (6), pp. 1233–1240, ISSN 1674-9871, doi: <https://doi.org/10.1016/j.gsf.2017.02.008>.
- O'Connor EA, and Walde DHG (1985).** Recognition of an Eocambrian Orogenic Cycle in SW Brazil and SE Bolivia. *Zentralblatt für Geologie und Paläontologie Teil I* 9, pp. 1441–1456. doi: 10.1127/zbl\_geol\_pal\_1/1985/1986/1441
- Ohmoto H, Watanabe Y, Yamaguchi KE, Naraoka H, Haruna M, Kakegawa T, Hayashiji KI, and Kato Y (2006).** Chemical and biological evolution of early Earth: Constraints from banded iron-formations. In: Ohmoto H and Kessler SK (eds.), *Evolution of the Atmosphere, Hydrosphere, and Biosphere on Early Earth: Constraints from Ore Deposits. Geological Society of America Memoirs*, vol. 198, pp. 291–331. Boulder, CO: Geological Society of America. doi: 10.1130/2006.1198(17)
- Olson SL, Kump LR, and Kasting JF (2013).** Quantifying the areal extent and dissolved oxygen concentrations of Archean oxygen oases. *Chemical Geology* 362, Pages 35–43, ISSN 0009-2541. doi: <https://doi.org/10.1016/j.chemgeo.2013.08.012>
- Paakola J (1971).** The volcanic complex and associated manganiferous iron formation of the Porkonen-Pahtavaara area in Finnish Lapland. *Bulletin de la Commission Géologique de Finlande* 247, pp. 1–83.
- Paquay FS, and Ravizza G (2012).** Heterogeneous seawater 187Os/188Os during Late Pleistocene glaciations. *Earth and Planetary Science Letters* 349–350, pp. 126–138.
- Parry LA, Boggiani PC, Condon DJ, Garwood RJ, Leme JDM, McIlroy D, Brasier MD, Trindade R, Campanha GAC, Pacheco MLAF, Diniz CQC, and Liu AG (2017).** Ichnological evidence for meiofaunal bilaterians from the terminal Ediacaran and earliest Cambrian of Brazil. *Nature Ecology & Evolution* 1 (10), pp. 1455–1464. doi: <https://doi.org/10.1038/s41559-017-0301-9>
- Pearson DG and Woodland SJ (2000).** Solvent extraction/anion exchange separation and determination of PGEs (Os, Ir, Pt, Pd, Ru) and Re–Os isotopes in geological samples by isotope dilution ICP-MS. *Chemical Geology* 165 (1–2), pp. 87–107, ISSN 0009-2541, doi: [https://doi.org/10.1016/S0009-2541\(99\)00161-8](https://doi.org/10.1016/S0009-2541(99)00161-8).
- Percak-Dennett EM, Beard BL, Xu H, Konishi H, Johnson CM, and Roden EE (2011).** Iron isotope fractionation during microbial dissimilatory iron oxide reduction in simulated Archean seawater. *Geobiology* 9(3), pp. 205–220.
- Perry EC, Tan FC, and Morey GB (1973).** Geology and stable isotope geochemistry of Biwabik Iron Formation, northern Minnesota. *Economic Geology* 68, pp. 1110–1125. doi: <https://doi.org/10.2113/gsecongeo.68.7.1110>
- Petit JR, Mounier L, Jouzel J, Korotkevich YS, Kotlyakov VI, and Lorius C (1990).** Paleoclimatological and chronological implications of the Vostok core dust record. *Nature* 343, pp. 56–58.
- Peucker-Ehrenbrink B and Hoffman PF (2006).** Sedimentary PGE anomalies at Snowball Earth terminations. (abstract) *Geochimica Et Cosmochimica Acta* 70 (18), A488. doi: 10.1016/j.gca.2006.06.1438.
- Peucker-Ehrenbrink B and Jahn B-m (2001).** Rhenium-osmium isotope systematics and platinum group element concentrations: Loess and the upper continental crust, *Geochemistry, Geophysics, Geosystems* 2 (10), 1061, doi:10.1029/2001GC000172.
- Peucker-Ehrenbrink B, and Ravizza G (1996).** Continental runoff of osmium into the Baltic Sea. *Geology* 24 (4): pp. 327–330. doi: [https://doi.org/10.1130/0091-7613\(1996\)024<0327:CROOIT>2.3.CO;2](https://doi.org/10.1130/0091-7613(1996)024<0327:CROOIT>2.3.CO;2)
- Peucker-Ehrenbrink B, and Ravizza G (2000).** The marine osmium isotope record. *Terra Nova* 12, pp. 205–219. doi: <https://doi.org/10.1046/j.1365-3121.2000.00295.x>
- Peucker-Ehrenbrink B, and Ravizza G (2012).** Chapter 8 - Osmium Isotope Stratigraphy. In: Gradstein FM, Ogg JG, Schmitz MD, Ogg GM (eds.). *The Geologic Time Scale 2012*, pp. 145–166. Elsevier, ISBN: 9780444594259, doi: <https://doi.org/10.1016/B978-0-444-59425-9.00008-1>
- Peucker-Ehrenbrink B, and Ravizza G (2020).** Chapter 8 - Osmium Isotope Stratigraphy, In: Gradstein FM, Ogg JG, Schmitz MD, Ogg GM (eds.), *The Geologic Time Scale 2020*, pp. 239–257. Elsevier, ISBN: 9780128243602, doi: <https://doi.org/10.1016/B978-0-12-824360-2.00008-5>
- Peucker-Ehrenbrink B, Waters CA, Kurz MD, and Hoffman PF (2016).** No evidence of extraterrestrial noble metal and helium anomalies at Marinoan glacial terminations. *Earth and Planetary Science Letters* 437, pp. 76–88. doi: <https://doi.org/10.1016/j.epsl.2015.12.040>
- Piacentini T, Vasconcelos PM, and Farley KA (2013).**  $^{40}\text{Ar}/^{39}\text{Ar}$  constraints on the age and thermal history of the Urucum Neoproterozoic banded iron-formation, Brazil, *Precambrian Research* 228, pp. 48–62. ISSN 0301-9268, doi: <https://doi.org/10.1016/j.precamres.2013.01.002>.

- Pickard AL (2002).** SHRIMP U–Pb zircon ages of tuffaceous mudrocks in the Brockman Iron Formation of the Hamersley Range, Western Australia. *Australian Journal of Earth Sciences* 49, pp. 491–507.
- Pickard AL (2003).** SHRIMP U–Pb zircon ages for the Palaeoproterozoic Kuruman Iron Formation, northern Cape Province, South Africa: Evidence for simultaneous BIF deposition on Kaapvaal and Pilbara Cratons. *Precambrian Research* 125, pp. 275–315.
- Pierrehumbert RT, Abbot DS, Voigt A, and Koll D (2011).** Climate of the Neoproterozoic. *Annual Review of Earth and Planetary Sciences* 39 (1), pp. 417-460. doi: <https://doi.org/10.1146/annurev-earth-040809-152447>
- Pimentel M, Jost H, and Fuck R (2004).** O embasamento da Faixa Brasília e o Arco Magmático de Goiás. *Geologia do Continente Sul-Americano: Evolução da Obra de Fernando Flávio Marques de Almeida*. pp. 355-368.
- Planavsky N, Rouxel O, Bekker A, Shapiro R, Fralick P, and Knudsen A (2009).** Ironoxidizing microbial ecosystems thrived in late Paleoproterozoic redox-stratified oceans. *Earth and Planetary Science Letters* 286, pp. 230–242.
- Planavsky NJ, Asael D, Hofmann A, Reinhard CT, Lalonde SV, Knudsen A, Wang X, Ossa Ossa F, Pecoits E, Smith AJB, Beukes NJ, Bekker A, Johnson TM, Konhauser KO, Lyons TW, and Rouxel OJ (2014).** Evidence for oxygenic photosynthesis half a billion years before the Great Oxidation Event. *Nature Geoscience* 7, pp. 283–286.
- Planavsky NJ, Bekker A, Hofmann A, Owens JD, and Lyons TW (2012).** Sulfur record of rising and falling marine oxygen and sulfate levels during the Lomagundi Event. *Proceedings of the National Academy of Science of the United States of America* 109, pp. 18300–18305.
- Planavsky NJ, Bekker A, Rouxel OJ, Kamber B, Hofmann A, Knudsen A, and Lyons TW (2010).** Rare earth element and yttrium compositions of Archean and Paleoproterozoic Fe formations revisited: New perspectives on the significance and mechanisms of deposition. *Geochimica et Cosmochimica Acta* 74 (22), pp.6387–6405.
- Planavsky, NJ, McGoldrick P, Scott CT, Li C, Reinhard CT, Kelly AE, Chu XL, Bekker A, Love GD, and Lyons TW (2011).** Widespread iron-rich conditions in the mid-Proterozoic ocean. *Nature* 477, pp. 448–495.
- Polgári M, Biondi JC, Gyollai I, Fintor K, and Szabó M (2021).** Origin of the Urucum iron formations (Neoproterozoic, Brazil): Textural and mineralogical evidence (Mato Grosso do Sul – Brazil). *Ore Geology Reviews* 139 (Part A), 104456. ISSN 0169-1368, doi: <https://doi.org/10.1016/j.oregeorev.2021.104456>
- Poulton SW and Canfield DE (2006).** Co-diagenesis of iron and phosphorus in hydrothermal sediments from the southern East Pacific Rise: Implications for the evaluation of paleoseawater phosphate concentrations. *Geochimica et Cosmochimica Acta* 70, pp.5883–5898..
- Puchtel IS, Blichert-Toft J, Touboul M, and Walker RJ (2018).** 182W and HSE constraints from 2.7 Ga komatiites on the heterogeneous nature of the Archean mantle. *Geochimica et Cosmochimica Acta* 228, pp. 1-26. ISSN 0016-7037, doi: <https://doi.org/10.1016/j.gca.2018.02.030>.
- Puchtel IS, Walker RJ, Touboul M, Nisbet EG, and Byerly G (2014).** Insights into early Earth from the Pt-Re-Os isotope and highly siderophile element abundance systematics of Barberton komatiites. *Geochimica et Cosmochimica Acta* 125, pp. 394–413.
- Putzer H (1958).** Die Kryptomelan- und Jaspelit-Lagerstätten von Corumbá im Staate Mato Grosso, Brasilien. *Erzmetall* 11, pp. 527-538.
- Putzer, H., (1958).** Die Kryptomelan- und Jaspelit-Lagerstätten von Corumbá im Staate Mato Grosso. Brasilien. *Erzmetall* 11, pp. 527–538.
- Ragsdale SW (2009).** Nickel-based Enzyme Systems\*. *Journal of Biological Chemistry* 284 (28), pp. 18571-18575. ISSN 0021-9258, doi: <https://doi.org/10.1074/jbc.R900020200>.
- Rai D, Eary LE, and Zachara JM (1989).** Environmental chemistry of chromium. *Science of the Total Environment* 86, pp.15–23.
- Rasmussen B, Muhling JR, Suvorova A, and Krapež B (2017).** Greenalite precipitation linked to the deposition of banded iron formations downslope from a late Archean carbonate platform. *Precambrian Research* 290, pp. 49–62.
- Ravizza G (2007).** Reconstructing the marine 187Os/188Os record and the particulate flux of meteoritic osmium during the late Cretaceous. *Geochimica et Cosmochimica Acta* 71, pp. 1355–1369.
- Ravizza GE, and Peucker-Ehrenbrink B, (2003).** Chemostratigraphic evidence of Deccan volcanism from the marine Os isotope record. *Science* 302, pp. 1392-1395.
- Reisberg L, and Lorand JP (1995).** Longevity of sub-continental mantle lithosphere from osmium isotope systematics in orogenic peridotite massifs. *Nature* 376, pp. 159–162.
- Richter FM, and Turekian KK (1993).** Simple models for the geochemical response of the ocean to climatic and tectonic forcing. *Earth and Planetary Science Letters* 119 (1–2), pp. 121-131. ISSN 0012-821X, doi: [https://doi.org/10.1016/0012-821X\(93\)90010-7](https://doi.org/10.1016/0012-821X(93)90010-7).

- Richter K, Walker RJ, and Warren PH (2000).** Significance of highly siderophile elements and osmium isotopes in the lunar and terrestrial mantle. In: Canup RM, Richter K (eds.) *Origin of the Earth and Moon*. Univ. Arizona Press, Tuscon, pp. 291–322.
- Ripley EM, Shafer P, Li C, and Hauck SA (2008).** Re–Os and O isotopic variations in magnetite from the contact zone of the Duluth Complex and the Biwabik Iron Formation, northeastern Minnesota, *Chemical Geology* 249 (1–2), pp.213–226, ISSN 0009-2541, doi: <https://doi.org/10.1016/j.chemgeo.2007.12.010>.
- Robbins LJ, Funk SP, Flynn SL, Tyler WJ, Li Z, Lalonde SV, Rostron BJ, Smith AJB, Beukes NJ, de Kock MO, Heaman LM, Alessi DS, and Konhauser KO (2019).** Hydrogeological constraints on the formation of Palaeoproterozoic banded iron formations. *Nature Geoscience* 12 (7), pp. 558–563.
- Robbins LJ, Lalonde SV, Planavsky NJ, Partin CA, Reinhard CT, Kendall B, Scott C, Hardisty DS, Gill BC, Alessi DS, Dupont CI, Saito MA, Crowe SA, Poulton SW, Bekker A, Lyons TW, Konhauser KO (2016).** Trace elements at the intersection of marine biological and geochemical evolution. *Earth- Science Reviews* 163, pp. 323–348.
- Robbins LJ, Swanner ED, Lalonde SV, Eickhoff M, Paranich ML, Reinhard CT, Peacock CL, Kappler A, and Konhauser KO (2015).** Limited Zn and Ni mobility during simulated iron formation diagenesis. *Chemical Geology* 402, pp. 30–39.
- Rooney AD, Chew DM, and Selby D (2011).** Re–Os geochronology of the Neoproterozoic-Cambrian Dalradian Supergroup of Scotland and Ireland: implications for Neoproterozoic stratigraphy, glaciations and Re–Os systematics. *Precambrian Research* 185, pp. 202–214.
- Rooney AD, Macdonald FA, Strauss JV, Dudás FÖ, Hallmann C, and Selby D (2014).** Re–Os geochronology and coupled Os–Sr isotope constraints on the Sturtian snowball Earth. *Proceedings of the National Academy of Sciences of the United States* 111 (1), pp. 51–56, doi: <https://doi.org/10.1073/pnas.1317266110>.
- Rooney AD, Strauss JV, Brandon AD, and Macdonald FA (2015).** A Cryogenian chronology: two long-lasting synchronous Neoproterozoic glaciations. *Geology* 43 (5), pp. 459–462.
- Sansjofre P, Ader M, Trindade R, Elie M, Lyons J, Cartigny P, and Nogueira ACR (2011)** A carbon isotope challenge to the snowball Earth. *Nature* 478, pp. 93–96. doi: <https://doi.org/10.1038/nature10499>
- Sato K, and Siga Jr. O (2000).** Evidence of the superproduction of the continental crust during Paleoproterozoic in South American Platform: Implications regarding the interpretative value of the Sm–Nd model ages. *Revista Brasileira de Geociências* 30, pp. 126–129.
- Savard D, Barnes S-J, and Meisel T (2010).** Comparison between Nickel-Sulfur Fire Assay Te Co-precipitation and Isotope Dilution with High-Pressure Asher Acid Digestion for the Determination of Platinum-Group Elements, Rhenium and Gold. *Geostandards and Geoanalytical Research* 34, pp. 281 - 291. doi:10.1111/j.1751-908X.2010.00090.x.
- Schneider G (1984).** Zur Mineralogie und Lagerstättenbildung der Mangan- und Eisenerzvorkommen des Urucum-Distriktes (Mato Grosso do Sul, Brasilien). Johann Wolfgang Goethe-Universität Frankfurt, *Frankfurter Geowissenschaftliche Arbeiten, Serie C Mineralogie*.
- Schreck PC (1984).** Geochemische Klassifikation und Petrogenese der Manganerze des Urucum-Distriktes bei Corumba (Mato Grosso do Sul, Brasilien). Johann Wolfgang Goethe-Universität Frankfurt, *Frankfurter Geowissenschaftliche 1311 Arbeiten, Serie C Mineralogie*.
- Schulz KJ and Cannon WF (2007).** The Penokean orogeny in the Lake Superior region. *Precambrian Research* 157, pp. 4–25.
- Schulz T, Koeberl C, Luguet A, van Acken D, Mohr-Westheide T, Ozdemir S, and Reimold WU (2017).** New constraints on the Paleoproterozoic meteorite bombardment of the Earth—geochemistry and Re–Os isotope signatures of spherule layers in the BARB5 drill core from the Barberton Greenstone Belt, South Africa. *Geochimica et Cosmochimica Acta* 211, pp.322–340.
- Schulz T, Viehmann S, Hezel D, Koeberl C, and Bau M (2021).** Highly Siderophile Elements and Coupled Fe–Os Isotope Signatures in the Temagami Iron Formation, Canada: Possible Signatures of Neoproterozoic Seawater Chemistry and Earth's Oxygenation History. *Astrobiology* 21, pp. 924–939. doi: <https://doi.org/10.1089/ast.2020.2311>
- Scott C, Wing BA, Bekker A, Planavsky NJ, Medvedev P, Bates SM, Yun M, and Lyons TW (2014).** Pyrite multiple-sulfur isotope evidence for rapid expansion and contraction of the early Paleoproterozoic seawater sulfate reservoir. *Earth and Planetary Science Letters* 389, pp. 95–104.
- Sekine Y, Suzuki K, Senda R, Goto KT, Tajika E, Tada R, Goto K, Yamamoto S, Ohkouchi N, Ogawa NO, and Maruoka T (2011).** Osmium evidence for synchronicity between a rise in atmospheric oxygen and Palaeoproterozoic deglaciation. *Nature Communications* 2: 502. doi: <https://doi.org/10.1038/ncomms1507>

- Seward TM (1989).** The hydrothermal chemistry of gold and its implication for ore formation: boiling and conductive cooling as examples. *Economic Geology Monograph Series* 6, pp. 398–404. doi: <https://doi.org/10.5382/Mono.06.31>
- Sharma M, Papanastassiou DA, and Wasserburg GJ (1997).** *The concentration and isotopic composition of osmium in the oceans.* *Geochimica et Cosmochimica Acta* 61 (16). pp. 3287–3299. ISSN 0016-7037. doi: 10.1016/S0016-7037(97)00210-X.
- Shen JJ, Papanastassiou DA, and Wasserburg GJ (1996).** Precise Re–Os determinations and systematics of iron meteorites. *Geochimica et Cosmochimica Acta* 60, pp. 2887–2900.
- Shirey SB, and Walker RJ (1995).** Carius tube digestion for low blank rhenium-osmium analysis. *Analytical Chemistry* 34, pp. 2136–2141.
- Siebert LC, Kramers JD, Meisel Th, Morel Ph, and Nögler ThF (2005).** PGE, Re–Os, and Mo isotope systematics in Archean and early Proterozoic sedimentary systems as proxies for redox conditions of the early Earth, *Geochimica et Cosmochimica Acta* 69 (7), pp. 1787–1801. <https://doi.org/10.1016/j.gca.2004.10.006>.
- Simonson BM (2003).** Origin and evolution of large Precambrian iron formations. In: Chan MA, Archer AW (eds.). *Extreme Depositional Environments: Mega End Members in Geologic Time*, Geological Society of America Special Papers 370, pp. 231–244. Boulder, CO: Geological Society of America. doi: 10.1130/0-8137-2370-1.231
- Skomurski FN, Ilton ES, Engelhard MH, Arey BW, and Rosso KM (2011).** Heterogeneous reduction of U<sup>6+</sup> by structural Fe<sup>2+</sup> from theory and experiment. *Geochimica et Cosmochimica Acta* 75 (22), pp. 7277–7290. ISSN 0016-7037, doi: <https://doi.org/10.1016/j.gca.2011.08.006>.
- Slack JF, and Cannon WF (2009).** Extraterrestrial demise of banded iron formations 1.85 billion years ago. *Geology* 37, pp. 1011–1014.
- Slack, JF, Grenne T, Bekker A, Rouxel OJ, and Lindberg PA (2007).** Suboxic deep seawater in the late Paleoproterozoic: evidence from hematitic chert and iron formation related to seafloor-hydrothermal sulfide deposits, central Arizona, USA. *Earth and Planetary Science Letters* 255, pp. 243–256.
- Smith AJB, Beukes NJ, and Gutzmer J (2013).** The composition and depositional environments of Mesoarchean iron formations of the West Rand Group of the Witwatersrand Supergroup, South Africa. *Economic Geology* 108, pp. 111–134.
- Smoliar MI, Walker RJ, and Morgan JW (1996).** Re–Os ages of Group IIA, IIIA, IVA and IVB iron meteorites. *Science* 271, pp. 1099–1102.
- Søgaard EG, Medenwaldt R, and Abraham-Peskir JV (2000).** Conditions and rates of biotic and abiotic iron precipitation in selected Danish freshwater plants and microscopic analysis of precipitate morphology. *Water Research* 34, pp. 2675–2682.
- Southam G, Lengke MF, Fairbrother L, and Reith F (2009).** The biogeochemistry of gold. *Elements* 5, pp. 303–307.
- Sperling EA, Rooney AD, Hays L, Sergeev VN, Vorobéva NG, Sergeeva ND, Selby D, Johnston DT, and Knoll AH (2014).** Redox heterogeneity of subsurface waters in the Mesoproterozoic ocean. *Geobiology* 12, pp. 373–386, doi: <https://doi.org/10.1111/gbi.12091>
- Spray JG, Kelley SP, and Dence MR (1999).** The Strangways impact structure, Northern Territory, Australia: Geological setting and laser probe <sup>40</sup>Ar/<sup>39</sup>Ar geochronology. *Earth and Planetary Science Letters* 172, pp.199–211.
- Stein H, and Hannah J (2014).** Rhenium–Osmium Geochronology: Sulfides, Shales, Oils, and Mantle. In: Rink W, Thompson J (eds). *Encyclopedia of Scientific Dating Methods*. Springer, Dordrecht. doi: [https://doi.org/10.1007/978-94-007-6326-5\\_36-1](https://doi.org/10.1007/978-94-007-6326-5_36-1)
- Stein HJ and Hannah JL (2015).** Rhenium-osmium geochronology: sulfides, shales, oils and mantle. In: Rink WJ, Thompson JJ (eds.). *Encyclopedia of Scientific Dating Methods*, Springer, Netherlands, pp. 707–723.
- Stern JC and Wieman ST (2021).** Traditional Stable Isotope Geochemistry. In: Alderton D, Elias SA (eds.). *Encyclopedia of Geology (Second Edition)*, Academic Press, pp. 100–113. ISBN 9780081029091, doi: <https://doi.org/10.1016/B978-0-08-102908-4.00116-8>
- Stern RJ, Mukherjee SK, Miller NR, Ali K, and Johnson PR (2013).** ~750 Ma banded iron formation from the Arabian-Nubian Shield—implications for understanding Neoproterozoic tectonics, volcanism, and climate change. *Precambrian Research* 239, pp. 79–94.
- Straub KL and Buchholz-Cleven BEE (1998).** Enumeration and detection of anaerobic ferrous iron-oxidizing, nitrate-reducing bacteria from diverse European sediments. *Applied Environmental Microbiology* 64, pp. 4846–4856.
- Straub KL, Benz M, Schink B, and Widdel F (1996).** Anaerobic, nitrate-dependent microbial oxidation of ferrous iron. *Applied Environmental Microbiology* 62, pp. 1458–1460.

- Suzuki K and Kato Y (2003).** Re-Os isotope systematics of 3.8 Ga banded iron formation and cherts from Isua supracrustal belt, SW Greenland. *Geochimica et Cosmochimica Acta Supplement* 67:459.
- Tagle R and Berlin J (2008).** A database of chondrite analyses including platinum group elements, Ni, Co, Au, and Cr: implications for the identification of chondritic projectiles. *Meteoritic & Planetary Science* 43, pp. 541–559.
- Tassinari CCG, Bettencourt JS, Geraldes MC, Macambira MJB, Lafon JM (2000).** The Amazon craton. In: Cordani UG, Milani EJ, Thomaz-Filho A, Campos DA (eds.), *Tectonic Evolution of South America. 31st International Geological Congress, Rio de Janeiro, Brazil*, pp. 41–95.
- Taylor KG, Simo JA, Yakum D, and Leckie DA (2002).** Stratigraphic significance of ooidal ironstones from the Cretaceous western interior seaway: The Peace River Formation, Alberta, Canada, and the Castlegate Sandstone, Utah, U.S.A. *Journal of Sedimentary Research* 72, pp. 316–327.
- Teixeira JBG, Misi A, and da Glória da Silva M (2007).** Supercontinent evolution and the Proterozoic metallogeny of South America. *Gondwana Research* 11 (3), pp. 346–361. ISSN 1342-937X, doi: <https://doi.org/10.1016/j.gr.2006.05.009>
- Tejada MLG, Suzuki K, Kuroda J, Coccioni R, Mahoney JJ, Ohkouchi N, Sakamoto T, and Tatsumi Y, (2009).** Ontong Java Plateau eruption as a trigger for the early Aptian oceanic anoxic event. *Geology* 37, pp. 855–858.
- Tohver E, Trindade RIF, Solum JG, Hall CM, Riccomini C, and Nogueira AC (2010).** Closing the Clymene Ocean and bending a Brasiliano belt: Evidence for the Cambrian formation of Gondwana, southeast Amazon craton. *Geology* 38 (3), pp. 267–270.
- Tréguer P, Nelson DM, Van Bennekom AJ, DeMaster DJ, Leynaert A, and Quéguiner B (1995).** The silica balance in the world ocean: a reestimate. *Science* 268, pp. 375–379.
- Trendall A and Blockley J (1970).** The iron formations of the Precambrian Hamersley Group, Western Australia with special reference to the associated crocidolite. *Geological Survey of Western Australia Bulletin* 119. Perth: Geological Survey of Western Australia.
- Tripathy GR and Singh SK (2015).** Re-Os depositional age for black shales from the Kaimur Group, Upper Vindhyan, India. *Chemical Geology* 413, pp. 63–72. doi: <https://doi.org/10.1016/j.chemgeo.2015.08.011>
- Trompette R (1994).** Geology of Gondwana (2000–500 Ma). Pan-African-Brasiliano aggregation of South America and Africa, Rotterdam, Balkema, pp. 350.
- Trompette R, Alvarenga CJS, and Walde D (1998).** Geological evolution of the Neoproterozoic Corumbá graben system (Brazil). Depositional context of the stratified Fe and Mn ores of the Jacadigo Group. *Journal of South American Earth Sciences* 11, pp. 587–597.
- Tsikos H, Beukes NJ, Moore JM, and Harris C (2003).** Deposition, diagenesis, and secondary enrichment of metals in the Paleoproterozoic Hotazel Iron Formation, Kalahari manganese field, South Africa. *Economic Geology* 98, pp. 1449–1462.
- Turgeon SC, and Creaser RA (2008).** Cretaceous oceanic anoxic event 2 triggered by a massive magmatic episode. *Nature* 454, pp. 323–326.
- Urban H, Stribrny B, and Lippolt HJ (1992).** Iron and manganese deposits of the Urucum District, Mato Grosso do Sul, Brazil. *Economic Geology* 87, pp. 1375–1392.
- Ussami N, Shiraiwa S, and Dominguez JML (1999).** Basement reactivation in a sub-Andean foreland flexural bulge: The Pantanal wetland, SW Brazil, *Tectonics* 18 (1), pp. 25–39. doi:[10.1029/1998TC900004](https://doi.org/10.1029/1998TC900004).
- van Acken D, Thomson D, Rainbird RH, and Creaser RA (2013).** Constraining the depositional history of the Neoproterozoic Shaler Supergroup, Amundsen Basin, NW Canada: Rhenium-osmium dating of black shales from the Wynniatt and Boot Inlet Formations. *Precambrian Research* 236, pp. 124–131.
- van Leeuwen P and Graaf JL (1987).** The Urucum-Mutum iron and manganese deposits, Mato Grosso do Sul, Brazil, and Santa Cruz, Bolivia. Part 1-The region's potential as an economic source of iron and manganese: *Geologie en Mijnbouw* 65, pp. 317–325.
- Viehmann S, Bau M, Bühn B, Dantas EL, Andrade FRD, and Walde DHG (2016).** Geochemical characterisation of Neoproterozoic marine habitats: Evidence from trace elements and Nd isotopes in the Urucum iron and manganese formations, Brazil. *Precambrian Research* 282, pp. 74–96. ISSN 0301-9268, doi: <https://doi.org/10.1016/j.precamres.2016.07.006>.
- Viehmann S, Bau M, Hoffmann JE, and Muenker C (2015a).** Geochemistry of the Krivoy Rog Banded Iron Formation, Ukraine, and the impact of peak episodes of increased global magmatic activity on the trace element composition of Precambrian seawater. *Precambrian Research* 270, pp. 165–180. doi: <http://dx.doi.org/10.1016/j.precamres.2015.09.015>.
- Viehmann S, Bau M, Smith AJB, Beukes NJ, Dantas EL, and Bühn B (2015b).** The reliability of ~2.9 Ga old Witwatersrand banded iron formations (South Africa) as archives for Mesoarchean seawater: Evidence

- from REE and Nd isotope systematics, *Journal of African Earth Sciences* 111, pp. 322-334. ISSN 1464-343X, doi: <https://doi.org/10.1016/j.jafrearsci.2015.08.013>.
- Viehmann S, Hoffmann EJ, Münker C, and Bau M (2013).** Decoupled Hf-Nd isotopes in Neoproterozoic seawater reveal weathering of emerged continents. *Geology* 42 (2): pp.115–118. doi: <https://doi.org/10.1130/G35014.1>
- Viehmann S, Hoffmann JE, Münker C, and Bau M (2014).** Decoupled Hf-Nd isotopes in Neoproterozoic seawater reveal weathering of emerged continents. *Geology* 42 (2), pp. 115–118. doi: <https://doi.org/10.1130/G35014.1>
- Völkening J, Walczyk T, and Heumann KG (1991).** Osmium isotope ratio determinations by negative thermal ionization mass spectrometry. *International Journal of Mass Spectrometry and Ion Processes* 105 (2), pp. 147-159. ISSN 0168-1176, doi: [https://doi.org/10.1016/0168-1176\(91\)80077-Z](https://doi.org/10.1016/0168-1176(91)80077-Z).
- Walde DHG (1981).** Die Mangan- und Eisenvorkommen von Urucum, Mato Grosso, Brasilien – Erste Ergebnisse und ein weiteres Programm. *Zentralblatt für Geologie und Paläontologie* 1, pp. 505–513.
- Walde DHG (1988).** Das Proterozoische Paraguay-Araguaia orogen in West-Brasilien, ausgehend von untersuchungen im Raum Corumbá. *Habilitationsschrift*, unpublished, Albert-Ludwigs University, Freiburg, p. 122.
- Walde DHG and Hagemann S (2007).** The Neoproterozoic Urucum/Mutún Fe and Mn deposits in W-Brazil/SE-Bolivia: assessment of ore deposit models. *Zeitschrift der Deutschen Gesellschaft für Geowissenschaften* 158, pp. 45-55. doi: 10.1127/1860-1804/2007/0158-0045.
- Walde DHG, Gierth E, and Leonardos OH (1981).** Stratigraph and mineralogy of the manganese ores of Urucum, Mato Grosso, Brazil. *Geologie Rundschau* 70, pp. 1077-1085.
- Walker J (1984).** Suboxic diagenesis in banded iron formations. *Nature* 309, pp. 340–342. doi: <https://doi.org/10.1038/309340a0>
- Wang C, Konhauser KO, and Zhang L (2015).** Depositional environment of the Paleoproterozoic Yuanjiaocun banded iron formation in Shanxi Province, China. *Economic Geology* 110, pp. 1515–1539.
- Wang C, Konhauser KO, Zhang L, Zhai M, and Li W (2016).** Decoupled sources of the 2.3-2.2 Ga Yuanjiaocun banded iron formation: implications for the Nd cycle in Earth's early oceans. *Precambrian Research* 280, pp. 1–13.
- Wang X, Planavsky NJ, Hofmann A, Saupe EE, De Corte BP, Philippot P, LaLonde SV, Jemison NE, Zou H, Ossa Ossa F, Rybacki K, Alfimova N, Larson MJ, Tsikos H, Fralick PW, Johnson TM, Knudsen AC, Reinhard CT, and Konhauser KO (2018).** A Mesoarchean shift in uranium isotope systematics. *Geochimica et Cosmochimica Acta* 238, pp. 438-452. doi: <https://doi.org/10.1016/j.gca.2018.07.024>
- Waters C, Peucker-Ehrenbrink B and Hoffman P (2009).** Platinum Group Element and Re-Os Isotope Systematics of Cryogenian Glacial Terminations. American Geophysical Union. *AGU Fall Meeting Abstracts*. abstract #U13A-0047.
- Wei W, Kläbe R, Ling H-F, Huang F, and Frei R (2020).** Biogeochemical cycle of chromium isotopes at the modern Earth's surface and its applications as a paleo-environment proxy. *Chemical Geology* 541, 119570.
- White WM (2015).** Chapter 2 - Decay systems and geochronology I. In: White WM (ed.), *Isotope Geochemistry, First Edition*. pp. 32-69. Wiley-Blackwell, ISBN 978-0-470-65670-9
- Widdel F, Schnell S, Heising S, Ehrenreich A, Assmus B, and Schink B (1993).** Ferrous iron oxidation by anoxygenic phototrophic bacteria. *Nature* 362, pp. 834–836.
- Williams GE and Schmidt PW (2020).** Dating the Acraman asteroid impact, South Australia: the case for deep drilling the 'hot shock' zone of the central uplift, *Australian Journal of Earth Sciences* 68 (3), pp. 355-367. doi: 10.1080/08120099.2020.1808066
- Xu DR, Wang ZL, Chen HY, Hollings P, Jansen NH, Zhang ZC, and Wu CJ, (2013).** Petrography and geochemistry of the Shilu Fe–Co–Cu ore district, South China: Implications for the origin of a Neoproterozoic BIF system. *Ore Geology Reviews* 57, pp. 322–350.
- Xu G, Hannah JL, Stein HJ, Bingen B, Yang G, Zimmerman A, Weitschat W, Mørk A, and Weiss HM (2009).** Re-Os geochronology of Arctic black shales to evaluate the Anisian-Ladinian boundary and global faunal correlations. *Earth and Planetary Science Letters* 288, pp. 581-587.



## 8 Appendix

### Appendix 8-1 – Anion exchange chemistry

<b>1<sup>st</sup> Stage</b>	
<b><u>ANION COLUMN</u></b>	Resin Amount 1ml
<u>Resin Cleaning</u>	10 ml H <sub>2</sub> O 10 ml 6M HNO <sub>3</sub> 10 ml conc HNO <sub>3</sub> 2 ml H <sub>2</sub> O 10 ml conc HCl 2 ml H <sub>2</sub> O
Equilibration	2 ml 1M HCl 2 ml 0.5M HCl
<u>Load sample</u>	<b><u>10 ml 0.5M HCl</u></b> 5 ml 1M HCl 2 ml 0.8M HNO <sub>3</sub> 2 ml 0.8M HNO <sub>3</sub>
<u>Collect Re-Ir-Pt-Ru</u>	<b><u>15 ml conc HNO<sub>3</sub></u></b> 2 ml H <sub>2</sub> O
<u>Collect Pd</u>	<b><u>15 ml conc HNO<sub>3</sub></u></b>
<u>Collect Pd</u>	<b><u>10 ml conc HNO<sub>3</sub></u></b>
<u>Collect Pd</u>	<b><u>10 ml conc HNO<sub>3</sub></u></b>
	Dry down both cuts and redissolved in 1 ml 1M HCl
<b>2<sup>nd</sup> Stage</b>	
<b><u>LN-Spec COLUMN</u></b>	
<u>Resin Cleaning</u>	4 ml H <sub>2</sub> O 4 ml 6M HCl 4 ml 6M HCl 4 ml 2M HF 4 ml 6M HCl 4 ml 2M HF 4 ml H <sub>2</sub> O
Equilibration	4 ml 1M HCl
<u>Load Pd and Collect Pd</u>	<b><u>1 ml 1M HCl</u></b>
<u>Collect Pd</u>	<b><u>4 ml 1M HCl</u></b>
<u>Load Ir-Pt-Re-Ru and collect</u>	<b><u>1 ml 1M HCl</u></b>
<u>Collect Ir-Pt-Re-Ru</u>	<b><u>5 ml 1M HCl</u></b> 4 ml 2M HF
Cleaning	4 ml 2M HF 4 ml 6M HCl 4 ml 2M HF 4 ml 6M HCl 4 ml 2M HF 4 ml 6M HCl

**Appendix 8-1:** Recipes for the 1<sup>st</sup> and 2<sup>nd</sup> stage anion exchange column separation. From Chu et al. (2014).

### Appendix 8-2 – Mean concentrations of HSE in various reservoirs.

Reservoir	Re (ppb)	Os (ppb)	Ir (ppb)	Pt (ppb)	Ru (ppb)	Pd (ppb)	<sup>187</sup> Re/ <sup>188</sup> Os	<sup>187</sup> Os/ <sup>188</sup> Os
Upper continental crust (UCC) <sup>(1)</sup>	0.198	0.031	0.022	0.51	0.21	0.52	34.5	1.4
Terrestrial Mantle <sup>(2)</sup>	0.35	3.9	3.5	7.6	1.2	7.1	0.4253	0.1296
CI Chondrite <sup>(3)</sup>	38.1	460.5	430.6	873.5	637.4	570.5	0.3921	0.1262
Modern Seawater <sup>(4)</sup>	0.007	0.00001	0.000003	0.00007	0.005	0.00066	-	-
Moodies Group (WR) <sup>(5)</sup>	0.047	0.016	0.011	0.053	-	0.078	-	0.3466
Temagami BIF (chert) <sup>(6)</sup>	0.025	0.002	0.003	0.05	-	-	77.3	2.381
Temagami BIF (magnetite) <sup>(6)</sup>	0.062	0.01	0.004	0.016	-	-	34	1.293

<sup>(1)</sup>Peucker-Ehrenbrink and Jahn (2001)

<sup>(2)</sup>Becker et al. (2006)

<sup>(3)</sup>Horan et al. (2003)

<sup>(4)</sup>Re and Os concentrations from Stein and Hannah (2014), Pt concentration from Mashio et al. (2017), Ir concentration from I et al. (2007), Ru concentration from Koide et al. (1987), and Pd concentrations from Lee (1983).

<sup>(5)</sup>Siebert et al. (2005)

<sup>(6)</sup>Schulz et al. (2021)

**Appendix 8-2:** Estimates of HSE abundance in various HSE reservoirs and BIFs.

### Appendix 8-3 – Major and trace element concentrations of Urucum samples

sample-ID type	Pure IF				Impure IF								
	UR51_20	UR62_15	UR62_17	UR62_25	UR51_10	UR51_26	UR51_30	UR51_35	UR51_40	UR51_47	UR51_70	UR62_11	UR62_25
	IF	IF	IF	IF	Mn-rich BIF	IF	IF	IF arkose	IF	IF	IF	IF	IF
<i>wt%</i>													
Al <sub>2</sub> O <sub>3</sub>	0.09	0.06	0.14	0.08	1.51	0.26	0.31	2.70	2.31	2.85	0.41	0.12	0.15
CaO	0.10	0.17	0.10	0.18	0.36	0.04	0.02	0.43	0.16	0.17	0.06	0.06	0.06
Cr <sub>2</sub> O <sub>3</sub>	<0.01	<0.01	<0.01	<0.01	<0.01	0.01	<0.01	0.01	0.01	0.01	<0.01	<0.01	<0.01
FeO <sub>t</sub>	91.4	70.5	71.4	62.5	41.7	72.5	79.7	62.3	67.2	73.5	86.8	73.8	62.0
Fe <sub>2</sub> O <sub>3t</sub>	101.6	78.4	79.4	69.5	46.3	80.6	88.6	69.3	74.7	81.7	96.5	82.0	68.9
MgO	0.01	0.01	0.01	0.01	0.07	2.60	0.01	0.05	0.08	0.61	0.01	0.01	0.02
MnO	0.03	0.02	0.02	0.02	7.02	0.08	0.17	1.44	1.01	6.65	0.05	0.01	0.21
Na <sub>2</sub> O	<0.01	0.01	0.01	<0.01	0.02	0.01	0.01	0.02	0.60	0.04	<0.01	0.01	0.01
P <sub>2</sub> O <sub>5</sub>	0.17	0.06	0.08	0.07	0.98	0.11	0.10	0.37	0.22	0.14	0.10	0.05	0.08
V <sub>2</sub> O <sub>5</sub>	0.01	0.00	0.01	0.01	0.01	0.01	0.02	0.02	0.02	0.02	0.01	0.01	0.01
ZnO	0.01	0.01	0.01	0.01	0.01	0.01	0.01	0.01	0.01	0.01	0.01	0.01	0.01
Fe/Mn	3193.0	3814	3347	3149	5.96	911	464	43.3	157	11.1	1786	7172	301
<i>mg/kg</i>													
Li	0.885	2.54	2.13	0.896	6.25	0.993	0.836	25.7	4.51	16.7	0.339	0.856	3.27
Be	0.446	0.377	0.322	0.274	1.25	0.262	0.482	1.04	0.499	0.381	0.46	0.241	0.34
Sc	0.825	3.70	1.74	2.93	10.0	2.90	3.66	12.7	2.64	4.13	2.24	1.33	1.69
Ti	216.0	70.9	58.2	118	814	136	331	1100	1590	1600	356	98.0	104
Co	0.349	0.484	0.329	0.73	123	1.23	6.96	59.1	75.6	119	0.657	0.178	1.02
Ni	2.39	1.68	1.42	2.52	43.2	2.43	6.46	50.1	60.7	115	4.18	2.26	3.77
Rb	0.164	0.39	0.385	0.135	2.73	0.386	1.29	3.96	4.7	40.1	0.548	0.408	0.309
Sr	38.8	14.5	33.4	21.9	140	19.2	54.2	90.5	81.8	183	134	35.4	22
Y	8.84	30.3	17.6	23	111	13.9	17.3	11.3	10.6	20	23.5	8.82	8.9
Zr	4.95	2.91	3.81	3.51	44.2	9.68	43.9	53.5	85.0	45.2	10.9	4.13	5.37
Nb	0.507	0.322	0.342	0.377	3.87	0.767	1.58	6.27	9.17	8.51	1.42	0.457	0.515
Mo	0.766	0.677	0.788	0.665	0.750	0.727	1.52	1.39	1.03	1.00	0.746	0.957	0.860
Cs	0.0135	0.0724	0.0804	0.027	0.191	0.0561	0.243	2.11	0.539	0.841	0.0492	0.137	0.0618
Ba	17.3	55.8	117	54.7	637	59.2	207	209	44.4	262	60	102	55.6
La	2.04	8.29	8.72	15.2	17.1	4.04	9.85	8.72	13.6	11.6	7.91	2.58	7.17
Ce	2.55	7.37	8.73	13.0	17.2	5.26	14.6	15.1	27.1	29.2	14.7	4.36	8.57
Pr	0.542	1.46	1.65	2.17	4.62	0.875	2.3	2.63	4.19	4.29	1.98	0.706	1.54
Nd	2.41	5.35	6.24	7.18	17.5	3.37	9.08	10.6	15.8	17.8	8.25	2.89	5.92
Sm	0.564	1.09	1.18	1.32	3.25	0.717	1.74	2.5	3.03	4.22	1.73	0.639	1.03
Eu	0.136	0.279	0.277	0.296	0.639	0.164	0.359	0.591	0.637	0.885	0.429	0.158	0.22
Gd	0.816	1.80	1.55	1.69	3.03	0.976	1.86	2.59	2.66	4.39	2.41	0.899	1.08
Tb	0.123	0.318	0.232	0.289	0.432	0.168	0.273	0.373	0.356	0.647	0.395	0.138	0.183
Dy	0.912	2.66	1.85	2.26	4.82	1.32	2.05	2.22	2.1	3.97	3.07	1.07	1.37
Ho	0.218	0.719	0.457	0.588	3.03	0.327	0.489	0.409	0.392	0.769	0.71	0.246	0.288
Er	0.74	2.61	1.55	2.16	9.15	1.14	1.68	1.17	1.23	2.31	2.27	0.81	0.906
Tm	0.106	0.377	0.212	0.304	0.996	0.173	0.247	0.145	0.181	0.325	0.303	0.111	0.122
Yb	0.787	2.90	1.62	2.30	5.95	1.47	2.03	0.949	1.33	2.31	2.26	0.838	0.976
Lu	0.125	0.491	0.267	0.383	0.719	0.265	0.36	0.139	0.212	0.335	0.357	0.135	0.153
Hf	0.0453	0.0423	0.0726	0.0379	0.847	0.173	0.602	1.29	1.87	0.951	0.231	0.0426	0.0973
Ta	-	-	-	-	0.138	-	-	0.125	0.322	0.348	0.0572	0.0104	-
W	0.283	0.23	0.204	0.127	1.39	0.291	0.374	1.38	1.28	2.81	0.246	0.14	0.185
Pb	0.376	0.533	0.477	2.26	1.49	1.19	1.99	2.35	2.13	4.98	0.724	0.773	0.475
Th	0.222	0.239	0.111	0.552	2.18	0.426	1.22	1.97	4.00	4.02	0.839	0.234	0.242
U	0.059	0.0773	0.133	0.0596	0.371	0.101	0.176	0.113	0.106	0.0897	0.128	0.0691	0.444

**Appendix 8-3:** Major and trace element concentrations of pure and impure IF samples used in this study. The characterisation of samples into pure and impure is based on REY-analysis of Viehmann et al. (2016). From Viehmann et al. (2016).

**Appendix 8-4 – Major and trace element concentrations of Urucum samples**

sample-ID type	Mn2					Mn1			chert
	UR51_14 Mn2	UR51_15 Mn2	UR51_16 Mn2 ark	UR51_45 Mn1 (B)	UR51_51 Mn1 ark (A)	UR51_53 Mn1 ark (A)	UR51_55 Mn1 (B)	UR51_56 Mn1 (B)	UR62_30 chert
<i>wt%</i>									
Al2O3	0.43	0.74	0.57	0.66	0.73	1.95	1.26	2.78	0.20
CaO	0.41	0.23	0.43	0.15	0.42	0.44	0.05	0.05	0.14
Cr2O3	<0.01	<0.01	0.01	<0.01	<0.01	<0.01	<0.01	0.01	<0.01
FeO <sub>t</sub>	8.07	13.64	22.90	21.4	4.73	3.63	35.5	34.0	13.1
Fe2O3 <sub>t</sub>	8.96	15.15	25.45	23.7	5.26	4.03	39.5	37.7	14.5
MgO	0.11	0.14	2.19	0.08	0.13	0.22	0.29	0.23	0.06
MnO	77.0	67.9	64.2	62.5	78.6	78.2	37.8	38.0	0.77
Na2O	0.08	0.09	0.06	0.21	0.33	0.17	0.32	1.27	0.00
P2O5	0.47	0.68	0.59	0.32	0.40	0.42	0.10	0.07	0.15
V2O5	0.06	0.06	0.05	0.06	0.06	0.07	0.04	0.04	<0.01
ZnO	0.01	0.01	0.01	0.01	0.01	0.01	0.01	0.01	<0.01
Fe/Mn	0.105	0.202	0.358	0.343	0.0604	0.0465	0.942	0.898	17.0
<i>mg/kg</i>									
Li	14.2	8.30	19.0	13.1	17.8	11.3	17.2	10.2	8.92
Be	3.39	11.7	0.988	1.06	0.577	0.841	1.18	1.43	0.745
Sc	8.93	6.77	10.2	1.15	8.45	7.89	1.19	0.934	5.65
Ti	489	458	587	947	520	423.0	1570	1350	22.0
Co	241	220	231	263	335	421	185	146	3.72
Ni	29.7	33.7	38.4	61.6	39.3	55.1	61.3	62.6	6.70
Rb	11.4	23.8	4.94	69.6	11.3	29.1	62.4	62.4	0.554
Sr	14.3	13.7	13.4	12.3	331	15.1	12.4	14.4	14.7
Y	23.6	20.0	24.3	14.7	29.7	32.3	9.36	7.97	49.7
Zr	39.7	32.8	51.6	72.6	23.6	18.8	46.5	37.7	6.34
Nb	3.98	4.34	4.71	4.93	3.37	3.07	6.23	8.03	0.0891
Mo	0.269	0.467	0.341	0.692	0.340	0.307	0.906	0.892	0.733
Cs	0.167	0.373	0.107	0.477	0.400	0.637	0.689	0.568	0.0178
Ba	1310	1760	1620	-	872	1220	-	-	302
La	19.3	16.5	17.1	28.0	21.1	24.3	22.6	27.7	3.62
Ce	22.3	29.6	27.9	105	19.1	19.6	55.1	56.9	6.70
Pr	4.34	3.82	3.69	6.83	5.85	6.68	5.37	5.96	0.856
Nd	15.6	13.3	12.9	25.1	21.9	25.4	19.2	19.4	3.75
Sm	3.15	2.48	2.44	6.29	4.76	5.33	3.95	3.37	1.11
Eu	0.603	0.46	0.404	3.62	1.02	1.11	1.71	1.71	0.322
Gd	3.09	2.34	2.27	6.12	4.9	5.45	3.40	2.74	2.56
Tb	0.458	0.347	0.318	0.784	0.769	0.819	0.452	0.376	0.517
Dy	3.02	2.20	2.34	3.97	4.97	5.27	2.41	1.98	4.48
Ho	0.747	0.566	0.795	0.712	1.05	1.10	0.406	0.340	1.17
Er	2.82	2.27	2.77	2.02	3.29	3.55	1.06	0.887	4.12
Tm	0.435	0.374	0.399	0.272	0.482	0.519	0.142	0.105	0.578
Yb	3.6	3.19	3.24	1.94	3.71	3.94	1.05	0.723	4.44
Lu	0.483	0.440	0.408	0.309	0.585	0.64	0.186	0.120	0.740
Hf	0.413	0.363	0.52	1.14	0.426	0.306	1.11	0.938	0.187
Ta	-	-	0.114	0.143	-	-	0.316	0.343	-
W	1.89	1.42	1.88	4.21	2.94	5.54	4.21	4.45	0.116
Pb	1.42	1.93	1.66	113	1.39	2.72	112	19.4	0.206
Th	1.58	1.97	2.10	7.03	1.13	1.66	3.30	2.80	0.274
U	0.228	0.241	0.312	1.07	0.094	0.0895	1.220	0.789	1.14

**Appendix 8-4:** Major and trace element concentrations of Mn1-horizon, Mn2-horizon, and chert samples used in this study. From Viehmann et al. (2016).

**Abstract 8-5 – Urucum hand samples**



**Appendix 8-5:** Hand samples of Urucum samples UR51\_10, UR51\_14, UR51\_15, UR51\_16, and UR51\_20. Selected samples are marked as red. Photos courtesy of Sebastian Viehmann. The brightness of the photos has been adjusted to better highlight band transitions.

**Abstract 8-6 – Urucum hand samples**



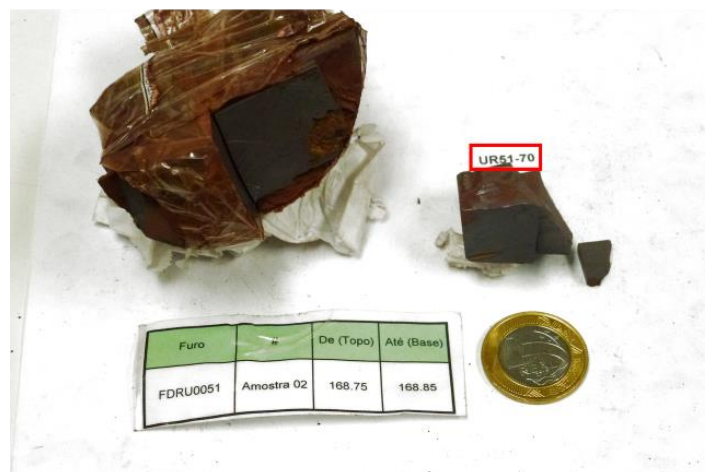
**Appendix 8-6:** Hand samples of Urucum samples UR51\_26, UR51\_30, and UR51\_35. Selected samples are marked as red. Photos courtesy of Sebastian Viehmann. The brightness of the photos has been adjusted to better highlight band transitions.

**Abstract 8-7 – Urucum hand samples**



**Appendix 8-7:** Hand samples of Urucum samples UR51\_40, UR51\_45, UR51\_47, and UR51\_51. Selected samples are marked as red. Photos courtesy of Sebastian Viehmann. The brightness of the photos has been adjusted to better highlight band transitions.

**Abstract 8-8 – Urucum hand samples**



**Appendix 8-8:** Hand samples of Urucum samples UR51\_53, UR51\_55, UR51\_56, and UR51\_51. Selected samples are marked as red. Photos courtesy of Sebastian Viehmann. The brightness of the photos has been adjusted to better highlight band transitions.

**Abstract 8-9 – Urucum hand samples**



**Appendix 8-9:** Hand samples of Urucum samples UR62\_11, UR62\_15, UR62\_17, and UR62\_25. Selected samples are marked as red. Photos courtesy of Sebastian Viehmann. The brightness of the photos has been adjusted to better highlight band transitions.

**Abstract 8-10 – Urucum hand samples**



**Appendix 8-10:** Hand samples of Urucum samples UR62\_30, and UR62\_31. Selected samples are marked as red. Photos courtesy of Sebastian Viehmann.

## Abstract

Iron Formations (IFs) are non-actualistic marine chemical sedimentary rock units that are rich in iron (15-40 wt% Fe) and have precipitated directly from seawater, i.e., directly reflect the geochemical composition of ancient seawater. They have been found on all continents and are known throughout the Precambrian eons. Their formation and genesis has long been of interest, involving anoxic hydrothermally influenced deep waters and inorganic or biological Fe oxidation mechanisms. As IFs have been deposited under an array of environmental settings, they have become popular archives in the study of environmental changes through Earth's early history, such as the progressive oxygenation of the global atmosphere or severe global glaciation events. During the Neoproterozoic (1000 - 538 Ma), Earth underwent a series of glaciation events, with ice sheets appearing in low latitudes. The Urucum iron and manganese formation (IF and Mn-F) in the Neoproterozoic Santa Cruz Formation, Brazil, has proven to be a reliable and robust archive for the late Neoproterozoic period and allows unique insight into the composition of seawater during that time-period. Here I present isotope dilution generated highly siderophile element (HSE) data and Re-Os isotopes data of selected Urucum IF and Mn-F samples. The concentrations of selected HSEs vary from ~33 to ~3450 ppt for Re, from ~3 to ~4380 ppt for Os, from ~4 to ~72 ppt for Ir, from ~120 to ~2200 ppb for Pt, from ~0.04 to ~6 ppt for Ru and from ~0.3 to ~2 ppt for Pd. Iron formation samples show  $^{187}\text{Re}/^{188}\text{Os}$  ratios ranging from 0.89 to 976 and  $^{187}\text{Os}/^{188}\text{Os}$  ratios from 0.14 to 2.20 for  $^{187}\text{Os}/^{188}\text{Os}$ . Manganese formation samples have  $^{187}\text{Re}/^{188}\text{Os}$  ratios from 0.22 to 198 for and  $^{187}\text{Os}/^{188}\text{Os}$  ratios between 0.11 and 2.10. The here measured sample outline the Urucum basement water as a mixture of deep ocean water and a continental flux with a high content of  $\text{Al}_2\text{O}_3$  and Sr, with the ocean water component being characterized by variable but generally high concentrations of Re and Os and the continental flux characterized by uniform but low Re and Os concentrations. A Re-Os isochron of the sample displaying the deep ocean water components yields a regression line that corresponds to an age of  $587.6 \pm 41.9$  Ma (MSWD = 0.63) and an  $(^{187}\text{Os}/^{188}\text{Os})_{\text{initial}}$  ratio of  $0.111 \pm 0.004$ . Concentrations of HSE are comparable to Archean BIFs and modern crustal values, whereas  $(^{187}\text{Os}/^{188}\text{Os})_{\text{initial}}$  ratios are highly unradiogenic and support a strong influence of a mantle-derived source on the Urucum basin water. The final Re-Os age is in good agreement with previous published age data of the Urucum BIF and better refines the deposition age constrictions of the Urucum IF-Mn-F as we directly dated IF and Mn-F samples. A deposition before 590 Ma is further supported, making a relation to the Marinoan glaciation event more likely than to the Glaskiers glaciation.

Eisenformationen (EF) sind nicht-aktualistische marine chemische Sedimentgesteinseinheiten, die reich an Eisen sind (15-40 Gew.-% Fe) und direkt aus dem Meerwasser ausgefällt wurden, d. h. sie spiegeln direkt die geochemische Zusammensetzung des alten Meerwassers wider. Sie wurden auf allen Kontinenten gefunden und sind aus dem gesamten Präkambrium bekannt. Ihre Bildung und Entstehung ist seit langem von Interesse, wobei anoxische, hydrothermal beeinflusste Tiefenwässer und anorganische oder biologische Fe-Oxidationsmechanismen eine Rolle spielen. Da sich EFs unter einer Vielzahl von Umweltbedingungen abgelagert haben, sind sie zu beliebten Archiven bei der Untersuchung von Umweltveränderungen in der frühen Erdgeschichte geworden, wie z. B. der fortschreitenden Sauerstoffanreicherung der Erdatmosphäre oder weitreichenden globalen Vergletscherungen. Während des Neoproterozoikums (1000 - 538 Ma) kam es auf der Erde zu einer Reihe von Vergletscherungen, bei denen in niedrigen Breitengraden Eisschilde auftraten. Die Urucum-Eisen- und -Mangan-Formation (EF und Mn-F) in der neoproterozoischen Santa-Cruz-Formation, Brasilien, hat sich als zuverlässiges und robustes Archiv für das späte Neoproterozoikum erwiesen und ermöglicht einzigartige Einblicke in die Zusammensetzung des Meerwassers während dieses Zeitraums. Hier präsentiere ich durch Isotopenverdünnung gewonnene Daten zu hoch siderophilen Elementen (HSE) und Re-Os-Isotopen ausgewählter Urucum EF- und Mn-F-Proben. Die Konzentrationen ausgewählter HSEs variieren von ~33 bis ~3450 ppt für Re, von ~3 bis ~4380 ppt für Os, von ~4 bis ~72 ppt für Ir, von ~120 bis ~2200 ppb für Pt, von ~0.04 to ~6 ppt für Ru and from ~0.3 to ~2 ppt für Pd. Die Eisenbildungsproben weisen  $^{187}\text{Re}/^{188}\text{Os}$ -Verhältnisse von 0,89 bis 976 und  $^{187}\text{Os}/^{188}\text{Os}$ -Verhältnisse von 0,14 bis 2,20 auf. Die Proben der Manganformation weisen  $^{187}\text{Re}/^{188}\text{Os}$ -Verhältnisse von 0,22 bis 198 und  $^{187}\text{Os}/^{188}\text{Os}$ -Verhältnisse zwischen 0,11 und 2,10 auf. Die hier gemessene Probe reflektieren das Urucum-Grundwasser als eine Mischung aus tiefem Ozeanwasser und einem kontinentalen Fluss mit einem hohen Gehalt an  $\text{Al}_2\text{O}_3$  und Sr, wobei die Ozeanwasserkomponente durch variable, aber im Allgemeinen hohe Konzentrationen von Re und Os und der kontinentale Fluss durch einheitlich geringe Re- und Os-Konzentrationen gekennzeichnet ist. Eine Re-Os-Isochrone der Probe, das die tiefen Ozeanwasserkomponenten zeigt, ergibt eine Regressionslinie, welche einem Alter von  $587,6 \pm 41,9$  Ma (MSWD = 0,63) und einem  $(^{187}\text{Os}/^{188}\text{Os})$  - Initialverhältnis von  $0,111 \pm 0,004$  entspricht. Die HSE-Konzentrationen sind mit archaischen EFs und modernen Krustenwerten vergleichbar, während die  $(^{187}\text{Os}/^{188}\text{Os})$  - Initialverhältnisse höchst unradiogen sind und einen starken Einfluss einer aus dem Mantel stammenden Quelle auf das Wasser des Urucum-Beckens belegen. Das finale Re-Os-Alter steht in guter Übereinstimmung mit früher veröffentlichten Altersdaten der Urucum EF. Da wir die EF- und Mn-F-Proben direkt datiert haben, wird das Ablagerungsalter des Urucum EF-Mn-F besser eingrenzt. Eine Ablagerung

vor 590 Ma wird weiter unterstützt, so dass ein Zusammenhang mit der Marinoischen Eiszeit wahrscheinlicher ist als mit der Glaskier-Eiszeit.